THE DECAY OF $_{55}Cs^{134}_{79}$

by

TARLOK SINGH NAGPAL
B.A., The Panjab University (India), 1952
M.Sc., The Aligarh Muslim University (India), 1956

A THESIS SUBMITTED IN PARTIAL FULFILMENT OF

THE REQUIREMENTS FOR THE DEGREE OF

DOCTOR OF PHILOSOPHY

in the Department

of

PHYSICS

We accept this thesis as conforming to the

required standard

THE UNIVERSITY OF BRITISH COLUMBIA
September, 1964

In presenting this thesis in partial fulfilment of the requirements for an advanced degree at the University of British Columbia, I agree that the Library shall make it freely available for reference and study. I further agree that permission for extensive copying of this thesis for scholarly purposes may be granted by the Head of my Department or by his representatives. It is understood that copying or publication of this thesis for financial gain shall not be allowed without my written permission.

Department of Physics

The University of British Columbia,
Vancouver 8, Canada

Date Sep, 1964.

The University of British Columbia

FACULTY OF GRADUATE STUDIES

PROGRAMME OF THE

FINAL ORAL EXAMINATION

FOR THE DEGREE OF

DOCTOR OF PHILOSOPHY

of

TARLOK SINGH NAGPAL

B.A., The Panjab University (India), 1952

M.Sc., The Aligarh Muslim University (India), 1956

MONDAY, SEPTEMBER 14, 1964, AT 1:30 P.M.

IN ROOM 10, HEBB BUILDING (PHYSICS)

COMMITTEE IN CHARGE

Chairman: I. McT. Cowan

M.P. Beddoes	G. Jones
J.W. Bichard	K.C. Mann
K.L. Erdman	J.F. Scott-Thomas

External Examiner: R.D. Connor

University of Manitoba

DECAY OF $_{55}Cs^{134}_{79}$

ABSTRACT

The tests of performance of the modified thin-lens magnetic spectrometer using ring-detection have been extended using improved mechanical controls of detector position. The results show only a small improvement over the performance obtained previously in this laboratory. We conclude that the limit of performance with the thin-lens magnet has been reached. Further improvement may be achieved only with a precision-wound magnet coil which will produce a completely symmetric field.

The decay of $_{55}Cs^{134}_{79}$ has been investigated using the modified thin-lens spectrometer, a scintillation spectrometer and beta-gamma, conversion-electron gamma coincidence techniques. The results support the simpler decay scheme proposed by Van Wijngaarden and Connor. The beta decay has three components with end-point energies and intensities of 659±3 kev(67.3%), 411 kev (2.5%) and 89 kev (30.3%), estimated from the energy level intensity balances in Ba^{134}. These intensity balances show discrepancies of less than 3% of the total decay intensity.

The conversion coefficients, calculated from the conversion electron and gamma-ray intensities lead to the following multipolarity identifications for the transitions in Ba^{134}; 473 kev (M1 or E2), 563-569 kev (M1 or E2), 605 kev (E2), 797-803 kev (E2), 1036 kev (M1 or E2), 1168 kev (E2) and 1366 kev (E2), in agreement with other work. The M1 or E2 character of the

473 kev and 1036 kev transitions makes it possible to assign a spin of 3+ or 4+ to the 1641 kev level which was uncertain before. An unsuccessful search for evidence of a 960 kev gamma-ray reported by others puts an upper limit of 0.2% on its intensity.

GRADUATE STUDIES

Field of Study: Physics

Quantum Mechanics	F.A. Kaempffer
Waves	J.C. Savage
Electromagnetic Theory	G.M. Volkoff
Nuclear Physics	J.B. Warren

Related Studies:

Applied Electronics	M.P. Beddoes
Differential Equations	J.F. Scott-Thomas

ABSTRACT

The tests of performance of the modified thin-lens magnetic spectrometer using ring-detection have been extended using improved mechanical controls of detector position. The results show only a small improvement over the performance obtained previously in this laboratory. We conclude that the limit of performance with the thin-lens magnet has been reached. Further improvement may be achieved only with a precision-wound magnet coil which will produce a completely symmetric field.

The decay of $_{55}Cs_{79}^{134}$ has been investigated using the modified thin-lens spectrometer, a scintillation spectrometer and beta-gamma, conversion-electron gamma coincidence techniques. The results support the simpler decay scheme proposed by Van Wijngaarden and Connor. The beta decay has three components with end-point energies and intensities of 659±3 kev(67.3%), 411 kev (2.5%) and 89 kev (30.3%), estimated from the energy level intensity balances in Ba^{134}. These intensity balances show discrepancies of less then 3% of the total decay intensity.

The conversion coefficients, calculated from the conversion electron and gamma-ray intensities lead to the following multipolarity identifications for the transitions in Ba^{134}; 473 kev (M1 or E2), 563-569 kev (M1 or E2), 605 kev (E2), 797-803 kev (E2), 1036 kev (M1 or E2), 1168 kev (E2) and 1366 kev (E2), in agreement with other work. The M1 or E2 character of the 473 kev and 1036 kev transitions makes it possible to assign a spin of 3+ or 4+ to the 1641 kev level which was uncertain before. An unsuccessful search for evidence of a 960 kev gamma-ray reported by others puts an upper limit of 0.2% on its intensity.

TABLE OF CONTENTS

LIST OF ILLUSTRATIONS AND TABLES

To follow page

To follow page

ACKNOWLEDGEMENTS

The work reported upon in this thesis has been made possible by the assistance and cooperation of a number of people in the Department of Physics, and to them I am most grateful.

Dr. J.B. Warren and Dr. B.L. White made the multichannel pulse height analyzer available to me and gave me advice on its use. Dr. Garth Jones was very helpful with some electronics problems. Mr. A. Fraser, Mr. J. Lees, Mr. E. Price, and members of the workshop staff provided valuable technical assistance. To all of these, I express my sincere thanks.

To Dr. K.C. Mann, who suggested the research problem, for his advice and guidance throughout the course of this work, I express my sincerest thanks.

The project was supported by the National Research Council of Canada, through Grants-in-Aid of Research to Dr. K.C. Mann.

INTRODUCTION

It was established in 1912 by the alpha scattering experiments of Sir Ernest Rutherford that an atom has a central massive core called the nucleus, where all the positive charge and all but a small fraction of the total mass are concentrated. Positive charge on the nucleus is due to the presence of positively charged particles called protons, each carrying a unit electronic charge. The number of protons in a nucleus is generally denoted by Z and is known as its atomic number. Surrounding the nucleus are Z electrons in various states of motion.

Modern theories of the atomic nucleus begin with the discovery of the neutron by Chadwick in 1932 and the suggestion of Heisenberg, shortly thereafter, that the elementary constituents of nuclei are protons and neutrons, often referred to indiscriminately as nucleons. The number of nucleons in a nucleus is its mass number and is denoted by A. Thus a nucleus of mass number A and atomic number Z is composed of Z protons and A-Z=N neutrons. Nuclei of equal Z and unequal N are called isotopes, those of equal N and different Z are called isotones, while nuclei of the same mass number A are isobars. A nuclear species or nuclide is generally denoted by the symbol X(A,Z), where X stands for the chemical symbol of the nuclide.

Quantum mechanical invesigations into the behaviour of a nucleus as a proton-neutron system reveal that such a system can exist only in certain discrete energy states which correspond to certain allowed arrangements and motions of the nucleons. Each state is characterized by properties such as energy, angular momentum (or spin), parity,* etc. The state of the lowest energy is called 'ground' state and all others are known as 'excited' states.

---

* In quantum mechanics a nuclear state is described by a wave function. On changing the sign of the coordinates of the wave function (mirror reflection) its sign may or may not change. Parity describes this behaviour. In the former case it is said to be odd, in the latter even.

A nucleus in an excited state is unstable or radioactive, and may attain stability through a variety of processes depending, among other things, upon the excitation energy available. The process of de-excitation may involve a change in the atomic number of the nucleus (beta emission and orbital electron capture) or no change in the atomic number (gamma emission, internal conversion and internal pair formation). In the former case, the nuclide is transformed to another which may also be left in an excited state; in the latter the nuclide remains unchanged. The probabilities of the different events are complicated functions of the energies and the spins and parities of the initial and final energy states involved in the process. It is useful to represent all such processes on energy level diagrams such as are shown in Figure 1. These representations are called decay schemes.

One important function of nuclear spectroscopy is the establishment of decay schemes for all nuclides with spin and parity assignments to each level, and a comparison of experimental measurements with theoretical predictions.

Decay schemes of a large number of nuclides have been investigated but only the simplest of them are well-established. The modes of decay of many nuclides are very complex and the data that can be collected in such cases generally are inadequate to lead to an unambiguous determination of the decay schemes. Therefore, it is not surprising to find that a particular decay has been investigated by many workers using a variety of techniques without reaching agreement on the decay process. The decay of Cs^{134}, the analysis of which forms part of the present work, is an example.

To follow page 2.

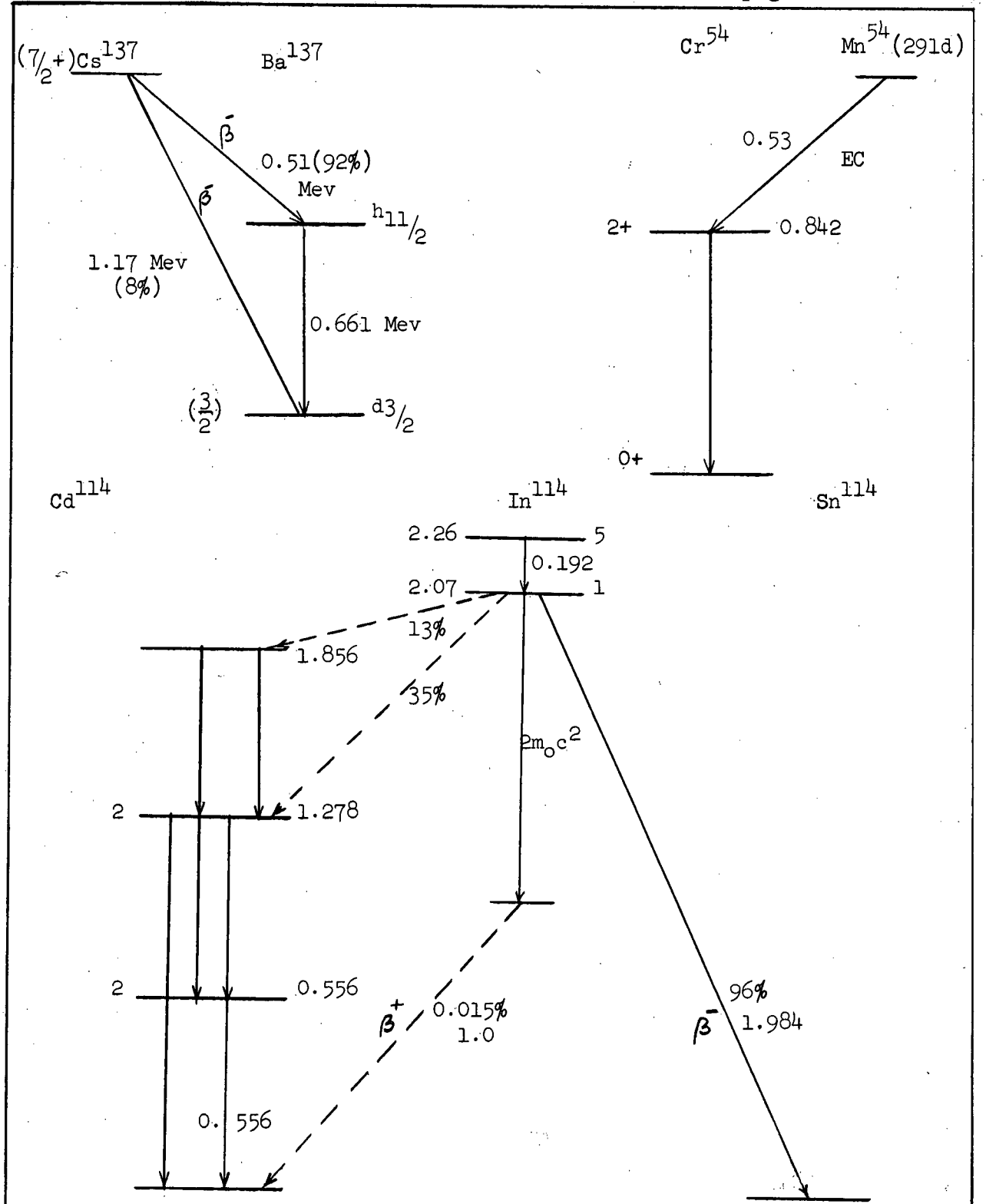

Fig.1. Typical Decay Schemes

CHAPTER 1

THEORY OF BETA AND GAMMA DECAY

BETA DECAY

In this process an unstable nucleus (parent) emits a negatron or a positron, or captures an orbital electron. The product nucleus (daughter) has the same mass number but its atomic number differs from the parent by one unit. Thus beta decay takes place between isobars.

Emitted negatrons and positrons have a continuous energy distribution from zero to some maximum energy which is related to the energy available for the decay. Since the decay takes place between discrete initial and final states, the emitted electrons do not carry away the entire energy available.

Electrons are not fundamental nuclear constituents so they must be created during the decay. The conservation of energy, momentum, and angular momentum in the beta decay process and the distribution in energy of the emitted electrons can be understood only if it is assumed that in addition to the electron, a second particle called the neutrino (ν) is emitted. The neutrino is assumed to have no charge, practically zero mass and an intrinsic spin angular momentum of $\frac{1}{2}\hbar$. These assumptions originally proposed by Pauli, led Fermi[1] to construct his theory of beta decay. It is only recently that the direct evidence for the existence of the neutrino has been found[2].

Since the number of nucleons A remains unaffected, beta decay essentially consists of the transformation of a neutron (or proton) in the parent nucleus into a proton (or neutron) in the daughter nucleus. Thus beta transitions may be indicated by:

$$(A,Z) \longrightarrow (A,Z\pm1) + e^{\mp} + \nu \qquad (1)$$

(negatron or positron emission)

$$(A,Z) + e^{-} \longrightarrow (A,Z-1) + \nu \qquad (2)$$

(capture of the orbital electron)

Processes (1) and (2) are energetically possible only if,

$$M(A,Z) > M(A,Z+1) \quad \text{negatron emission}$$

$$M(A,Z) > M(A,Z-1)+2m_0 \quad \text{positron emission}$$

$$M(A,Z) > M(A,Z-1) \quad \text{orbital electron capture}$$

where $M(A,Z)$ is the mass of an atom of mass number A and atomic number Z, and m_0 is the rest mass of electron.

In the description of processes (1) and (2) above, we have assumed that the neutrino accompanying a negatron is identical with that accompanying a positron. This is the assumption made by Majorana[3]. The alternative assumption is that of Dirac[4] whereby the particle emitted with a positron is the 'normal' neutrino and that emitted with a negatron is its 'antiparticle' or antineutrino. In Dirac's theory of spin-$\frac{1}{2}$ particles, the emission of an antiparticle is equivalent to the absorption of a normal particle and therefore all nuclear beta processes can be conveniently expressed by a basic relation, i.e.,

$$p + e^- \longleftrightarrow n + \nu \qquad (3)$$

which is interpreted as the annihilation of a neutron (n) and a neutrino (ν) leading to the creation of a proton (p) and a negatron (e^-) or vice versa.

Theory of Beta Decay

Fermi's basic assumption is that the leptons (electron and neutrino) in nuclear beta decay are created as a result of the transformation of a neutron state into a proton state, or vice versa, inside a nucleus in much the same way that a photon is born with the change in state of a charged radiating system. Beta transition probabilities, therefore, can be calculated using the same 'golden rule' of time dependent perturbation theory which is used for calculating electro-magnetic transition probabilities in the theory of radiation. The golden rule gives as the transition probability, t per unit time;

$$t = \frac{2\pi}{\hbar} |\langle U_f | H | U_i \rangle|^2 \frac{dn}{dE} \qquad (4)$$

where $U_{i,f}$ are initial and final wave functions of the system, $\frac{dn}{dE}$ is the density of final states available to the emitted particles and H is the force or 'interaction' which brings about the transformation of the system from an initial to a final state. In the theory of radiation the interaction is taken over from classical theory and the elementary electronic charge e measures the strength of the interaction. For beta decay, however, no such classical analog exists. The beta interaction, therefore, has to be invented to fit the experimental results.

(i) Beta Interaction

Fermi proposed that the interaction is proportional to a four vector current associated with the beta decay process. From the viewpoint of mathematical convenience it can be written as:

$$H = g (\psi_p^* \underline{O} \psi_n)(\psi_e^* \underline{O} \psi_\nu) + \text{h.c.} \qquad (5)$$

where 'g' measures the strength of interaction. Starred ψ's represent the corresponding wave functions of the particles created and simple ψ's those of the particles annihilated. $\underline{O}$ is an operator which brings about the annihilation of the two particles to create two new ones. h.c. is the hermitian conjugate of the expression preceeding it and is included for the sake of completeness and accounts for the creation of positrons.

Particles involved in beta decay are all spin-$\frac{1}{2}$ particles, each of which is represented by a four-component vector (spinor) in Dirac's theory. $\underline{O}$ can be any operator containing spin coordinates. Using Dirac four matrices to construct the $\underline{O}$'s and then combining the latter with ψ's, a large number of interactions are possible. Of these, only those are accepted that are invariant under rotations and Lorentz transformations. Physically this

defines the way the interactions depend upon the spin coordinates. Using this criterion we end up with just five types of interactions called respectively scalar (S), vector (V), tensor (T), axial vector (A) and pseudoscalar (P). Fermi's original hypothesis quoted the vector interaction as an example. There is no a priori reason why each of these five interactions cannot bring about beta decay and hence an arbitrary linear combination of these is a possible choice. The most general interaction therefore is

$$H = g \sum_i C_i (\psi_p^* \underline{O_i} \psi_n)(\psi_e^* \underline{O_i} \psi_\nu) + \text{h.c.} \qquad (6)$$

where $\underline{O_i} = O_{S,V,T,A,P}$, and $C_i = C_{S,V,T,A,P}$ are arbitrary constants .

The interaction (6) is invariant under space reflection or it conserves parity and is called 'even'. A similar interaction but 'odd' in nature can also be constructed and is obtained by replacing ψ_ν in (6) with $\gamma_5 \psi_\nu$. γ_5 has a pseudoscalar character, which imparts an 'odd' behaviour to the interaction.

Before Yang and Lee[5] advanced their hypothesis of parity non-conservation in weak interactions, the even and odd interactions had been used as equivalent alternate ways in which one could formulate a theory of beta decay. The possibility of their coexistence in any decay was rejected to maintain the then secure view that parity was conserved in weak interactions. (Beta decay is a weak interaction.)

Immediately following Yang and Lee's hypothesis, a large number of experiments were performed, the first being the classic measurement of Wu et al[6] on the spatial distribution of beta particles emitted from aligned nuclei. They proved that the hypothesis was correct and hence both odd and even interactions can coexist in a decay. A general form of interaction, then,

may be:

$$H = g\sum_i \left[\psi_p^* \underline{O}_i \psi_n \; (C_i \; \psi_e^* \underline{O}_i \psi_\nu + C_i' \psi_e^* \; \underline{O}_i \gamma_5 \psi_\nu) \right] + \text{h.c.} \qquad (7)$$

To simplify (7) use is made of the available experimental evidence[7], which shows that the negatron and neutrino emitted in beta decay are longitudinally polarized with spin antiparallel to their momentum. When tracked down theoretically, this means that

$$C_i = C_i'$$

and that only vector and axial vector interactions should be included. The presently accepted interaction therefore is

$$H = g\sum_{V,A} C_{V,A} \left[(\psi_p^* \underline{O}_{V,A} \psi_n) \; \psi_e^* \underline{O}_{V,A} \; (1+\gamma_5) \psi_\nu \right] + \text{h.c.} \qquad (8)$$

with $C_A = -1.2\, C_V$ [8]

(ii) Beta Spectrum

In calculating beta decay rates using (4) Fermi made the following assumptions;

(1) the nuclear extension $\sim \bar{r} = 0$;

(2) U_i is the wave function of the initial nucleon, ψ_i say whereas $U_f = \psi_f \psi_\beta \psi_\nu$; $\psi_{f,\beta,\nu}$ are respectively the wave functions of the final nucleon, electron and (anti) neutrino;

(3) electrons and antineutrinos are considered emerging as plane waves with momentum p_β and p_ν respectively. Therefore

$$\psi_\beta = \frac{1}{\sqrt{V}} e^{i \bar{p}_\beta \cdot \frac{\bar{r}}{\hbar}} \; , \; \psi_\nu = \frac{1}{\sqrt{V}} e^{-i \bar{p}_\nu \cdot \frac{\bar{r}}{\hbar}} \qquad (9)$$

where $\frac{1}{\sqrt{V}}$ is a normalization factor using an arbitrary volume V around the nucleus;

(4) the transition probability is proportional to the expectation value for the electron and the antineutrino at the nucleus, i.e. $\propto |\psi_\beta(0)|^2 |\psi_\nu(0)|^2$.

Using these assumptions with

$$\frac{dn}{dE} = \frac{V^2 p_\beta^2 p_\nu^2 \, dp_\beta}{4\pi^4 \hbar^6 c} = \frac{V^2 (E_0 - E_\beta) p_\beta^2 dp_\beta}{4\pi^4 \hbar^6 c} \qquad (10)$$

where $E_{0,\beta}$ respectively are disintegration energy and beta particle energy, and making use of equation (4), the probability per unit time that a beta particle will be emitted with momentum between p_β and $p_\beta + dp_\beta$ is

$$P(p_\beta)dp_\beta = \frac{g^2}{2\pi^3 \hbar^7 c^3} |M|^2 p_\beta^2 (E_0 - E)^2 \, dp_\beta \qquad (11)$$

where $M = \int \psi_f^* \, \underline{O}_i \, \psi_i \, d\tau \qquad (12)$

In deriving (11) it was assumed that the nuclear charge of the transforming nucleus allows the electron plane wave to emerge undistorted. Physically, negatrons will be 'held back' and positrons 'pushed forward' as a result of the Coulomb forces between the nuclear and the electronic charges, resulting in a characteristic distortion of the spectrum. Correction factors for either case and for different values of p and Z have been calculated and are available. These are known as Fermi functions, F(Z,p). The corrected form of (11), therefore, is

$$P(p_\beta)dp_\beta = \frac{g^2}{2\pi^3 \hbar^7 c^3} F(Z,p) \, |M|^2 p_\beta^2 (E_0 - E_\beta)^2 dp_\beta \qquad (13)$$

A more useful form of equation (13) is obtained as follows:

n(p), the number of beta particles having momentum between p and p+dp is related to P(p) through a constant multiplier.

Further, it is customary to use units in which $m_0 = \hbar = c = 1$, and particle momentum p and energy W are expressed as

$$p = \frac{p_\beta}{m_0 c} \quad \text{and} \quad W = \frac{E_\beta}{m_0 c^2}$$

This, then, leads to the following form of the momentum distribution of beta particles

$$n(p)dp = \text{const.}\ |M|^2\ F(Z,p)p^2(W_0-W)^2dp \qquad (14)$$

In (14) $p^2(E_0-E)^2$ is known as the 'statistical-weight'. It is this factor that describes the statistical division of the disintegration energy between the beta particle and the neutrino.

In calculating the transition probability, plane wave functions were used for the light particles. These were evaluated at the nuclear-centre on the assumption that the nuclear dimensions were negligible compared with the wave length $\lambda = \frac{2\pi}{K}$ of the plane wave. The product of the wave functions may be expressed as:

$$\psi_\beta^* \psi_\nu = \frac{1}{V} e^{-i(\bar{p}_\beta + \bar{p}_\nu).\frac{\bar{r}}{h}} = \frac{1}{V} e^{-i\bar{k}.\bar{r}}$$

Actually the nuclear extension $|r|$ is such that $|kr| \ll 1$ for moderate energies and therefore $e^{-i\bar{k}.\bar{r}}$ may be expanded as

$$\left.\begin{aligned} e^{-i\,k.r} &= 1 - i(\bar{k}.\bar{r}) + \tfrac{1}{2}(\bar{k}.\bar{r})^2 - \ldots \\ &= \sum_0^\infty (2l+1)i^l\, j_l(kr) P_l(\cos\theta) \end{aligned}\right\} \qquad (15)$$

where j_ℓ is the spherical Bessel function and $P_\ell(\cos\theta)$ are Legendre Polynomials.

Using (15), we can write

$$\left.\begin{aligned} \langle U_f | H | U_i \rangle &\sim \int \Psi_f^* \underline{O} \Psi_i \, dt - i \int \Psi_f^* \, \bar{k}.\bar{r}\underline{O} \, \Psi_i \, dt + \cdots \\ &\sim |M| - |M_1| + |M_2| - \cdots\cdots \end{aligned}\right\} \quad (16)$$

where successive terms decrease by a factor of approximately 10^{-2} for energies $\sim$ 1 Mev. M is momentum independent, while $|M_1|$, $|M_2|$, etc. are all momentum dependent.

The orthogonality properties of the wave functions may, under certain conditions involving spin and parity changes in the transition, cause any of the matrix elements to vanish. This being so, it is the first non-vanishing element which primarily determines the decay probability. The assumption leading to equation (14) meant that $|M|$ only was used. Such transitions are most probable, and are called 'allowed' transitions. Where $|M|$ is zero, and $|M_1|$ non-zero, we have a 'first-forbidden' transition, etc.

The transition rate in the case of a forbidden transition may be expressed by an equation similar to equation (13), i.e.,

$$P(p_\beta)dp_\beta = \frac{g^2}{2\pi^3 \hbar^7 c^3} S_n(p) F(Z,p)(E_0 - E_\beta) p_\beta^2 \, dp_\beta \qquad (17)$$

where $S_n(p)$ is called the 'shape-factor'.

The probability of observing forbidden transitions decreases rapidly with increasing order of forbiddenness.

(iii) Selection Rules

The conditions whereby a transition falls within a certain classification (allowed, forbidden, etc.) are called 'selection rules'. These obviously are conditions whereby the element $|M_i|$ does not vanish. As might be expected the quantum descriptions involved are angular momentum and parity.

The angular momentum $\bar{I}\hbar$ of any nucleus is considered to be a vector sum of all angular momentum components of the constituent nucleons. These are of two types: orbital angular momentum $l_i\hbar$ for the ith nucleon, where l_i is an integral, and intrinsic spin angular momentum $s_i\hbar$, where $s_i = \frac{1}{2}$. The parity of the wave function for the ith nucleon is odd or even if $(-1)^{l_i}$ is odd or even.

It can be shown that for the particles involved in the transition, the first element $|M|$ is non-vanishing if $\Delta l = 0$, that is, if the parities of the initial and final states are the same. These are the allowed transitions. There are two possibilities which can satisfy this parity condition. Since the decay involves two spin-$\frac{1}{2}$ particles, the beta particle and the neutrino, the total angular momentum change is that of their intrinsic spins. The two particles may come out with their spins antiparallel, in which case $\Delta I = 0$. This is the so called singlet state and is the basis of the Fermi hypothesis and his selection rules. The other possibility is that both particles are emitted with spins parallel, in which case $\Delta I = 1$. This is the triplet state postulated by Gamow and Teller. To summarize for allowed transitions

$$\left.\begin{array}{ll} \Delta I = 0, \text{no} & \text{(Fermi)} \\ \Delta I = \pm 1 \text{ or } 0 \text{ (except } 0 \leftrightarrow 0), \text{ no} & \text{(Gamow Teller)} \end{array}\right] \quad (18)$$

For the first forbidden transition $|\Delta l| = 1$, i.e. change in angular momentum of one unit with change in parity, $(-1)^1 = -1$; therefore

$$\left.\begin{array}{l} \Delta I = \pm 1, 0, \text{ yes} \\ \Delta I = \pm 2, \pm 1, 0, \text{ yes} \end{array}\right] \quad (19)$$

(iv) Kurie Plot

The statistical shape of the continuous beta spectrum has been predicted by the Fermi theory as n(p) vs. p. Since the spectrometer resolution* $\frac{\Delta p}{p}$ is not zero, the measured counts per unit time at any momentum setting $N(p) = n(p)\,\Delta p$. But $\frac{\Delta p}{p} = R$, a constant. Hence the distribution function $n(p) \propto \frac{N(p)}{p}$.

* Spectrometer resolution is defined in detail on page 22

A plot of $\frac{N(p)}{p}$ vs. p gives the true spectral distribution and is shown in Figure 2.

From Figure 2 it is obvious that the spectrum approaches its end point energy W_0 tangentially making it difficult to determine accurately. The difficulty is removed if, instead, a Kurie plot is used.

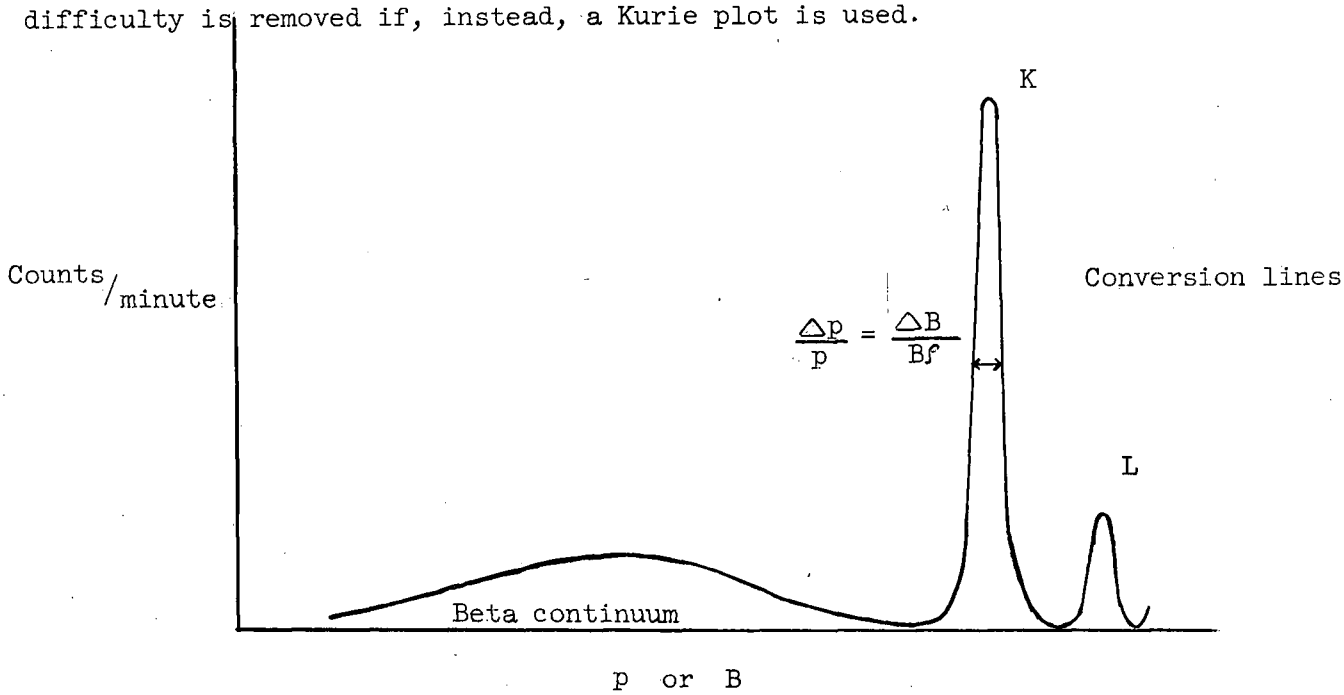

Fig. 2. A typical beta spectrum with conversion lines

For allowed transitions $|M|^2$ in equation (14) is independent of energy and therefore it follows that:

$$\left[\frac{N(p)}{p^3 F(Z,p)}\right]^{\frac{1}{2}} = \text{const } (W_0 - W) \qquad (22)$$

where $|M|^2$ has been absorbed in the constant factor. N(p) is known experimentally, the function F(Z,p) corresponding to Z and p involved is available in tables[10] and hence $\left[\frac{N(p)}{p^3 F(Z,p)}\right]^{\frac{1}{2}}$ can be computed to plot against W. A plot constructed in this fashion yields a straight line for allowed transitions and is known as Kurie plot. The extrapolation of the straight line is the usual method of determining W_0.

A complex beta spectrum may be resolved into its components through Kurie analysis.

For forbidden transitions, the Kurie plot may not be linear, since $|Mi|^2$ is no longer energy independent. In these cases, a shape factor must be included. A shape factor which produces a linear Kurie plot can provide information on the degree of forbiddeness. It is important to note that a curved Kurie plot is a strong indication that the transition is forbidden although the reverse is not always true.

The Kurie analysis does have inherent difficulties where many beta groups are involved. Any relatively weak group may be lost in the subtraction processes the method demands. Groups whose end-points are too close together cannot be resolved. Finally, and particularly in the low energy region of the spectrum, the thickness of the source and backing become important, leading to spectral distortions caused by absorption and back scattering.

(v) Comparative Half-Life

The decay constant, λ for beta transition is obtained by integrating (13) which yields

$$\lambda = \int_0^{p_{max}} P(p_\beta)dp_\beta = C\ M^2 f(Z,p_{max}) \qquad (23)$$

where $$C = \frac{g^2}{2\pi^3\hbar^7c^3}$$

and $$f(Z,p_{max}) = \int_0^{p_{max}} p_\beta^2\ (E_0-E_\beta)F(Z,p)dp \qquad (24)$$

Numerical values for $f(Z,p_{max})$ are available in tabular form[11].

Since the half life $t = (\ell n 2)\tau$ where the mean life, $\tau = \frac{1}{\lambda}$, we define the comparative half life (ft) as

$$ft = \frac{\text{constant}}{|M|^2} \qquad (25)$$

The product ft is thus a measure of the transition matrix element $|M|$. The magnitude of M is a measure of the decay probability and hence of the degree of forbiddenness. Therefore allowed transitions have the smallest ft values, the ft value increasing with increasing forbiddenness, so that they may be used for the classification of beta transitions. They range from 10^3 sec to 10^{18} sec. It is, therefore, more convenient to use $\log_{10}$ft values instead. Experimental evidence leads to the following crude classifications.

Transition	$\log_{10}$ft
Allowed	3 to 6
First forbidden	7 to 9
Second forbidden	13
Third forbidden	18

Log_{10}ft values for any decay can be conveniently calculated from the nomographs prepared by Moszkowski[12].

(vi) Orbital Electron Capture

An unstable nucleus may attain stability by capturing one of the atomic electrons. While any electron may be captured, it will most probably be a K-shell electron (if the decay energy is sufficient) because K shell wave functions overlap the nucleus the most. This process is known as K-capture. No observable particle is emitted but the final atom emits an X-ray when a bound electron from a higher shell drops into the vacancy in the K shell. X-rays emitted are soft and so the capture process is hard to observe. The so called Auger electrons also accompany the process.

Theoretically, K-capture is similar to positron emission ($p+e_k \longrightarrow n+\nu$) but is energetically favoured over the latter because no positron rest mass has to be created and the rest mass of the captured electron is added to the energy release.

Where K-capture is energetically impossible, L-capture will take place because lesser energy is required to ionize an L shell electron. Along with a normal K-capture process, capture from the L and higher shells is always present.

The calculation of the decay constant for the orbital electron capture decay differs from that of electron emission in two respects. In the first place instead of free electron wave functions, K, L, etc. shell eigenfunctions of the atom are used; secondly, the statistical factor has the form

$$(W_0 + m_0c^2 - W_i)$$

where W_i is the ith shell binding energy of the electron. The decay constant can still be written in a form similar to (23), viz,

$$\lambda_K = C_K|M|^2 f_K(Z,W_0) \qquad (26)$$

where $$f_K = 2\pi\left(\frac{Ze^2}{hc}\right)^3\left[W_0 + 1 - \tfrac{1}{2}\left(\frac{Ze^2}{hc}\right)^2 \right]^2 \qquad (27)$$

Z in equation (29) refers to the parent and not the daughter nucleus. $Log_{10}ft$ values for this process have also been tabulated.

GAMMA DECAY

In the majority of beta processes, a daughter nucleus is left in an excited state with too little energy to emit a nucleon. It will, therefore, lose its excitation energy either by the emission of gamma rays or by the ejection of an electron from an orbit of the daughter atom. The latter process is known as 'internal conversion' and will be discussed later. De-excitation by gamma radiation may take place in a single step or through several steps.

(i) Multipole Radiation

By treating the nucleus as a system of charges and currents, its radiation can be sorted out into distinct types. In quantum theory, this corresponds to sorting the emitted quanta into what is known as 'multipole orders L', according to the angular momentum L (in units of $\hbar$) carried off by each quantum. For each multipole order, there are two possible classes of radiation: electric 2^Lpole (EL) and magnetic 2^Lpole (ML), which differ in parity. Classically EL and ML refer to the radiation emitted by a vibrating electric or magnetic 2^L pole. Generally the electromagnetic radiation field of a system contains all the multipoles expressed as a converging power series in $\frac{R}{\lambda\!\!\!^{-}}$ with the familiar classical restriction that $\frac{R}{\lambda\!\!\!^{-}} \ll 1$, where R is a typical radius of the charge current system and $\lambda\!\!\!^{-}$ is the radiated wavelength/2π. This means that only the lowest multipole order L allowed by the symmetries of the system can make an appreciable contribution, for gamma rays up to quite high energy. It also turns out that the strength of an electric multipole exceeds that of a magnetic multipole of the same order by a factor $\frac{c}{v}$, where v is the velocity of the charged particles. Mixtures of electric and magnetic multipoles may be radiated. So far only (MI+E2) has been detected.

The conservation of angular momentum and parity for the nucleus plus gamma rays imposes selection rules on the possible multipolarities of a gamma transition between two states of specified angular momenta (I_i, I_f) and parities (π_i, π_f):

$$\text{i.e.,} \quad I_i - I_f \ll L \ll I_i + I_f$$

$$\text{and} \quad = \frac{\pi_f}{\pi_i} = (-1)^L \text{ for EL radiation} \qquad = -(-1)^L \text{ for ML radiation} \tag{28}$$

Here $\Delta\pi = +1$ means no change in parity and $\Delta\pi = -1$ means change in parity.

It is noted that radiative transitions cannot occur for L = 0. If $I_i=I_f=0$, ordinary radiation is wholly forbidden though such transitions may take place by pair production or by internal-conversion.

The gamma transition probability t is calculated using the same well-known equation from perturbation theory:

$$t = \frac{2\pi}{h} |\langle U_f | H | U_i \rangle|^2 \frac{dn}{dE} \qquad (4)$$

The operator corresponding to H depends upon the multipole order. For example in the case of electric dipole radiation it will have the form $\sum_i e_i \bar{x}_i$. Estimates of the transition probabilities for various multipole orders can be made. These estimates, of course, depend upon the choice of a nuclear model. Moszkowski[13], for example, has made such estimates using an extreme single particle model, namely a proton in a central velocity independent potential. These estimates, although very crude, do in many cases provide a basis for the analysis of experimental data.

(ii) Internal Conversion and Conversion Coefficients

Internal conversion processes result from a direct interaction between the multipole field of a nucleus and a bound atomic electron. The kinetic energy E_i of the emitted electron, is given by

$$E_i = W-B_i \qquad (29)$$

where W is the excitation energy and B_i the atomic binding energy of the electron. Equation (29) becomes identical in form with Einstein's photo-electric equation, if W is replaced by the energy $h\nu$ of the unsuccessful photon. This led to an erroneous picture of the process that the excited nucleus first emits a photon which is then absorbed by the atom to produce a photoelectron. This hypothesis known as 'internal photoelectric effect' was rejected because of the fact that transitions like $0 \rightarrow 0$ are observed in internal conversion though such transitions cannot produce any gamma rays.

If gamma emission is allowed, internal conversion and photon emission are two competing de-excitation processes with transition probabilities depending upon the matrix element $\langle U_f | H | U_i \rangle$.

If in a de-excitation process N_e and N_γ are respectively the number of internal conversion electrons and photons, the conversion coefficient is defined as:

$$\alpha = \frac{Ne}{N_\gamma} \qquad (30)$$

Since conversion electrons can come from different atomic shells $N_e = N_{e_K} + N_{e_L} + N_{e_M} + \ldots$, therefore

$$\alpha = \alpha_K + \alpha_L + \alpha_M + \ldots$$

where $\alpha_K = \frac{Ne_K}{N\gamma}$ is the K shell conversion coefficient

$$\alpha_L = \frac{N_{e_{L_1}} + N_{e_{L_2}} + N_{e_{L_3}}}{N_\gamma}$$ is the L shell conversion coefficient,

and so on.

Theoretical values of the internal conversion coefficient are independent of any particular nuclear model but depend strongly on

W, the transition energy

Z, the atomic number of the transforming nucleus

L, the multipole order of the transition

$\Delta\pi$, change in parity

Extensive theoretical calculations of internal conversion coefficients are available[14]. A comparison between experimental and theoretical values of conversion coefficients is a useful tool for determining parity and angular momentum of nuclear states.

CHAPTER II

METHODS OF DETECTION AND MEASUREMENT

Our knowledge of nuclear properties began when experimenters first learned how to detect and analyze particles or rays emitted by radioactive nuclei. Even today, the study of nuclear structure is a matter of counting and analyzing what comes out of such nuclei either spontaneously or when induced by particle bombardment. In what follows we shall describe briefly only those types of detectors and analyzers (spectrometers) that are generally used with beta and gamma ray work.

DETECTION SYSTEMS

Some important characteristics that determine the quality and suitability of a detection and measurement system for a particular radiation are 1) its efficiency of detection (i.e. its ability to detect a reasonable fraction of the radiation that passes through it, 2) its resolving power (ability to distinguish between radiations of almost equal energy or momentum) and 3) its resolving time (ability to distinguish between two almost simultaneous events). If the energy of a particle is E and ΔE is the uncertainty in its measurement, the resolution is measured by $\frac{\Delta E}{E} \times 100$.

While the last few years has seen the evolution of a wide variety of basic detectors for all types of particles, those used in beta-ray spectroscopy may be classified in three groups, the gaseous ionization detector, the scintillation phosphor, and more recently, the solid-state detector.

The gaseous ionization detector was one of the earliest used. It consists of a volume of gas in an electric field. Any ionizing particle which passes through the gas, produces ion-pairs. These move under the influence of the field to collecting electrodes and produce an electrical pulse in an external circuit. The field strength may be low enough to produce no secondary ionization, or it may be high enough to produce secondary ion

multiplication or even an avalanche. The Geiger counter is an example of the last case and the output pulse size is independent of the number of ion-pairs originally produced by the particle. Such a pulse gives no information except the arrival of the particle. Where avalanches are not produced, the output pulse height is proportional to the original number of ion-pairs, and hence to the energy lost in the gas by the particle. The proportional counter is such a detector, and particularly in the case of low energy electrons, the pulse height can be correlated with the electron energy.

These detectors suffer in comparison with others in their time resolution and it is difficult to resolve particles which arrive less than 10^{-6} seconds apart. Also, for weakly ionizing radiations, such as gamma-rays, the gas volume must be large.

The scintillation detector makes use of the fact that ionization and excitation produced in materials such as zinc sulfide, calcium tungstale, anthracene, naphthalene or thallium-activated sodium iodide, results in the emission of photons to which the materials are transparent. Such materials are known as phosphors, and the photon bursts are called scintillations. The number of photons produced is proportional to the energy lost in the phosphor by the particle. The photons are converted into an electrical pulse, usually by means of a secondary electron device called a photomultiplier, the output pulse height being proportional to the energy of the particle. The scintillation detector is usually much smaller than gaseous detectors, has a very short resolving time, and a high detection efficiency. It has been the most popular detector for gamma-rays, even though its energy resolution is somewhat poor.

It was discovered as early as 1945 that semiconducting materials such as diamond, zinc sulfide and silver chloride, when exposed to an ionizing radiation, became electrically conducting. The charge thus released can be

collected to produce an electrical pulse just as in the case of the gaseous detector. They suffered from certain inherent disadvantages however. There are a number of charge carriers already present in such crystals caused by thermal excitation and impurities, and these frequently outnumber those produced by the incident particle. Also, crystal impurities provide trapping centers for the charges which lead to a storage of charge and ultimate crystal polarization. Recently, these defects have been reduced by exploiting the junction properties of a semiconductor. In a p-type semiconductor, vacancies or 'holes' are the charge carriers. In an n-type semiconductor, the carriers are electrons. At a junction between p and n type materials, the charge carriers from each region close to the junction migrate into the other and a shallow layer at the interface is cleared of charge. This zone is called the 'depletion layer' and its thickness can be increased to over 1 cm by applying an external electrical field in the direction of the migration. The depletion layer behaves like an intrinsic semiconductor, and is used as the sensitive region of detection. Very recently[15], solid state detectors have shown outstanding promise in low energy nuclear physics. Their ionization potential is about 3 ev/electron-hole pair as compared with 30 ev for the gaseous detector. The lithium-drift techniques applied to silicon and germanium crystals can give energy resolutions $\sim$10ev for particles. They have a linear energy response, a very fast pulse rise-time ($\sim 10^{-9}$ seconds) and are the smallest in size of all detectors.

MAGNETIC SPECTROMETERS

Principles of Operation

The momentum p of a charged particle may be deduced from its trajectory in a magnetic field. The force on the particle is

$$\overline{F} = e(\overline{v}x\overline{B}) \qquad (31)$$

In the special case of an electron of charge e and mass m and moving with velocity v in a field B at right angles to v, we have

$$\frac{mv^2}{\rho} = evB \quad \text{or} \quad B\rho = \frac{mv}{e} = \frac{p}{e} \tag{32}$$

where ρ = radius of curvature of the path. Thus $B\rho$ is proportional to p. The gauss-cm unit of $B\rho$ is a convenient measure of electron momentum and is related to the electron energy by

$$E = m_0c^2\left[\sqrt{\left(\frac{e}{m_0} \cdot \frac{B\rho}{c}\right)^2 + 1} \; -1\right] \tag{33}$$

Extensive tabulations of this relation are available[16].

The magnetic field also possesses focusing properties, and may focus an initially divergent beam of monoenergetic electrons into a convergent one, forming an image of the source. With a suitable baffle arrangement, electrons in a small chosen momentum interval only will reach a detector placed at the focal position. Instruments with this property are known as analyzers or spectrometers.

There is a wide variety of magnetic spectrometers, whose principle of performance is based upon equation (31). A comparison of performance is better understood by first defining some of the commonly-used parameters.

a) The <u>resolving power</u> for momentum-selective instruments is defined as $\frac{B\rho}{\Delta B\rho}$. It is usually evaluated from the shape of a monoenergetic conversion line of momentum B, where $\Delta(B\rho)$ is the full width of the peak at half-maximum as shown in Figure 2. The inverse <u>resolution</u> $R = \frac{\Delta(B\rho)}{B\rho}$ is more generally used. The momentum spread $\Delta(B\rho)$ arises from the spectrometer field characteristics. The resolution R is rated 'high' or 'low' according as R is small or large.

b) The dispersion γ, defined as

$$\gamma = \frac{dx}{d(B\rho)}$$

is a measure of the spatial spread of momentum foci, x is a suitable coordinate fixing the position of the image of the focused particle. Obviously, closely spaced spectral lines can be resolved only if the distance between the images of two lines is greater than the spatial width of the lines.

c) The gathering power ω measures the geometrical efficiency of the instrument. The emission of beta-particles from an unpolarized point source is isotropic. The size and position of the entrance baffles define a solid angle of acceptance Ω, so that the fraction entering the spectrometer is

$$\omega = \frac{\Omega}{4\pi}$$

Depending upon the field characteristics, it may be that only part of these reach the detector, and some of these may miss detection if the detector efficiency is not 100%. Thus, the transmission T which measures the fraction of the total emitted beta-rays which is detected is the 'effective solid angle' expressed as a fraction of 4π. Thus

$$T \leqslant \omega$$

d) In beta-ray spectroscopy, one is often limited, not by the total activity of a source, but by its 'specific activity', i.e. the activity per unit weight. Sources must be thin to minimize spectral distortions caused by absorption and scattering within the source itself. If the specific activity is low, the source area σ must be large to produce an appreciable counting rate. Large sources produce poorer foci than small sources. In this case, the luminosity L is a useful parameter where

$$L = \sigma T.$$

An aperture luminosity L can also be defined as $\Lambda = \sigma\omega$, and obviously

$$L \leqslant \Lambda$$

Comparisons of spectrometer performances should properly include all these parameters. However, a crude but useful figure-of-merit is one that compares resolution R and transmission T. For any given instrument, the resolution may be improved at the expense of the transmission and vice-versa. In what follows, we have selected to compare the ratio $\frac{T}{R}$ as a rough guide of performance. The higher this ratio, the better the instrument.

Spectrometer Classification

There are two main groups of magnetic spectrometers, the flat spectrometer and the lens (or helical) spectrometer. In the first group, the central trajectory is confined largely to a plane perpendicular to the magnetic field. In the lens spectrometers, the trajectory spirals along the field lines. In both types, fields may be homogeneous or inhomogeneous and produced with or without iron. The shape of the field determines in each case the degree and kind of focusing. In the so-called double focusing, electrons are focused in both the horizontal and the vertical planes. The flat types may be single or double focusing; while lens types, due to their radial symmetry, are always double focusing.

Flat Spectrometers

Semicircular spectrometers (and spectrographs) are the prototypes of the flat instruments. Others in this family are the third order focusing spectrometer, the double focusing spectrometer; and various sector field spectrometers, among these the 'orange' spectrometer and the spiral orbit spectrometer. Each spectrometer in this group has a different shape of the magnetic field which is responsible for the unique type of focusing in each case, the principles of which are illustrated for each case in Figures 3 to 8.

To follow page 24.

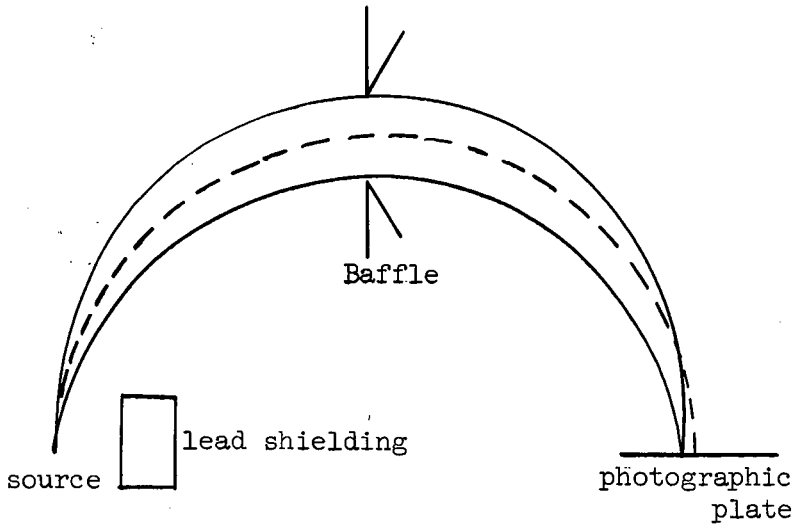

Fig. 3. Main features of the spectrometer due to Rutherford and Robinson

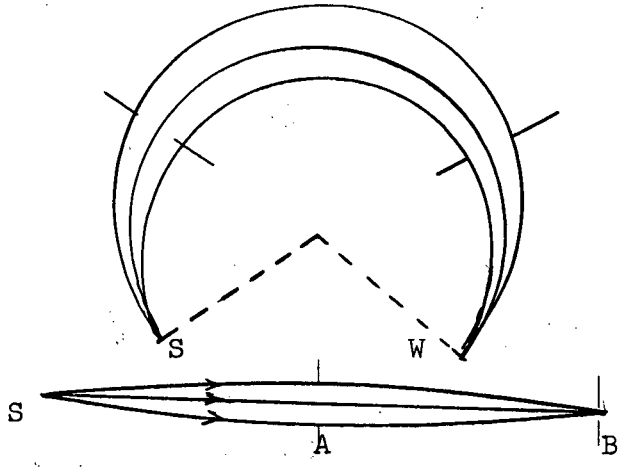

Fig.4. Double focussing

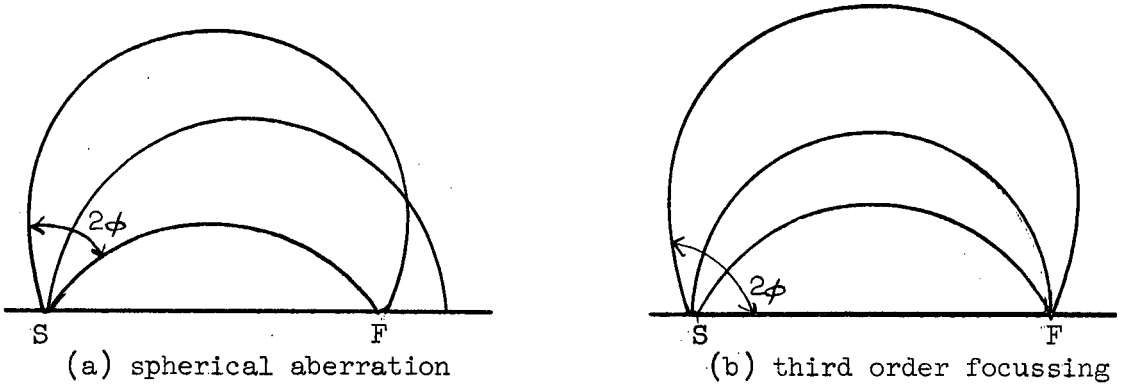

Fig. 5. Principle of third order focussing

To follow page 24

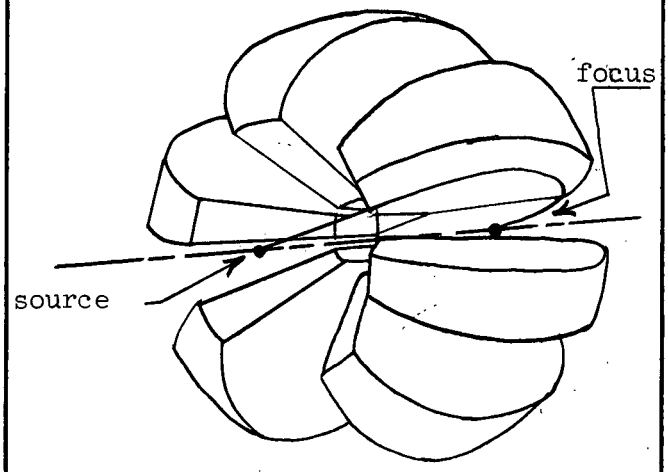

Fig. 6. "orange" spectrometer

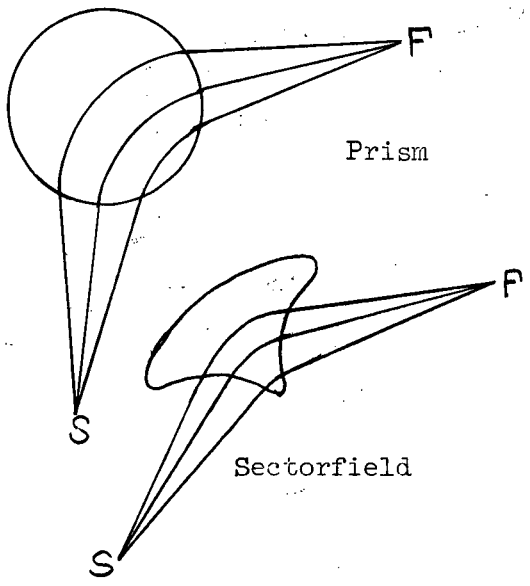

Fig. 7. Prism and sectorfied spectrometers

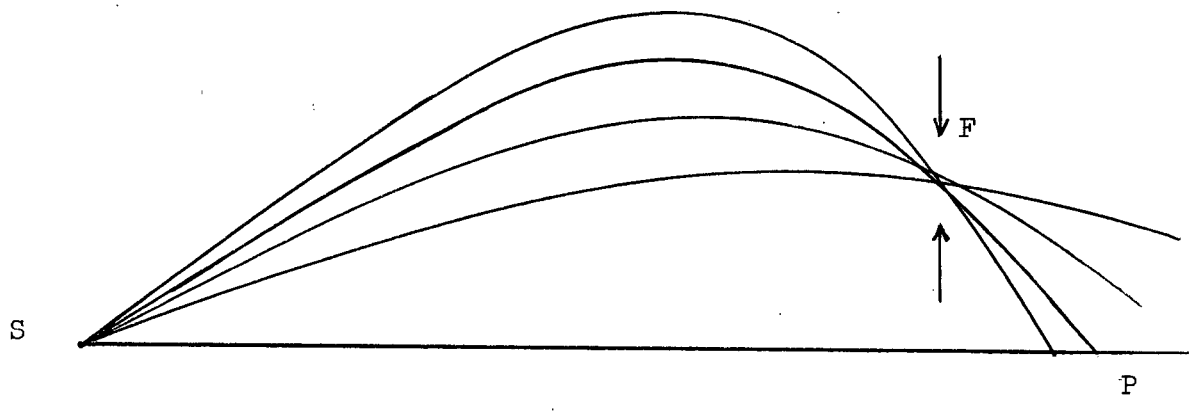

Fig. 8. Electron trajectories in thin lens spectrometer

Lens Spectrometers

To this group belong solenoidal spectrometers, long lens and short (thin) lens spectrometers, and the intermediate image spectrometer. The solenoidal spectrometer employs a uniform magnetic field over the entire electron path which makes the computation of electron trajectories very simple. Lens spectrometers suffer excessively from inherent focusing aberrations. Siegbahn[17] has shown that an 'upward concave' magnetic field gives a considerably reduced aberration. The long lens is designed to produce such a field. The intermediate image is a special type of long lens spectrometer. In these, the source and the detector lie in regions of a strong magnetic field. For some applications this proves a serious drawback. The thin lens spectrometer is described in detail in the next chapter.

There is such a wide range of problems studied in nuclear spectroscopy that it is impossible to single out one particular instrument which will have superior qualities in all cases. Different problems need different spectrometers. In general, flat spectrometers such as the semicircular and the double focusing instruments are to be preferred for high resolution, low transmission experiments and precise energy measurements. Lens spectrometers are most suitable for high transmission and moderate resolution. They are preferable, for instance, for coincidence measurements. Lens spectrometers have proven useful for reasonably accurate energy measurements as well. The orange spectrometer, however, has the unique property of showing a moderate resolution with very high transmission.

A detailed study on beta-ray spectrometers has been undertaken by Gerholm[18].

Momentum or energy measurements of beta particles with any of the magnetic spectrometers usually are not absolute. In most cases, the spectrometer is calibrated with a known monoenergetic conversion line. A number of such lines are known, their absolute momenta having been determined by other means (see for example, Seigbahn et al [19]). Where the spectrometer magnet is air-cored, a single point calibration is sufficient.

Spectrometer Measurements of Beta and Internal Conversion Spectra

The data obtained is always the counting rate N(p) as a function of the field B. From the instrument calibration, the $B\rho$ or p value corresponding to B is known and $\frac{N(p)}{P}$ is plotted against p.

Regions of such a spectrum not obscured by conversion line interference, may be subjected to a Kurie analysis. If the beta spectrum is complex, it is often possible to use the analysis to resolve the spectrum into its individual beta components, yielding information on group end-point energies and relative intensities.

The internal conversion lines, superimposed on the primary beta spectrum provide information on transition energies, where the conversion lines are reasonably intense. Also, the relative intensities of the conversion lines from various electron shells can be related to the multipole order and electric or magnetic nature of the transition. In particular, the K/L conversion ratio can be compared with theoretical estimates, which depend upon energy, multipole order and atomic number. Such comparisons assist in assigning spin and parity changes to the transition. The relative intensities of the conversion lines are just the relative areas under the lines on the $\frac{N(p)}{p}$ vs. p spectrum plot.

It is more difficult to measure absolute intensities of internal conversion lines, since this requires a precise knowledge of the parameters T and R of the instrument, and it is not always easy to measure these with sufficiently high accuracy. Where it can be done, and the accompanying gamma-ray absolute intensities are known, the conversion coefficients may be computed and compared with theory.

Spectrometer Measurements of Photoelectron Spectra

The photoelectron process provides a means whereby the spectrometer may be used to give reasonably accurate measurements on gamma-ray energies.

In this method, the source is placed in a container of low Z material, thick enough to absorb all primary electrons and internal conversion electrons. To the outside of the container is attached a small thin foil of a heavy element such as lead or uranium. Gamma rays emitted by the source eject photo electrons from the foil which is called a 'radiator' which becomes the photo electron source. High Z foils are used because the photoelectric cross section rises rapidly with increasing Z of the radiator-material.

The photo electrons ejected from the foil show up as K, L and sometimes M photopeaks beyond the Compton continuum. From the peak positions and the calibration of the instrument, one may obtain the gamma ray energy by adding the appropirate shell binding energy of the radiator element.

Relative intensities of gamma-rays can be derived from areas under the photopeaks, if the source-converter geometry is simple enough to allow calculations of yield based upon the photoelectric cross section and angular distributions. Hultberg et al[20] have discussed this problem in detail.

THE SCINTILLATION GAMMA-RAY SPECTROMETER

This system is based upon the pulse height analysis of the scintillation spectra produced in phosphors by gamma-rays. The essential components of a typical system are shown in block diagram form in Figure 9.

The electrical pulses from the output stage of the photomultiplier which are generally too small to be analyzed directly, are amplified with a linear amplifier, then sorted according to their size with either a single channel pulse height analyzer (P.H.A) or an automatic multichannel pulse height analyzer (Kicksorter), and finally recorded with a scaler. A plot of the number of pulses per unit time versus pulse height gives the intensity distribution of the charged particles or the photons absorbed by the scintillation crystal.

To follow page 27.

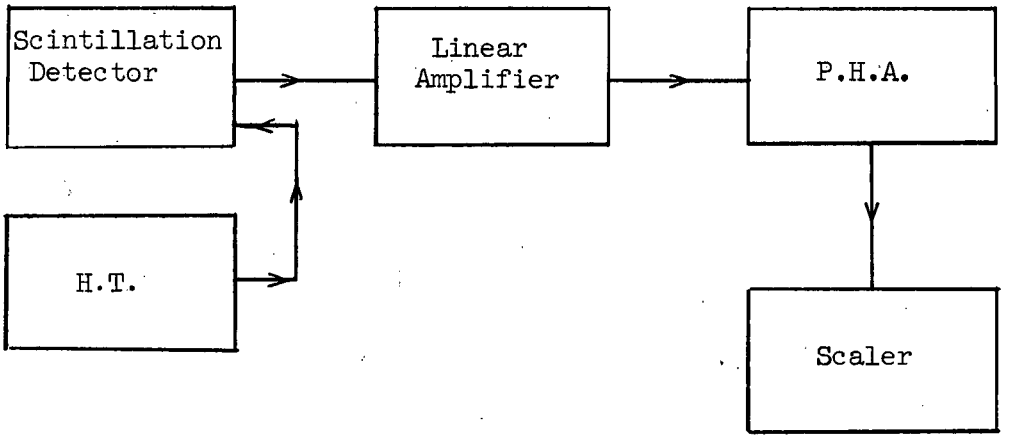

Fig. 9. Block diagram of gamma ray scintillation spectrometer

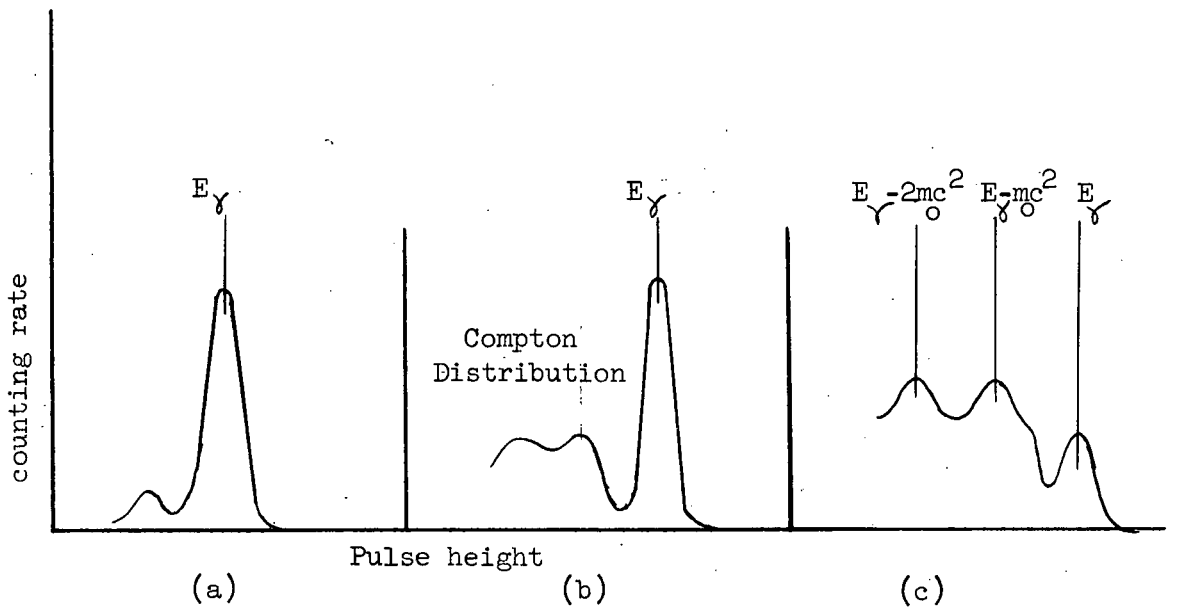

Fig. 10. Pulse spectrum of homogeneous gamma radiation

In Figure 10 are shown typical pulse height spectra to be expected from gamma-rays of different energies. These spectra reflect the relative importance of the photoelectron, Compton and pair-production processes within the phosphor. For $E_\gamma < 250$ Kev (Figure 10a) the photo electric effect predominates, and the pulse height distribution shows a strong full energy peak (with a lower energy 'escape' peak corresponding to the events in which the K X-ray of iodine emerges without loss from the crystal of NaI). The photopeak produced has an amplitude proportional to the energy of the gamma ray and not to that of photoelectrons because most of the X-rays emitted after the photoeffect are absorbed in the crystal and contribute to the intensity of the scintillation. For $E_\gamma > 500$ Kev but < 1.02 Mev, the compton effect is also important and the full energy photopeak is accompanied by a characteristic distribution of the recoil electrons with a well marked Compton edge (Figure 10b). For $E_\gamma > 1.02$ Mev pair production is possible and peaks will be observed at pulse amplitudes corresponding to the energies $E_\gamma - 2m_0c^2$, $E_\gamma - m_0c^2$ and E_γ respectively (Figure 10c). These three lines result because of the three possibilities. Firstly both annihilation quanta may escape leaving behind an energy equal to $E_\gamma - 2m_0c^2$, secondly one quantum of the annihilation pair may be recaptured giving rise to a line of $E_\gamma - m_0c^2$ and thirdly both quanta may be absorbed resulting in a full energy photopeak. If a very large crystal of NaI is used almost nothing escapes and the distribution will consist of only one strong peak at E_γ .

The position of these peaks permits an accurate determination of gamma ray energies. The width of the peak is statistical in origin. The pulse height (amplitude) is proportional to E and to the number of photons N produced in the phospher by an event. The latter process is a statistical process and therefore N follow a Gaussian curve with an uncertainty $\sim\sqrt{N}$. The width of the peak is hence proportional to $\sqrt{E}$.

COINCIDENCE SPECTROSCOPY

The coincidence method is designed to measure 'simultaneous' emission of two types of radiation with the help of two or more counters and a coincidence circuit which produces a count when particles arrive at the counters within a resolving time, τ. Because of its high detection efficiency, energy proportionality and fast rise-times, the scintillation detector is ideal for coincidence work.

As an example we may describe a typical simple gamma-gamma coincidence system, illustrated with a block diagram in Figure 11a. The mixer element is the Rossi coincidence circuit and is shown in Figure 11b. The gamma-ray source is placed between two detectors. Of the pulses produced in detector 1, the pulse height analyzer (P.H.A.1) can be set to select only those of a certain amplitude (i.e. energy) and these are fed into one input of the mixer-circuit. This is called the gate pulse. P.H.A.2 can be used to scan the entire spectrum from detector 2, which is fed into the other input of the mixer-circuit. The latter will produce an output pulse only if it receives pulses on both inputs which arrive within a time interval, τ. The output pulses of the mixer-circuit, then respresent the gamma-ray spectrum of detector 2 in coincidence with the gate pulse.

The chance (accidental) coincidence rate is given by

$$N_{ch} = 2N_1N_2\tau$$

where N_1 and N_2 are the total counting rates of counter 1 and counter 2 respectively and τ is the resolving time of the system. To keep N_{ch} very much lower than the true coincidence rate, it is important that τ should be as small as possible. Whereas the resolving time of the Rossi circuit alone can be made as low as 10^{-9} sec., the resolving time τ of the system of Figure 11a is never better than 10^{-6} sec. This is because the resolving time of the system is practically governed by the P.H.A. only. In the process of

To follow page 29.

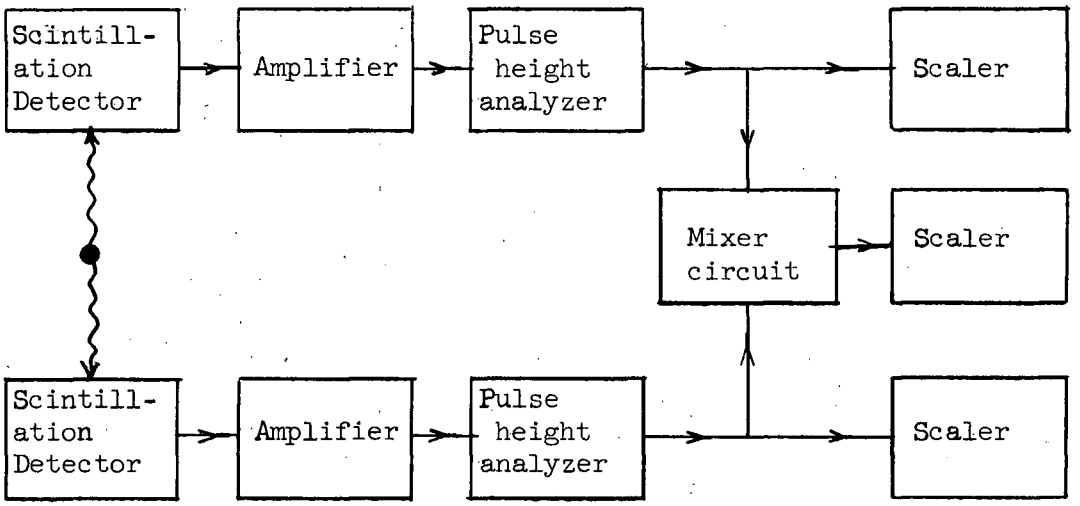

Fig.11(a). Block diagram of gamma gamma coincidence system

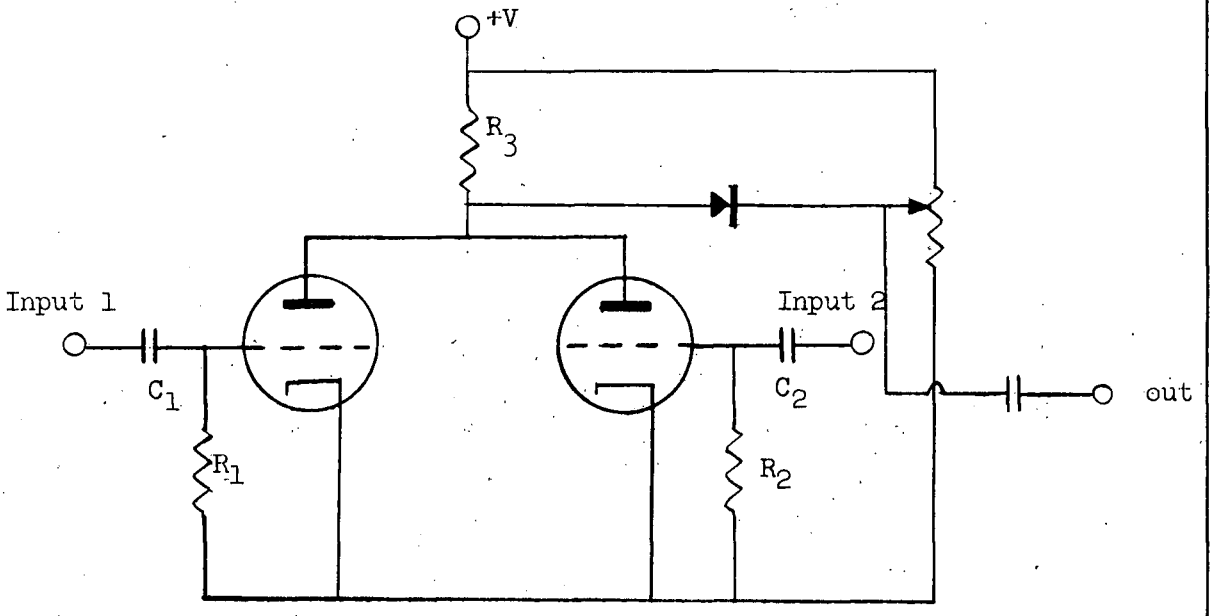

Fig. 11(b). Rossi coincidence circuit

pulse-height analysis, the P.H.A. imposes a variable delay in the output pulses depending upon the size and the shape of the input pulses. The magnitude of the time spread associated with the variable delay is $\sim 10^{-6}$ sec.

Bell, Graham and Petch[21] solved this problem by performing the coincidence selection and the pulse height analysis in entirely separate channels, and combining the results of these operations in a separate, relatively slow coincidence circuit. The system used by them is called a Fast-Slow Coincidence system and is illustrated in the block diagram of Figure 12.

The unselected pulses from the detectors are fed into the fast coincidence circuit whose resolving time may be 10^{-9} sec. At the same time detector pulses are also amplified, analyzed and fed into the so-called slow coincidence circuit with a resolving time $\sim 10^{-6}$ sec. At the end of the chain the triple coincidence unit selects, out of all the fast coincidences originally formed, only those that are in coincidence with the outputs of the two slow channels. In this way the full speed of the detectors is preserved and at the same time pulse height selection is carried out without affecting the fast response of the Rossi circuit. The resolving time of the fast-slow coincidence system is determined by the fast coincidence circuit alone.

Coincidence spectrometry is a very useful and widely used technique in nuclear spectroscopy.

When dealing with a complex beta spectrum with several beta rays, the beta gamma coincidence technique is far more relaible for determining the upper energy limit and the spectral shape of the beta transitions than is the conventional Kurie analysis approach. The reason is that by a proper choice of gating pulse, some of the beta groups are eliminated leaving the Kurie analysis to deal with a simpler picture. Similarly, the use of gamma-gamma coincidence measurements can sometimes isolate a single component from a composite gamma ray peak in the singles spectrum.

To follow page 30.

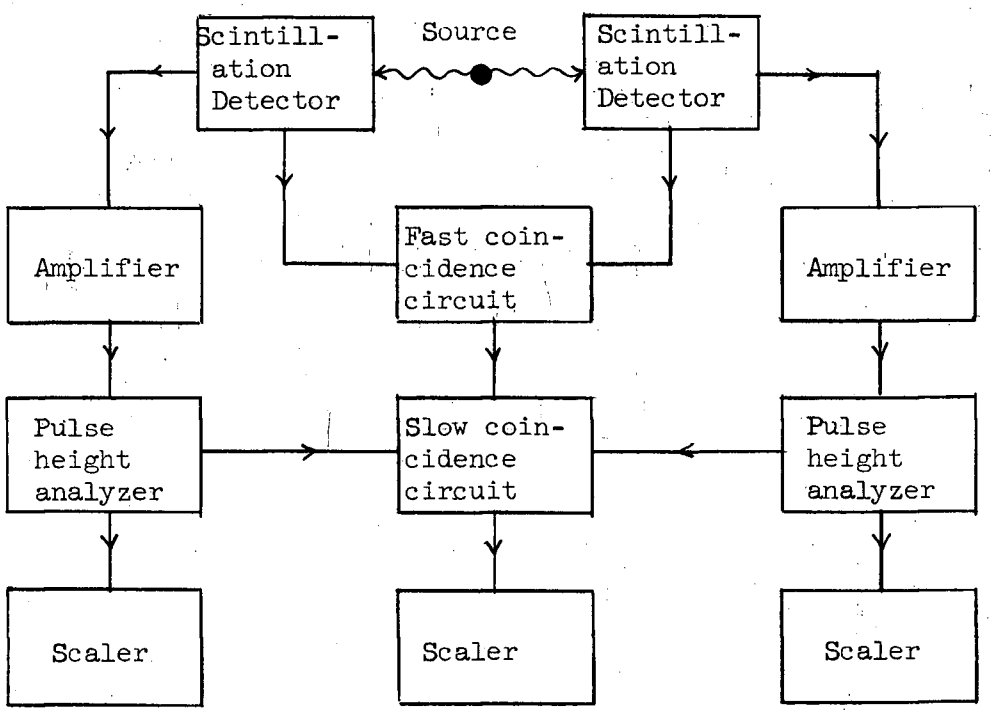

Fig. 12. Fast-slow coincidence system

Coincidences may also be measured between conversion electrons and gamma rays which would appear to have attractions over gamma-gamma measurements. This method exploits the high resolutions obtainable with magnetic spectrometers. However, the results are usually of qualitative interest only and merely assist in deducing decay sequences. Directional correlation effects may be large and generally unknown unless a prior determination of the spins and parities of the levels has been made.

Gamma-Gamma Angular Correlation

It has been shown theoretically that the angle between the directions of emission of two photons emitted in cascade depends upon the spins of the nuclear levels connected by the two photons. For example, if one gamma ray γ_1 is emitted in a particular direction $\bar{r}_1$, the probability of the emission of the second gamma ray γ_2 in the direction $\bar{r}_2$ is a function of the angle between $\bar{r}_1$ and $\bar{r}_2$ (say, θ).

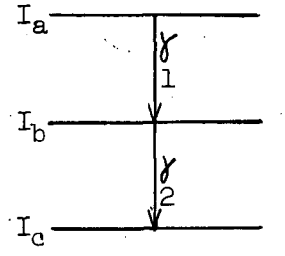

Figure 13. Two γ-rays in cascade

A convenient form for expressing the directional correlation $W(\theta)$ between γ_1 and γ_2 is:

$$W(\theta) = 1 + A_2P_2(\cos\theta) + A_4P_4(\cos\theta) + \ldots A_vP_v(\cos\theta) + \cdots \qquad (34)$$

The coefficients A_v depend upon five parameters; the multipole orders L_1 and L_2 of the gamma rays and the spins I_a, I_b, and I_c of the nuclear levels. The maximum value for v is established by the condition,

$$v_{max} = \text{Min } (2L_1; 2I_b; 2L_2) \qquad (35)$$

Calculations of the coefficients A_v in (34) for various combinations of the spin and multipole order parameters have been made by Biedenharn and Rose[22].

Gamma-gamma angular correlations are obtained by fixing the direction of one detector and moving the other through small angular steps and recording the coincidence counting rate at each step. A least square fit to the data of a function of the form (34) then yields values for A_ν which can be compared with those calculated theoretically. If multipolarities of the gamma rays concerned are known from some other source (the internal conversion coefficients, say) then the experimentally measured values of A_ν can be extremely helpful in establishing the spins of the levels involved. If they are not known, then a trial-and-error procedure must be used to determine which parameters best fit the results.

CHAPTER III

THE THIN LENS MAGNETIC SPECTROMETER

Introduction

This spectrometer uses a bell-shaped field produced by a relatively short (compared with the source to detector distance), axially symmetric magnetic coil (Figure 14). The source and the detector are located along the coil axis on opposite sides of the coil and outside the region of high field.

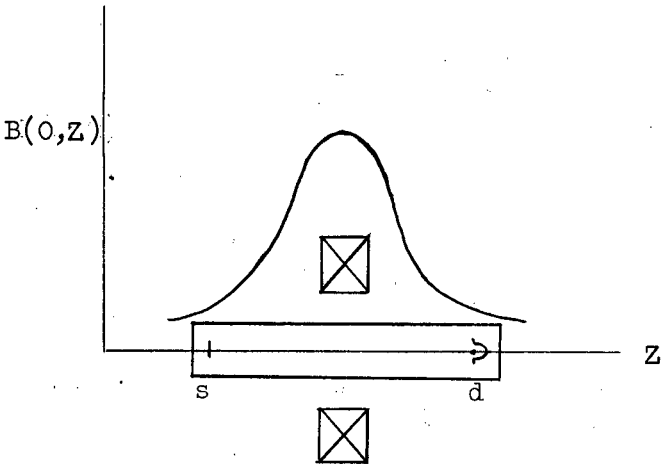

Figure 14. The bell-shaped field in a thin lens spectrometer.

In this spectrometer analogies with optical lenses have been much used Busch[23] first pointed out that the ordinary lens formula $\frac{1}{f} = \frac{1}{u} + \frac{1}{v}$ is applicable in this case and showed that

$$\frac{1}{f} = \frac{1}{4(B\rho)^2} \int_{-\infty}^{+\infty} B_Z^2 (0,Z)dz \qquad (36)$$

where $B(0,Z)$ is the axial field component and $B\rho$ is the electron momentum.

Deutch, Elliott and Evans[24] carried out a detailed study of the thin lens spectrometer and showed that

$$f = C\left(\frac{p}{ni}\right)^2 \qquad (37)$$

where p is the electron momentum, ni is the ampere-turns, and C is a constant depending upon the shape and size of the magnet coil. Thus, for a fixed geometry, the momentum of the focused electron is proportional to i.

Figure 8 shows the radial displacement of typical trajectories for a short lens field. It is obvious that even for a narrow range of emission angles, the axial focus is much extended, a fact which demands detectors of

large size. The disadvantage may be minimized to some extent by using low emission angles, and a symmetrical geometry of source and detector, but this inevitably leads to low transmission and dispersion, and hence to poor resolution.

Even so, the thin lens spectrometer possesses certain distinct advantages over other types. It is inexpensive and easy to construct. The source and detector, both lie outside the high-field region and are easily accessible, so that it is readily adaptable to beta-gamma coincidence work.

An unmodified thin lens spectrometer, with symmetrical geometry and axial detection has a transmission of approximately 0.3% with a resolution $\sim$3% in momentum, characteristics which suffer in comparison with, for example, the Siegbahn-Slatis intermediate image spectrometer. However, the possibilities of the thin lens are too tempting to discard it, and from time to time, attempts have been made by various workers in this laboratory and elsewhere, to improve its performance.

THE MODIFIED THIN LENS SPECTROMETER

In Figure 8, the electron trajectories reach a region of maximum convergence off the axis before coming to an 'extended' focus along the axis. The envelope of this convergence forms a ring in a plane perpendicular to the magnetic axis. This is the well-known 'ring focus', which has been exploited by many workers[25-28] in the past. Keller et al[26], for example, inserted suitable baffles at the position of the ring, and with an axial detector found that for the same resolution, the transmission increased by a factor of two.

Mann and Payne[29] took advantage of the ring focus property but in a different way. Their attack was to place the detector not on the axis, but at the position of the ring. Their detector will be described in detail later, but briefly, it consisted of a ring of anthracene crystals coupled to a

photomultiplier. Detection thus takes place before the electron beam diverges again past the ring focus. This arrangement made it possible to use greater ranges of emergence angles α. It is well-known that the transmission increases as α^2 and the resolving power as α. The physical size of the vacuum chamber will limit α if a symmetric geometry is used. With ring detection, the symmetric geometry may be discarded, and the source moved closer to the magnet. Using these modifications, Mann and Payne achieved a resolution $\sim$ 1.24% with a transmission $\sim$ 1.1%.

Mann and Payne began their investigations by first computing a large series of trajectories for the thin lens field after the method of Deutch et al[24]. The calculations were made by the computing center of the University of Toronto. From the families of curves of which Figure 8 is an example, the position and nature of the ring focus was found to be a sensitive function of

(a) source-to-magnet distance s,

(b) detector-to-magnet distance d,

(c) mean emission angle α, and

(d) angular divergence $\Delta\alpha$.

The ring focus radius was fixed at 5.0 cm., a value chosen for convenience because of the vacuum chamber size, and each of the four parameters was varied independently in a systematic way. They placed in front of the ring detector and at the position of the ring focus, annular exit baffles of variable slit width. At each position, a line profile of the K-conversion line of Cs137 was taken. In all cases, the object was to determine the values of the four parameters which would produce the best line, i.e., maximum peak height consistent with minimum peak width. They were limited to some extent in their search by the length of their vacuum chamber, and by a lack of adequate controls for variations of s and d, and as a result, they were not certain that the results they achieved were necessarily the ultimate attainable with the magnet used.

Chaturvedi[30] recognized that precautions should be taken to ensure alignment of the source-detector axis with the magnetic field axis, since otherwise, the arrangement could not be axially symmetric. He designed a vacuum tube mounting which could be sensitively and accurately controlled. With this, it was possible to rotate the tube about any axis. Mann and Payne had provided a source centering mechanism, whereby the source position could be adjusted in a plane perpendicular to the spectrometer axis, but Chaturvedi was still limited in detector position control.

A schematic diagram of the spectrometer used in the present work is shown in Figure 15. The vacuum chamber length has been increased by 50% and the detector is mounted on a cylinderical carriage inside the vacuum chamber with ball-bearing rollers and position controlled by an external rod passing through a vacuum seal. This gives a smooth and easy access to the detector. Parameters s and d are continuously adjustible with this device and with the axial movement of the vacuum chamber, which is mounted on rollers on the Chaturvedi supports, and can move freely into and out of the magnet. With these modifications, the work of Mann and Payne was repeated, but with greater ranges of the four parameters.

Details of the ring detector are shown in Figure 16, and except for the controls, it is the design of Mann and Payne. The 5" photomultiplier (Dumont 6364) was selected from several for the smallest dark current, and is coupled to the anthracene ring by a shallow lucile light pipe cut to a critical reflection shape. The anthracene is fitted to a shallow (3/16" deep by 1/4" wide) circular ring cut into the lucite. The lucite and anthracene are coupled by a mixture of glycerine and Ivory soap, a mixture with good optical properties which flows freely when warm, but which is solid at room temperature. The lucite is coupled to the face of the photomultiplier with a mixture of silicone gel (DC 400) and silicone oil.

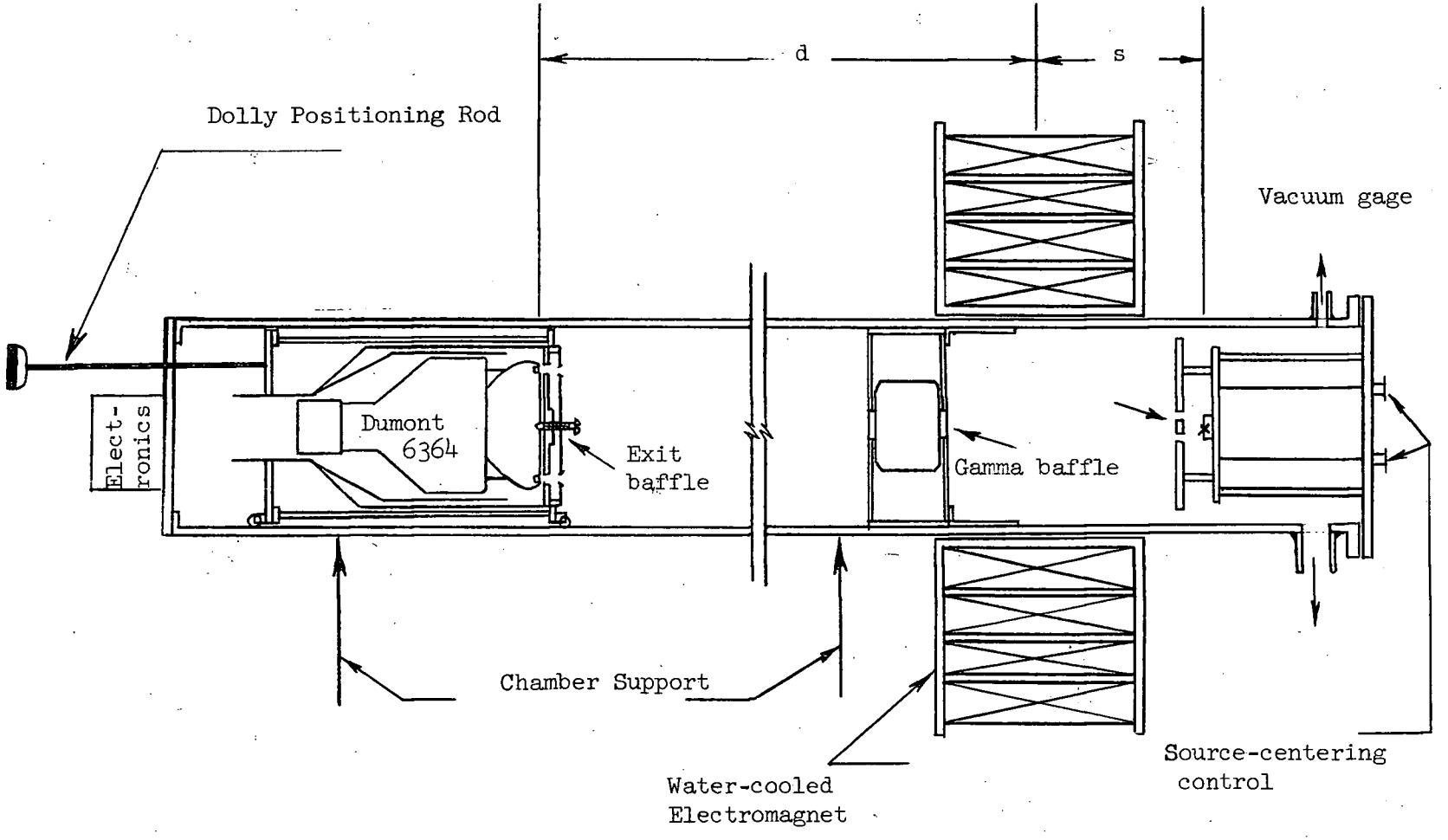

Fig. 15. Modified thin lens spectrometer.

To follow page 36.

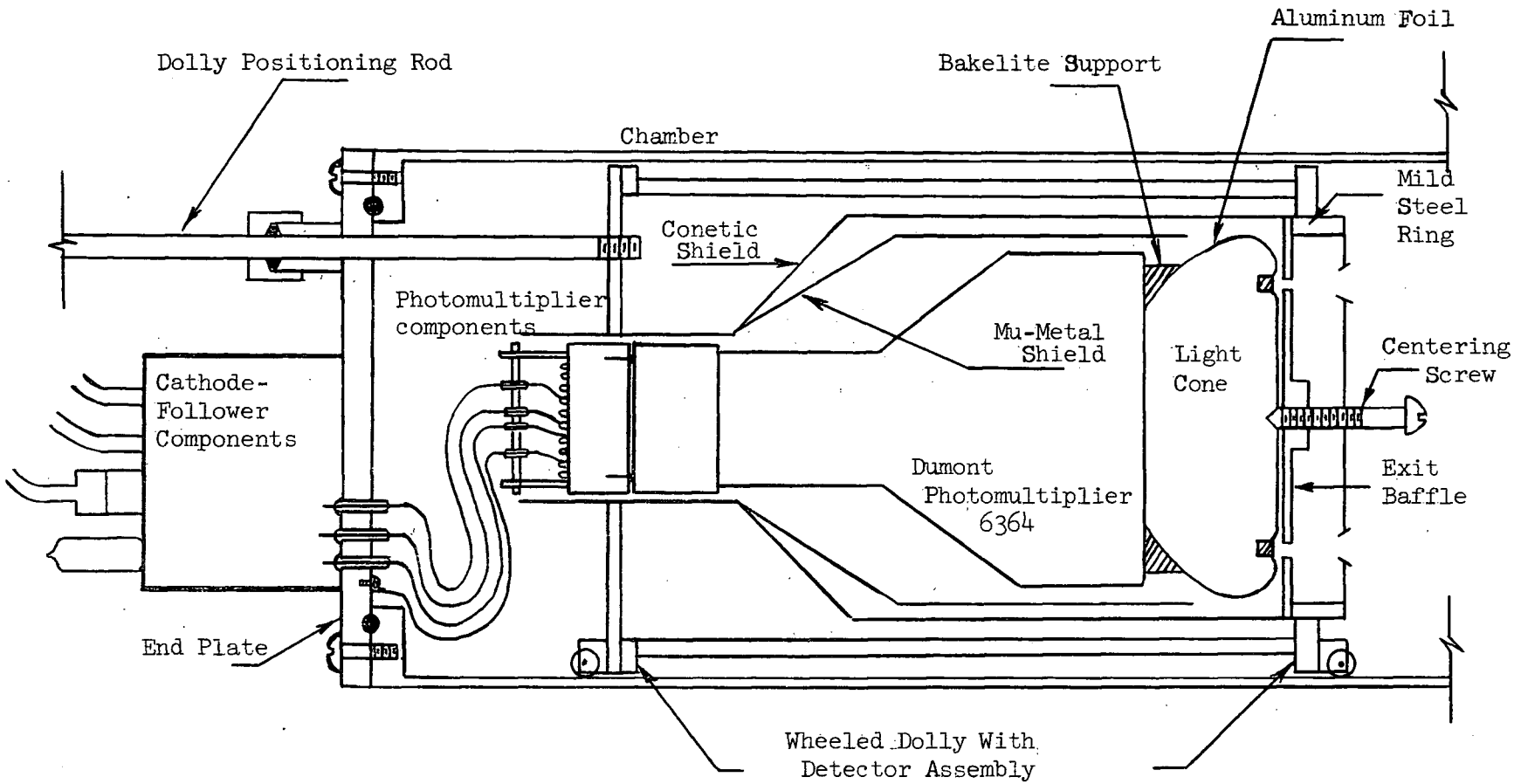

Fig. 16. The Detector Assembly

To follow page 36.

The photomultiplier is shielded from the residual field of the magnet by placing a mu-metal shield around the photomultiplier itself, and then by surrounding the entire detector assembly with a Fernetic-Conetic* jacket. Figure 17 shows the effect of this shielding arrangement as a function of magnet current. The first effect of the field occurs when the field strength is adjusted to focus electrons of approximately 600 kev. This field effect appears to be constant with time and shows no detectable hysteresis.

The entrance and exit baffles, shown in Figure 14, are made of 1/8" aluminum. The entrance baffle system which determines α and $\Delta\alpha$ are mounted rigidly to the source holder on aluminum stand-offs. The source holder in turn is mounted on the source-centering assembly of Mann and Payne. It is a simple rack and pinion arrangement controllable from outside the spectrometer.

A lead baffle shields the detector from direct gamma radiation from the source. Other baffles are used to reduce the number of electrons and gamma-rays scattered from the chamber walls, an effect that becomes very important when strong sources are used.

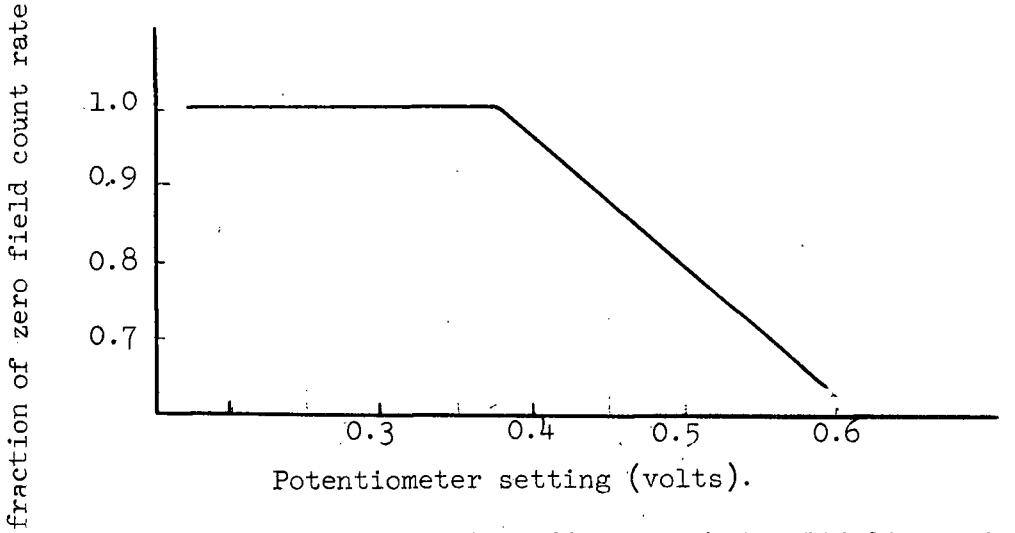

Figure 17. Defocusing effect on photomultiplier noise.

Finally to compensate for the earth's magnetic field, the entire spectrometer assembly is enclosed by large rectangular Helmholtz coils.

---

* Available from Perfection Mica Co., Chicago, Illinois.

THE ASSOCIATED CIRCUITS

(a) The Field Current Control Circuit

The electric current used to produce the focusing field was taken from a 110V d.c. generator. This current was supplied to the magnet through a regulator capable of regulation to 1 part in 10^4. This is accomplished as follows (See Figure 18). The current through the field coils also passes through a bank of 38 paralleled 6AS7-G's and a 0.1 ohm standard resistance made of manganin strip. The voltage produced across the standard resistance is compared with that from a Rubicon potentiometer. This comparison is carried out in the bias-control-circuit which feeds the required bias to the grids of the 6AS7-G's. The bias-control-circuit consists of a Brown converter-fed d.c. control amplifier having a frequency response from 0 $^c/_s$ to 20 $^c/_s$ and a gain of 30,000 in parallel with an a.c. amplifier of frequency response from $10^c/_s$ to 2000 $^c/_s$ and a gain of 10,000. A complete circuit diagram of the bias control circuit is shown in Appendix 2, Figure A5.

(b) Beta Spectra Counting Circuit

A block diagram of the counting circuit is shown in Figure 19.

The collector output of the photomultiplier is fed to a cathode follower to match the impedance of the signal cable leading to linear pulse amplifier (Tracerlab amplifier, model RLA-1). The amplified pulses are counted with a standard scale of 64. High voltage for the photomultiplier is provided by a John Fluke Manufacturing Co.,Inc., Seattle (U.S.A) Power supply, model 402M. The voltage supply circuit for the photomultipler is shown in Appendix 2, Figure A6.

SPECTROMETER ADJUSTMENT

The source used for calibration and adjustment was Cs137. This source has an isolated K-conversion line of 3381.28±0.5 gauss-cm. corresponding to a 661 Kev transition. The Cs137 was obtained from Chalk River in the form of $CSNO_3$ dissolved in HNO_3. A beta source was prepared by depositing a drop of the

To follow page 38.

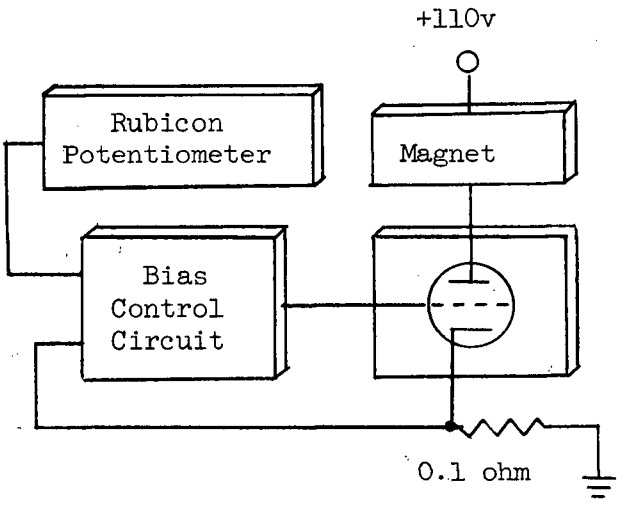

Fig. 18. Control Circuit

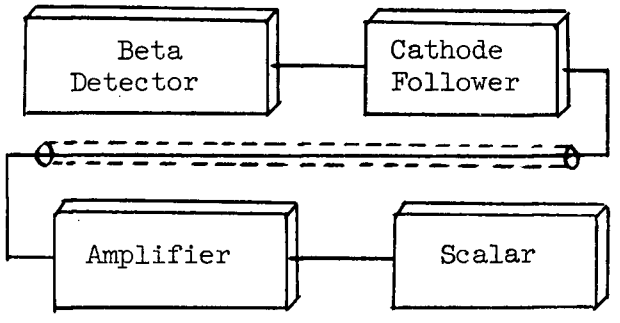

Fig. 19. Counting Circuit

solution on a 240 $\mu gm/_{cm^2}$ thick aluminum foil and allowing it to dry. It was then covered with a thin film of collodion to contain the active material.

Discriminator Level Setting

In any photomultiplier there are always some 'dark' pulses or 'noise'. It is important that the signal-to-noise ratio should be as large as possible. For electron energies above a few hundred kev the signal-to-noise ratio for the photomultiplier used is high and in consequence the discriminator level can be adjusted for low background (noise) with no loss of counts. With low energy electrons, however, the signal pulses overlap the noise pulses to some extent and hence a lower discriminator setting is necessary to 'dig' out the signal. In beta spectra, we must deal with a continuum of energies from low to high and under these circumstances, it is advantageous to use different discriminator settings for different small ranges of electron energies. For any particular small range of electron energies the discriminator setting is determined by measuring the peak height of a conversion line as a function of discriminator setting or noise level. As the discriminator level is lowered, the number of significant signal pulses increases until it reaches its maximum value. Further lowering the discriminator level leaves the significant peak-height unaffected. The plot of peak height vs. noise is thus a plateau-shaped curve, the knee of which determines the discriminator setting at the energy of the electrons to be focused. One such graph is shown in Figure 20.

For measuring spectra covering a large energy range, the knee-points determined for energy intervals beginning with energy E result in a curve of the type shown in Figure 21 and from this, the optimum discriminator setting at any energy may be found.

Spectrometer Alignment

The following procedure was adopted as the most reliable.

(a) The source is positioned in its mounting so that it lies in the centre of the spectrometer end-plate. A special jig was constructed for this purpose.

To follow page 39.

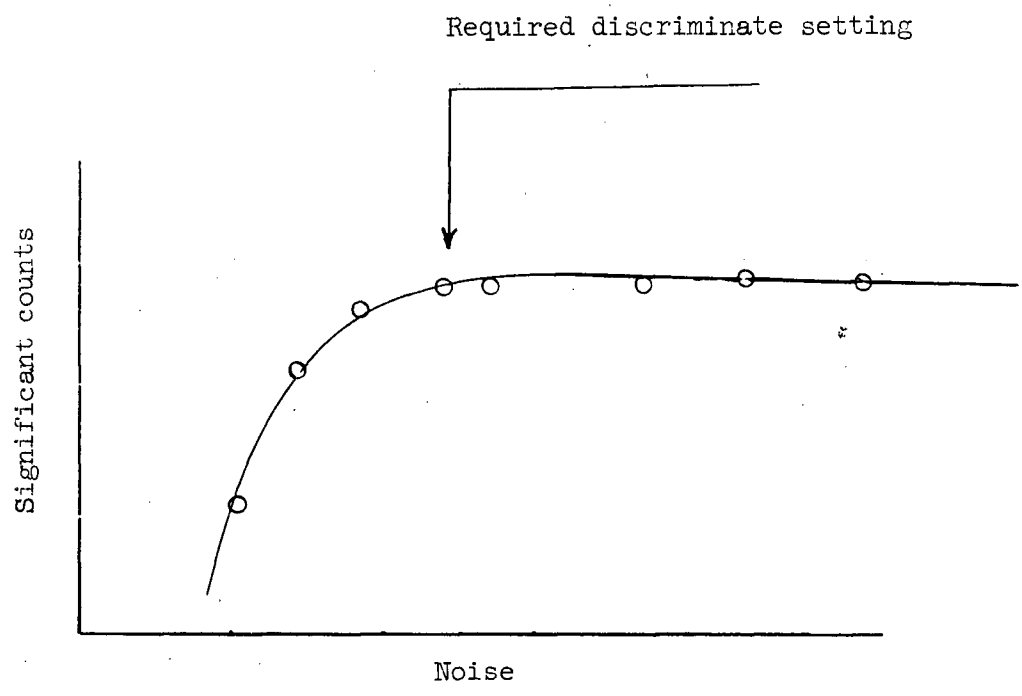

Fig. 20. Typical discrimination plateau.

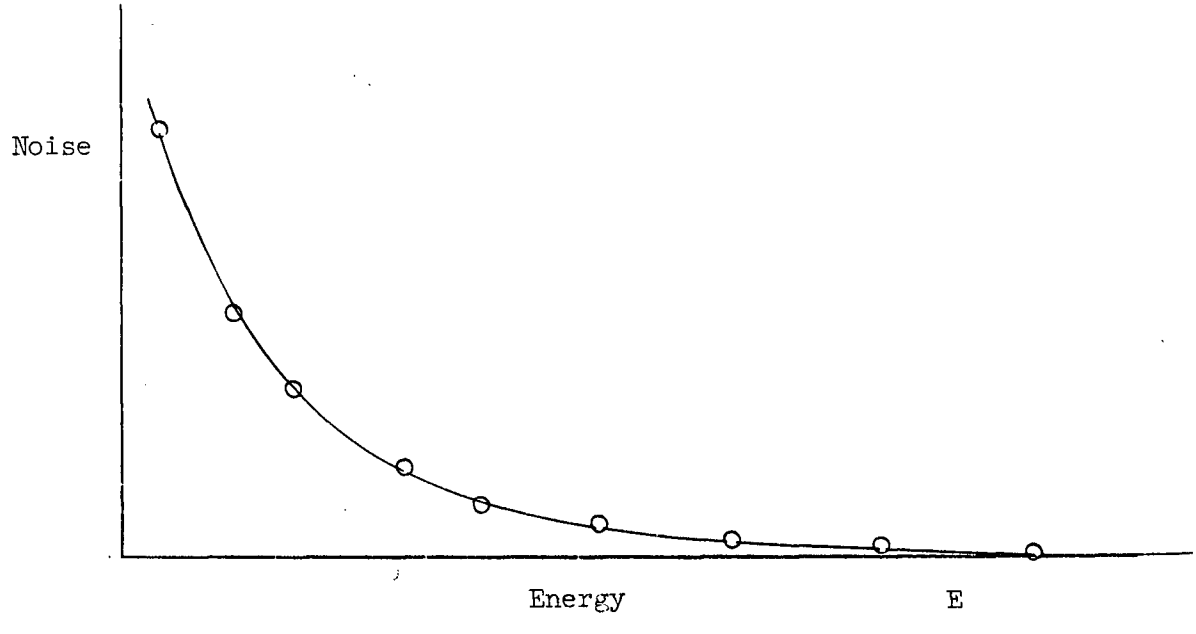

Fig. 21. Noise level setting corresponding to different electron energies.

This does not ensure that it lies on the magnetic-axis.

(b) The vacuum chamber is then visually centred to make it reasonably concentric with the circular opening in the magnet.

(c) The position of the source is next varied with the rack and pinion arrangement and the peak profile of the conversion line is studied as a function of the source position. The position of the source corresponding to the maximum peak-height attained is then used in subsequent adjustments.

(d) Following an optical analogy, it is apparent that the performance of the instrument will be optimum when the source-detector axis and the geometric axis of the vacuum chamber coincide or, at least, intersect each other at the magnet-centre (lens-centre). Whereas the above three operations may bring the ring focus into coincidence with the scintillation detector, they may not fulfil this condition. For this reason the vacuum chamber is rotated around an axis through the magnet-centre and the peak-height of a conversion line studied as a function of the angular displacement of the vacuum chamber. The position of the vacuum chamber corresponding to the maximum peak height is then taken as the correct position for both vacuum chamber and source. The spectrometer is now ready for tests.

Variation of the Parameters

The parameters α and $\Delta\alpha$ are determined by the size and position of the entrance baffles. Six mean emergent angles were chosen, such that the mean tangent of α (and the associated gathering powers ω), were 0.2498(1.1%), 0.3030(1.2%), 0.3384(1.13%), 0.3481(1.17%), 0.3685(1.09%) and 0.3834(1.1%). It had been intended to keep the gathering powers constant for all six baffles, but after they had been cut, their calculated gathering powers showed the above variations. We found that for higher mean tangents and larger gathering powers, the vacuum chamber walls interfered with the beam. In principle, this can be overcome by a smaller value of s, but with our arrangement, it was physically impossible, because of vacuum pump connections, to reduce s sufficiently for higher mean tangents than 0.3834.

For each entrance baffle, and with a wide open exit baffle, s was varied in steps of 0.5 cm. At each such position, the line profile of Cs^{137} was measured as a function of detector position d. An example of the results for a particular value of s is shown in Figure 22 and Figure 23. A comparison of such curves for all source positions enabled a choice of optimum s and for that particular entrance baffle, and the spectrometer was set on these.

Then the exit slot width was reduced in steps to obtain a 'match' between the focused beam and the exit baffles. Where the exit slot is too wide, the transmission is determined by the beam width, and the line width by the exit baffles. Reducing the slot width has no effect upon the transmission until the match point is reached, although the line width steadily decreases. When the exit slot becomes narrower than the beam width at the focus, the line height drops and the line width stays constant, since the latter is now determined by the width of the focused beam. Figure 24 represents a typical set of line profiles. This procedure was followed with all entrance baffles. Table I is a summary of the results. In Table II, we compare the results with those of Mann and Payne, in the only two cases where the same mean tangents and gathering powers were used.

It is obvious that in spite of the greater flexibility of control available in this survey, the performance of the spectrometer has not been significantly improved, and we are forced to conclude that we have reached the optimum settings for the thin lens magnet used. It is most probable that the limit reached is imposed by the fact that the field itself is not radially symmetric. No special precautions were taken with the windings of the coil. If this symmetry is not present, then the ring focus will not be a true circle and no circular exit baffles can properly match it. The only possibility for further improvement would be to use precision techniques in winding the coil, e.g., square cross-section wire with accurate controls of turn radius.

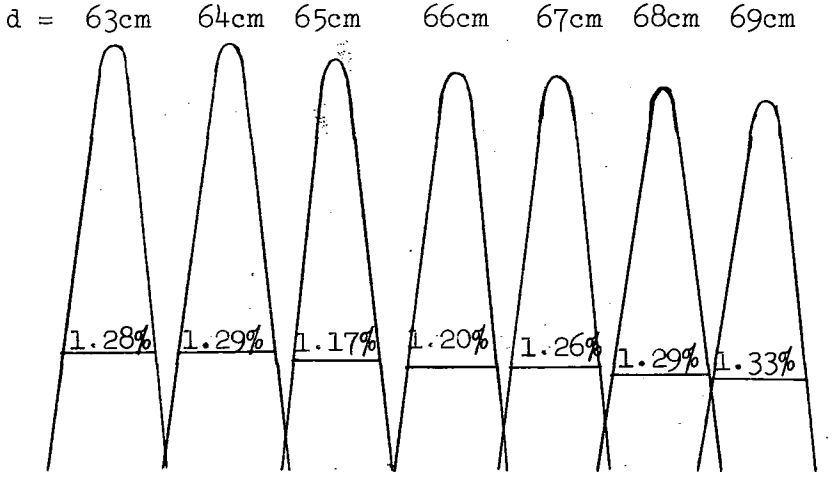

Fig.22. Variation of peak shape with detector distance.
(M.T.=0.3481, ω=1.17%, slot=3mm, s=20.5cm)

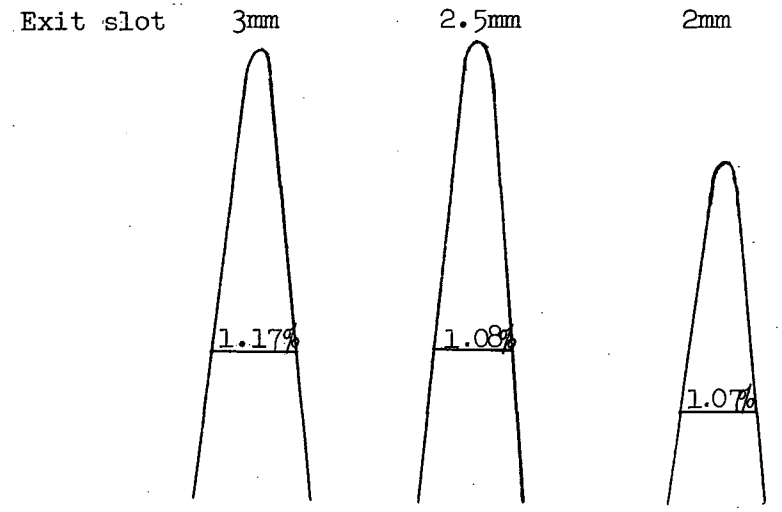

Fig. 24. Graph showing 'match' condition
(M.T.03481 , ω=1.17%)

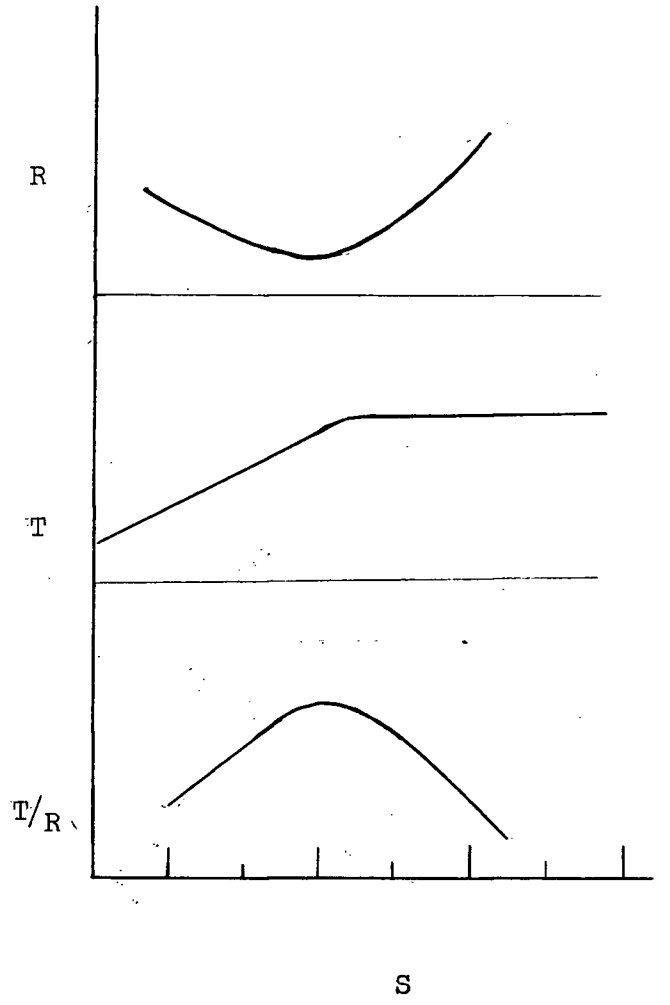

Fig. 23. Variation of R, T and $T/_R$ with s

To follow page 41.

TABLE I

Results of Calibration Measurements

Mean tan	ω%	R%	T(arbitrary units)	$\frac{T}{\omega}$	$\frac{T}{\omega R}$
0.2498	1.1	1.39	29	26	19
0.3030	1.2	1.20	42	35	29
0.3384	1.13	1.09	38	34	31
0.3481	1.17	1.07	40	34	32
0.3685	1.09	1.02	31	28	27
0.3834	1.1	1.03	34	31	30

Table II

Comparison of present work with that of Mann and Payne

	$(\frac{\omega}{R} \times 100)$	
Mean tan	Present work	Mann and Payne
0.3834	106	83.
0.3481	109	89.

CHAPTER IV

THE DECAY OF Cs^{134}_{55}

The 2.3 year negatron decay of Cs^{134}_{55} to Ba^{134}_{56} has been investigated during the past few years by a great many workers[31-52] and while agreement has been reached on certain aspects of the decay, there are still many differences in the proposed schemes that require clarification. The published decay schemes are becoming increasingly complex as authors present evidence for new beta and gamma ray transitions which have not been noted before.

Fig.25(a) shows those levels and transitions in the decay that are generally accepted. Fig.25(b) indicates other levels and transitions that have been reported from time to time by some laboratories. While this work was in progress, the two most recent papers appeared. Van Wijngaarden and Connor[52] have analyzed the decay of Cs^{134}, paying particular attention to the preparation of the beta source. They report that if the source and backing are too thick, back scattering gives evidence of beta-groups at 410 and 280 kev which almost entirely disappear when thinner sources are used. With the thinnest sources, they could not detect any of the transitions of Fig.25(b) and have been able to place very small upper limits on their intensities. They conclude that the decay scheme of Fig.25(a) is correct. Part of their conclusions has received independent support from the work of Schriber and Hogg[51] who examined the decay using a sum coincidence spectrometer. Their results indicate only the presence of the levels in Fig.25(a), and that therefore the only beta-groups with end-point energies less than 662 kev are those of energies 410 and 89 kev.

EXPERIMENTAL PROCEDURES

The Cs^{134} used in our measurements was obtained from Oak Ridge National laboratory where it had been prepared by the $Cs^{133}(n,\gamma)Cs^{134}$ method. It was received in the form of $CsCl$ in HCl solution. A small quantity of this

To follow page 43.

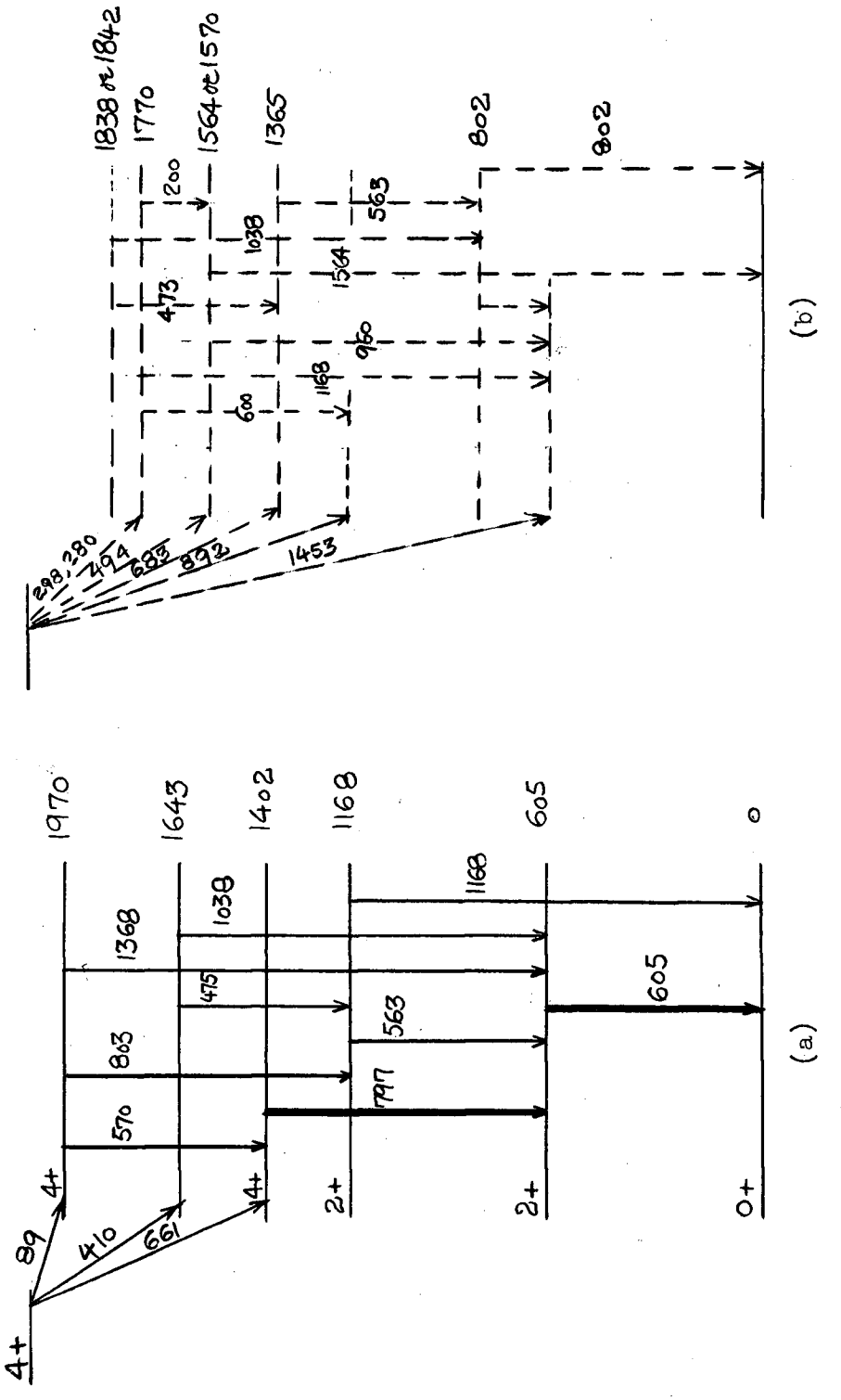

Fig. 25 Decay of $^{134}_{55}Cs$

solution was evaporated to dryness and then dissolved in distilled water. The resultant solution was practically acid-free. A drop of this solution was deposited on a thin aluminum foil (150 $\mu gm/cm^2$) and evaporated to dryness. It was then covered with a thin film of collodion to keep the active material in place. This source was used for the measurement of beta, gamma, internal conversion and coincidence spectra. This is the type of beta source that Van Wijngaarden and Connor[52] predict will show spurious beta groups.

For the preparation of photoelectron source, a specially designed brass capsule, as shown in Fig.26, was used. The active material, in full concentration, was deposited into the capsule, evaporated to dryness and covered with a thick layer of collodion. The thickness of the brass between the source material and the radiator was 0.75 mm which is adequate to absorb all expected primary betas and conversion electrons. The radiator was a circular disc of lead, 4 mm. in diameter and 15 mg/cm^2 thick, fixed to the brass capsule as shown in Fig.26.

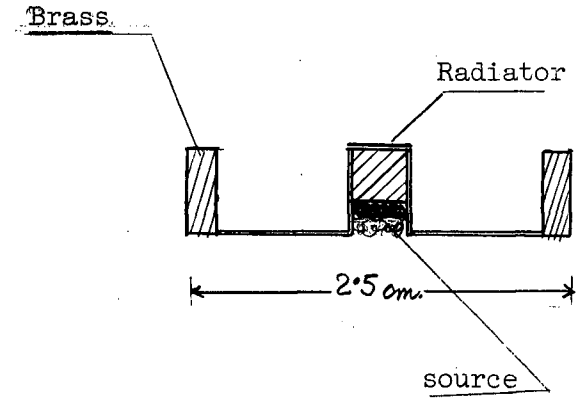

Fig.26 Photoelectron source.

For beta and conversion electron measurements, the modified thin lens spectrometer was set for a line-width of 1.5% in momentum and a gathering power of 1.61%. The large photoelectron radiator gave wider lines, and in these measurements, the photoelectron line widths were approximately 3%.

Gamma-ray singles spectra were taken with the source in position in the spectrometer as shown in Fig.28. The gamma-detector was a $1\frac{1}{2}$" x 1" NaI(Tl) crystal assembly, optically coupled to an RCA 6342 photomulitplier by a $5\frac{1}{2}$" long lucite rod (Fig.27). This arrangement moved the photomultiplier back from the strong field of the spectrometer magnet and at the same time kept the

To follow page 44.

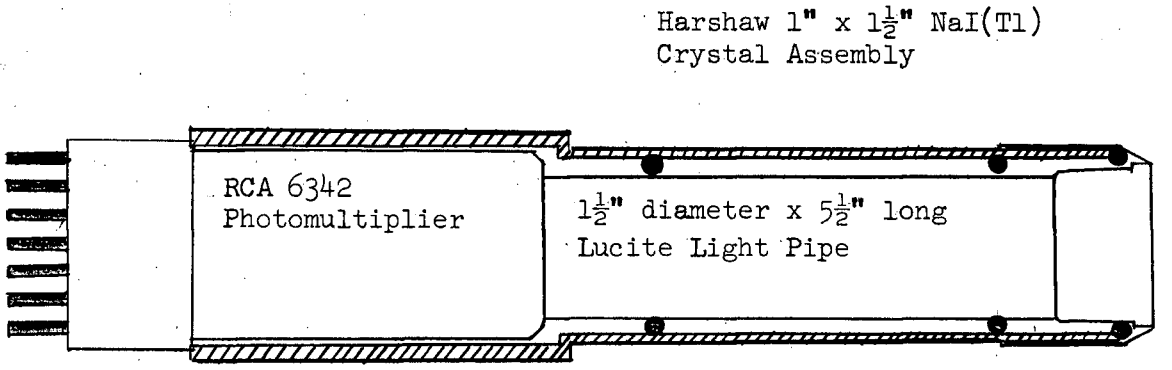

Fig. 27. Gamma Ray Detector Used in the Beta-Gamma Coincidence Measurements

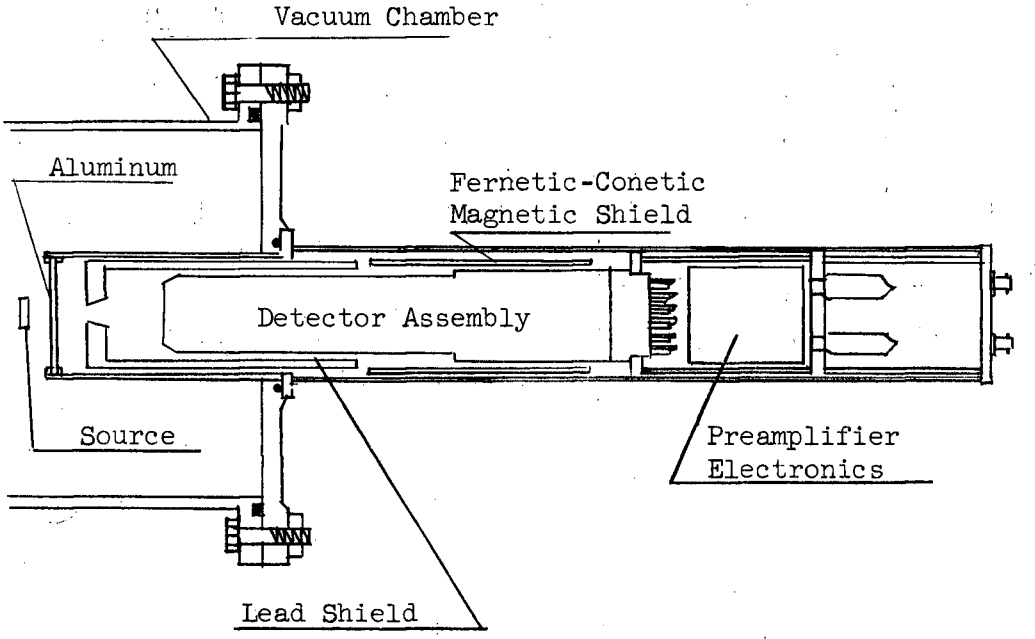

Fig. 28. Gamma Ray Detector Assembly in the Magnetic Spectrometer.

NaI(Tℓ) crystal near the source. The residual magnetic field effect on the photomultiplier was further reduced by surrounding it with a Fernetic-Conetic magnetic field jacket. Even with this protection, the gamma-ray pulse heights were affected by the field, but to a small extent only, and the effect was not troublesome.

A lead shield was placed around the crystal to reduce the scattered gamma-radiation reaching the crystal from the surrounding brass. This shield was only partly successful as evidenced by a concentration of low energy pulses in the singles spectra.

The Coincidence Systems

Two separate coincidence arrangements were used in this experiment. They will be called the gamma-beta and the beta-gamma systems and are shown in block diagram form in Fig.29 and Fig.30 respectively. Both are fast-slow systems and have some elements in common. The fast-slow mixer is a commercially available Borg-Warner unit, model DZ4 with a resolving time $\sim 10^{-7}$ sec.

The gamma-beta system of Fig.29 was designed to measure spectrometer beta pulses in coincidence with selected gamma-ray pulses. Pulses of a few millivolts amplitude from both beta and gamma detectors feed the fast inputs of the mixer. Since the latter require input amplitudes of 20 ma. into 1000 ohms, the direct pulses are first amplified and converted into standard pulses of the required amplitude and polarity by specially designed circuits called 'fast drivers', a schematic diagram of which is shown in Appendix 2, Fig.A7.

At the same time, 'slow' gamma pulses from the seventh dynode (see Appendix 2, Fig.A8) are amplified and fed to a single-channel pulse-height analyzer, whose output goes to one of the slow channels. A particular base line setting of the single channel analyzer selects from the slow gamma output, pulses corresponding to a selected gamma-ray. With this arrangement alone, the fast-slow circuit gives an output pulse whenever a spectrometer pulse is in coincidence

To follow page 45.

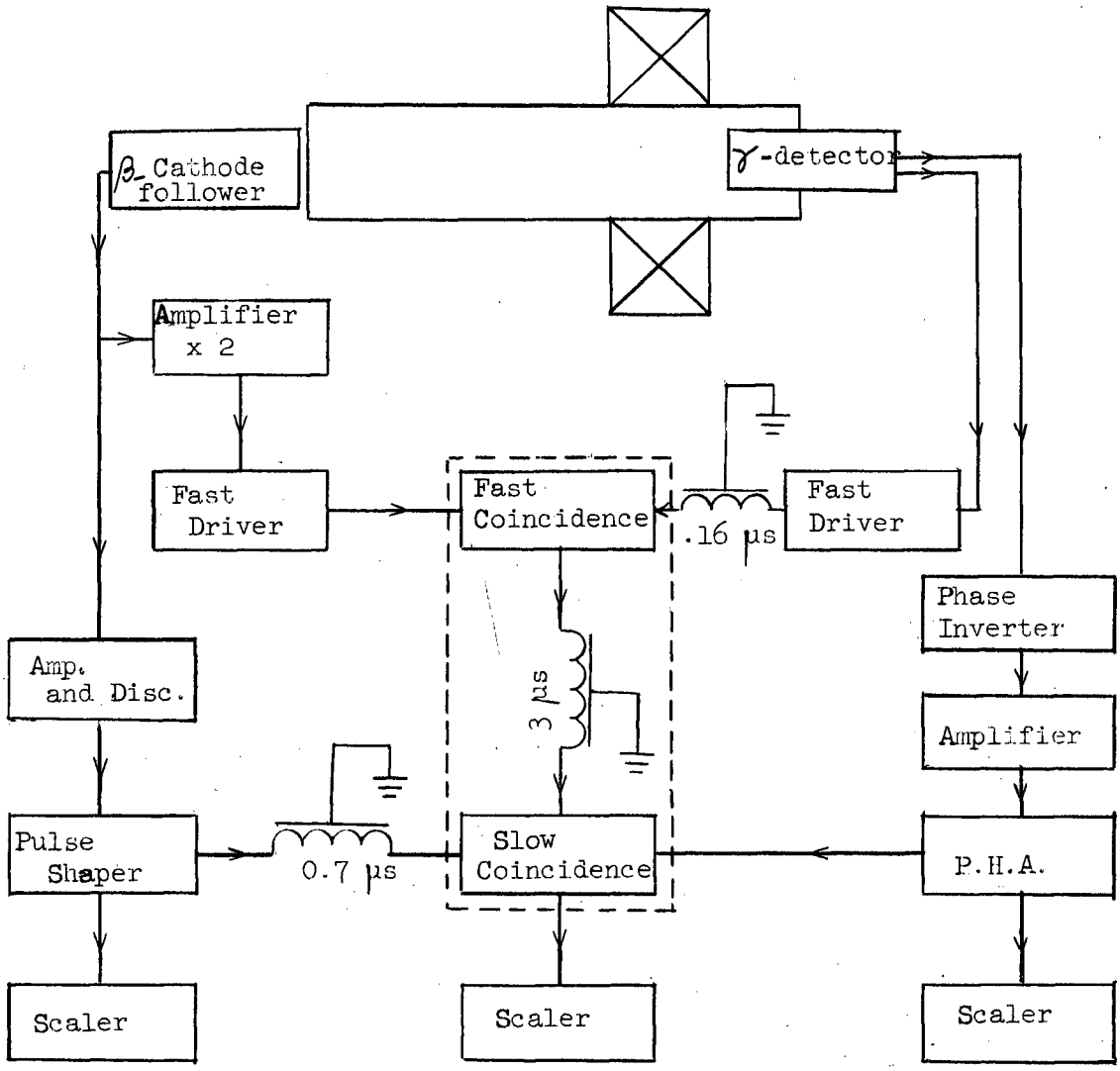

Fig.29 Block diagram of gamma-beta coincidence system

To follow page 45.

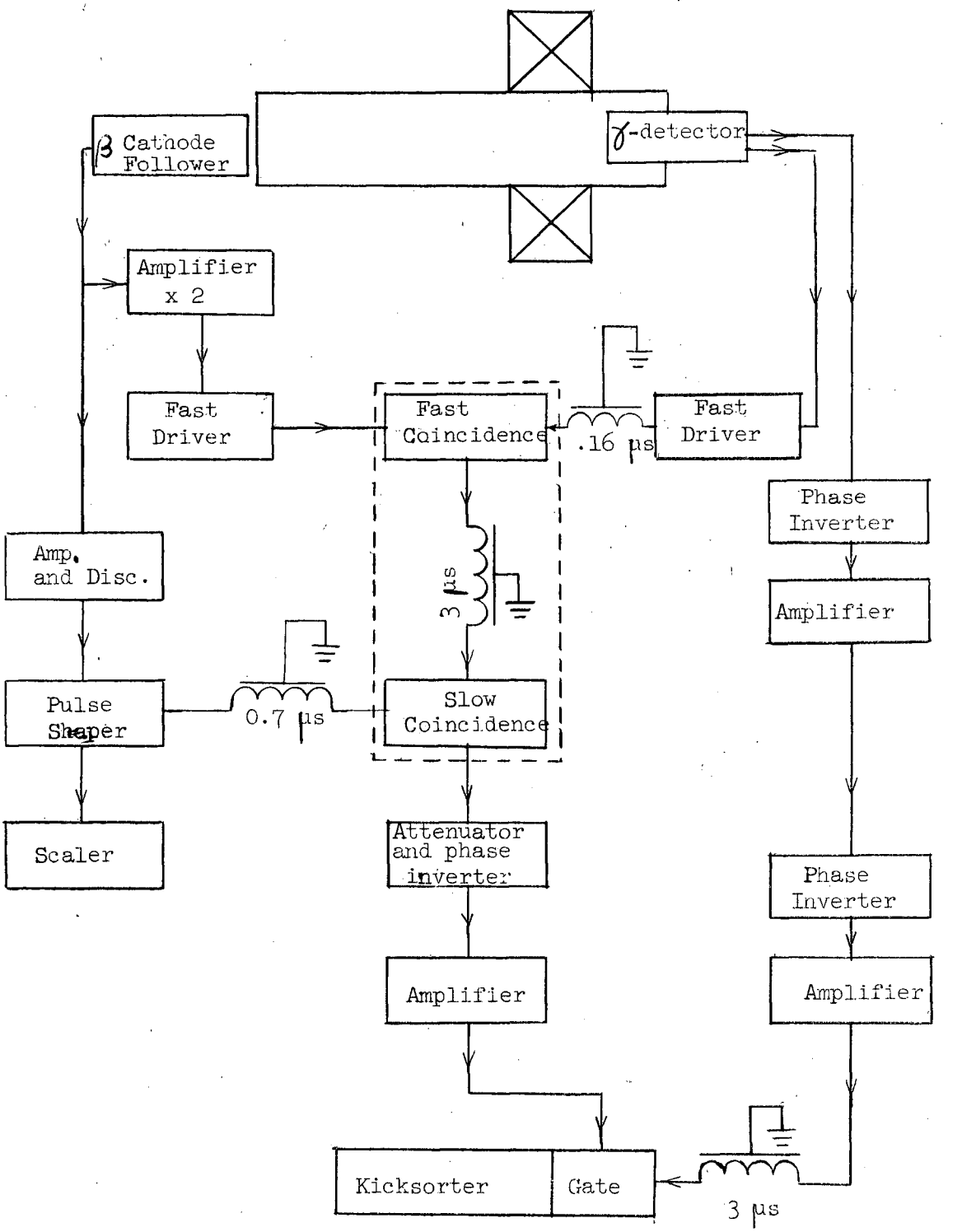

Fig.30 Block diagram of beta-gamma coincidence system.

with the selected gamma-ray. However, the fast beta pulses include photomultiplier noise as well, which contributes heavily to the chance coincidence rate. To reduce this, the beta-detector output is fed to an amplifier discriminator whose output feeds the other slow input, and the fast-slow output then represents triple coincidences between the fast sum pulses and the two slow channels. Because of amplifier, discriminator, and pulse height analyzer delays, it is necessary to incorporate into the system the proper external delays to ensure that all pulses arrive at the mixer at the same time.

The beta-gamma system of Fig.30 is designed to measure gamma-ray spectra in coincidence with selected beta-pulses. The fast inputs are the same as those of the gamma-beta system. Only the beta-slow input is used, so that the mixer output pulses represent all gamma-ray pulses in coincidence with beta pulses selected by the spectrometer current setting. This output provides a time gate to the multi-channel pulse height analyzer and only during this time is the analyzer receptive to the gamma-ray slow input. The spectrum thus analyzed is that in coincidence with a preselected beta gate. As before, external delays are incorporated to ensure the proper arrival times of all pulses.

It will be noted that a variable delay has been incorporated on the gamma-side in both arrangements. This compensates for the difference in transit time of the electrons in the 5" photomultiplier used on the beta side and the 2" photomultiplier on the gamma side. The magnitude of this transit time difference was determined by measuring the coincidence counting rate between the 605 kev K-conversion line and the 797 kev gamma-ray (which are known to be in coincidence), as a function of the delay. A typical result is shown in Fig.31.

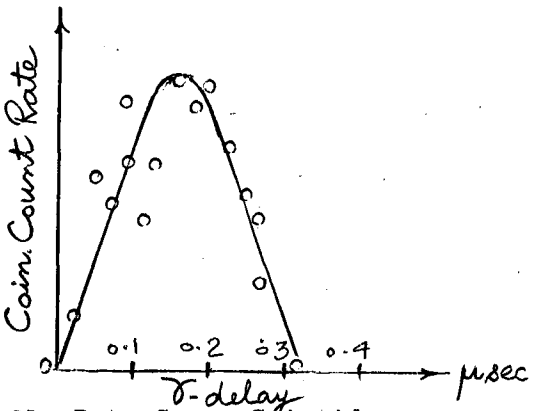

Fig.31 Beta Gamma Coincidence response as a function of delay on the gamma side.

EXPERIMENTAL RESULTS

The primary beta and conversion electron spectrum is shown in Fig.32, and Fig.33 shows the Kurie analysis of the spectrum with the conversion lines removed. The highest energy beta-group that is detectable, gives a least-squares end point of 659 ± 3 kev in agreement with the more precise measurement of 661.9 ± 0.5 kev of Van Wijngaarden and Connor[52]. The spectrum also shows two other groups with end points of 411 and 272 kev. Strong source absorption begins at ~130 kev and in consequence, the low-energy 89 kev group could not be observed. When the data of Fig.32 is replotted as $\frac{N}{p}$ vs p, the areas under each group are proportional to the group intensities. The actual counts under the 662 kev group are 2730, while the relative intensities of the 662, 411 and 272 kev groups are 100, 14, and 7.6 respectively.

Fig.34 shows the internal conversion lines taken from Fig.32 with the primary beta background subtracted. The very weak K-conversion lines corresponding to transitions of energies 1036, 1168 and 1366 kev, were difficult to measure and each experimental point in this region has a minumum counting time of 60 minutes. In this region the statistical uncertainty is approximately 15%. Also shown is a weak conversion line corresponding to a 473 kev transition. The intensities of all lines were compared by measuring the areas under each peak and dividing by the peak momentum. The results are summarized in Table IV. It is to be noted that the 605 K-conversion line includes within it a small (L+M) shell contribution from the 563, 569 kev transitions.

Fig.35 shows the photoelectron spectrum taken with the 15 mg/cm^2 lead radiator. The Compton distribution, measured with the radiator removed, has been subtracted. The spectrum was used only to relate the intensities of the 473, 563-569, and 605 gamma-rays. The intensities were compared in the same manner as for the conversion electrons except that corrections for

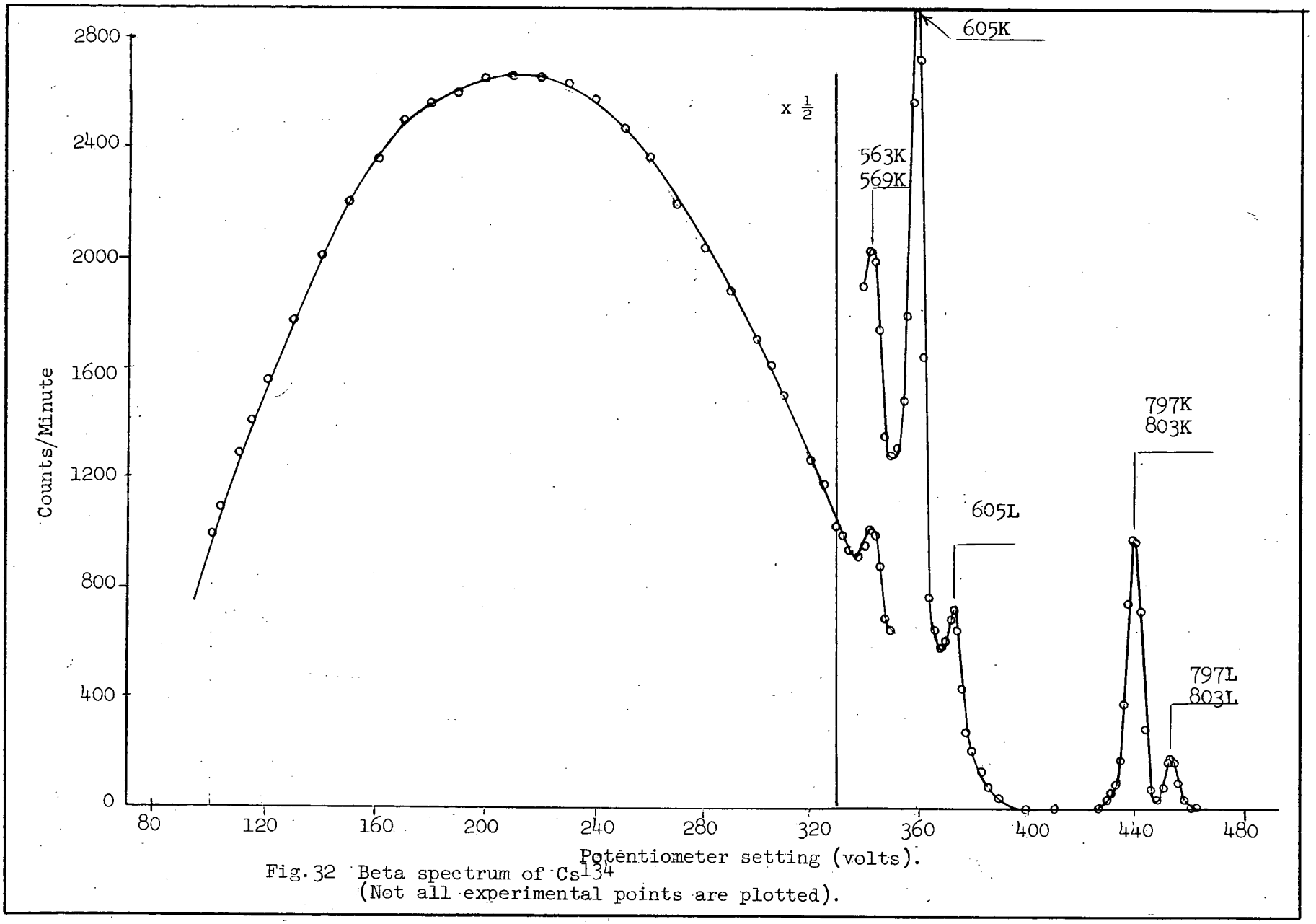

Fig. 32 Beta spectrum of Cs^{134}
(Not all experimental points are plotted).

To follow page 47.

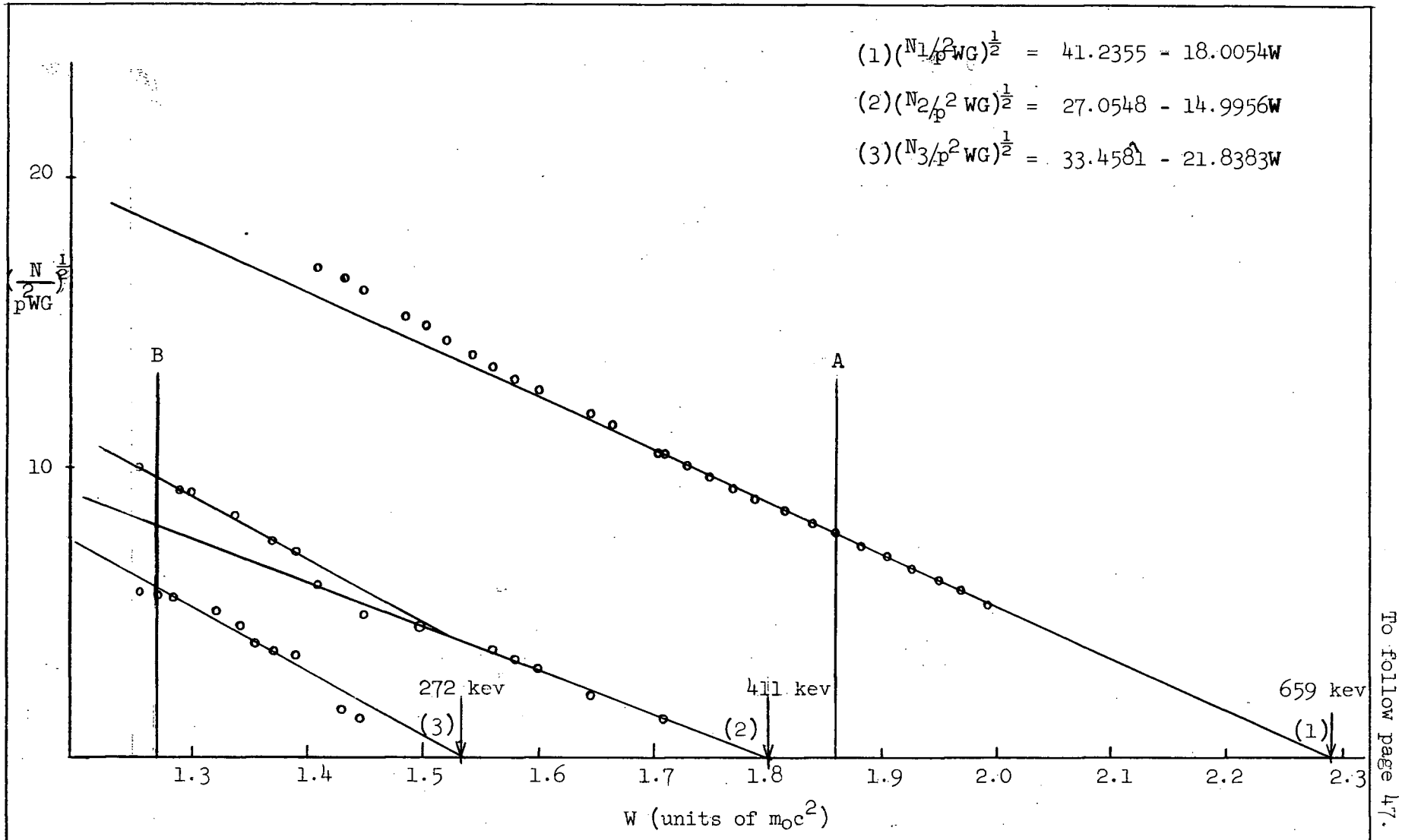

Fig.33 Kurie analysis of beta spectrum of Cs^{134}

To follow page 47.

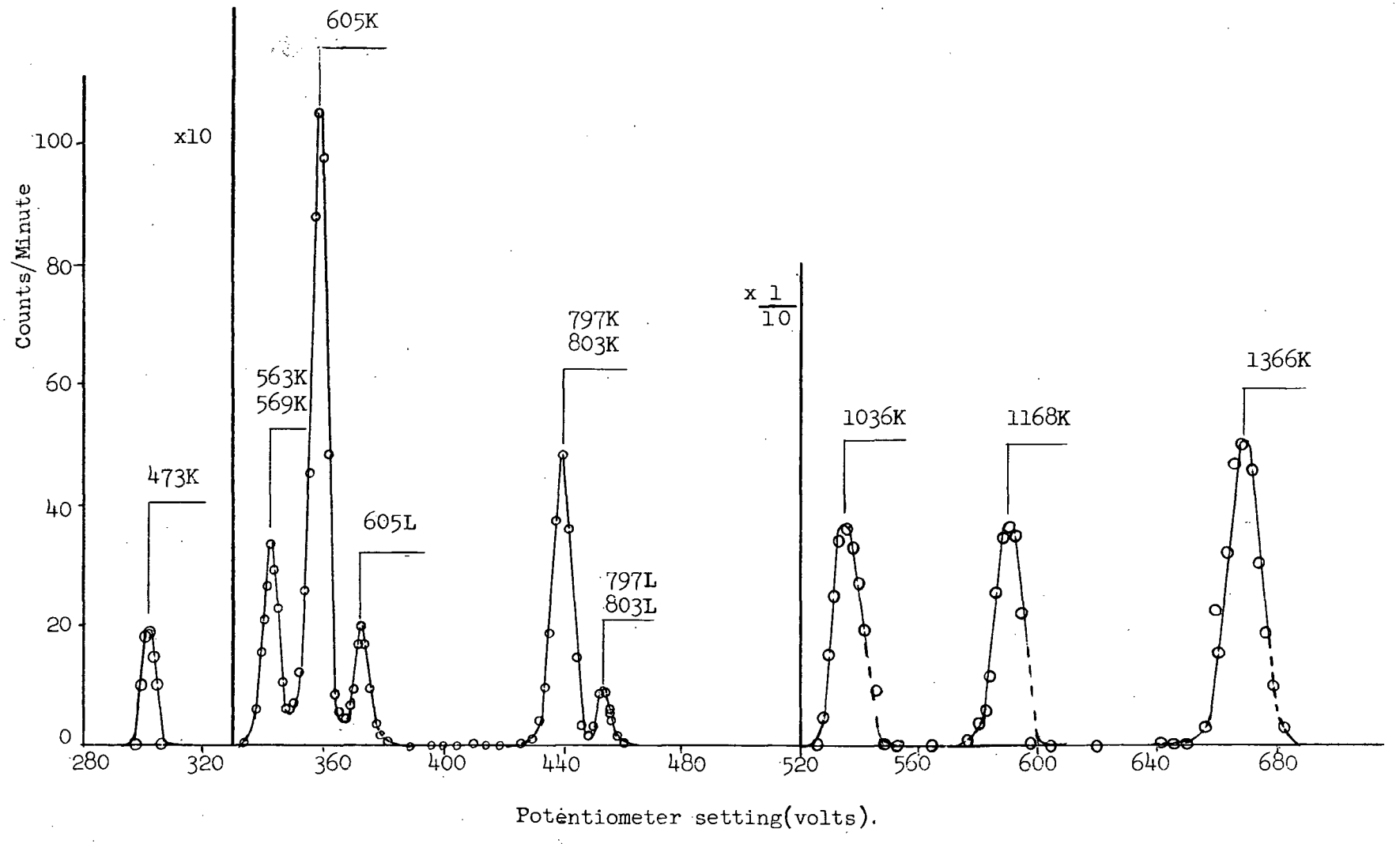

Fig. 34 Internal conversion spectrum of Cs^{134}
(Not all experimental points are plotted).

To follow page 47.

To follow page 47.

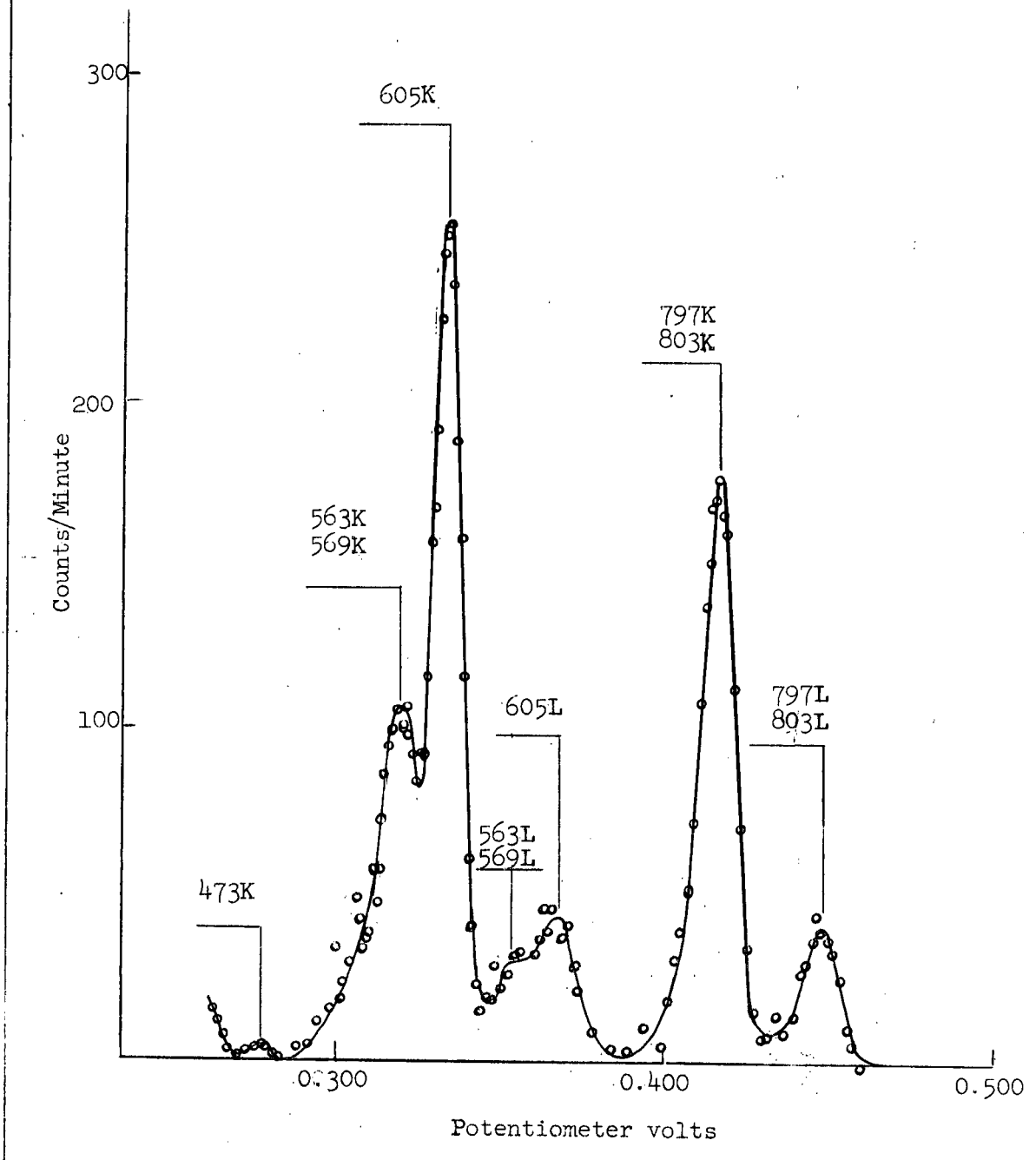

Fig.35 Part of photoelectron spectrum of Cs^{134}

Table III

Conversion Electron Intensities
(Beta scale)

E(kev)	K-conv.	(L+M) conv.
473	0.81 ± 0.30	
563	2.48 ± 0.60	
569	4.24 ± 0.60	
605	19.2 ± 1.0	3.5 ± 0.5
797 803	8.14 ± 0.4	1.3 ± 0.3
1036	0.08 ± 0.02	
1168	0.086 ± 0.02	
1366	0.016 ± 0.03	

variation of photoelectron cross-section with energy, using the data of Davisson and Evans[53], were also applied. The energy spread is small enough that such factors as the dependence of angle of emission of the photoelectrons on energy may be ignored. The data from this spectrum is included in Table IV.

Fig.36 shows the gamma-rays singles spectrum. It was analyzed by successive stripping of the upper energy profiles. For the three high energy gamma-rays, we used as shape standards the line profiles of the gamma-rays of Co^{60}, a source that was readily available. It has the advantage that its two gamma-rays of energy 1173 and 1333 kev are very close to two of the gamma-rays of Cs^{134}, but is suffers from the disadvantage that the line shapes are not resolved. To obtain these, the Co^{60} singles spectrum was taken with the same geometry as with Cs^{134}. This is shown in Fig.37. The 1333 kev photopeak is sufficiently resolved to measure its width. The peak profile is constructed as shown in the figure. When this peak is subtracted, the residue shows the clear leading edge of the 1173 kev photopeak. The correct half-width is selected (consistent with $\sqrt{E}$ dependence) and this establishes the Compton continuum of the 1333 kev gamma-ray under the 1173 kev photopeak. This is then scaled down to provide the 1173 Compton continuum. In this region of the spectrum, the sum of the two profiles is identical with the measured Co^{60} spectrum. The photopeak area ratios, when corrected for the known variation of peak/total ratio and crystal efficiency[54], gives the correct relative intensities of these two gamma-rays $\left[\frac{[1173]}{[1333]} = 0.96\right]$ to within 4%. They were then considered to be acceptable shape standards and were used to unfold the three upper energy profiles in Fig.36. The intensities of the expected Compton distributions of the combined 1036, 1168 and 1366 kev gamma-rays of Cs^{134} are not likely to exceed 1% of the 605 or 797 kev photo peaks so that even though their exact shapes are not known, their effect upon these intense photopeaks is minimal. Rather than ignore

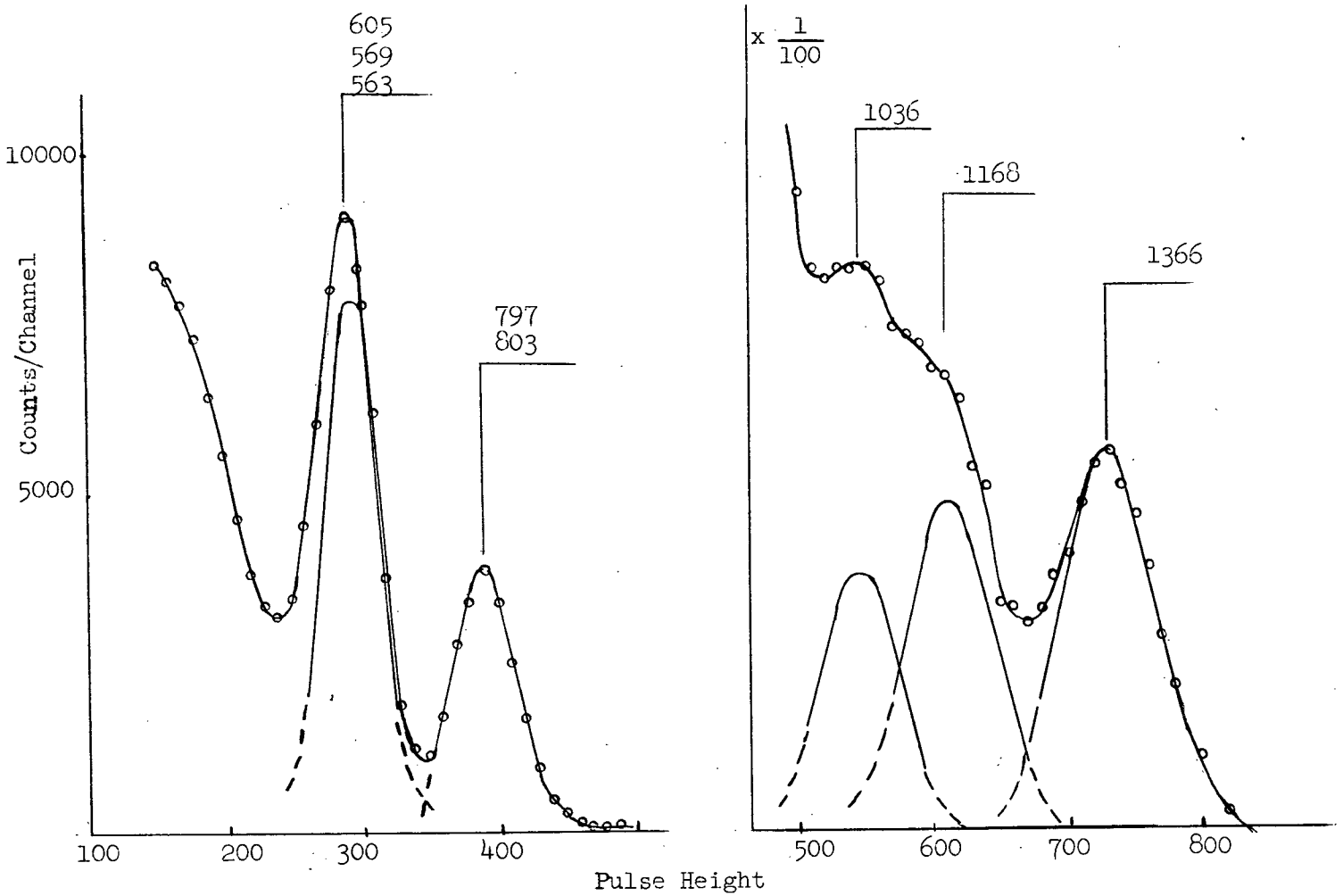

Fig.36 Scintillation spectrum of the gamma rays of C^{134}

To follow page 49

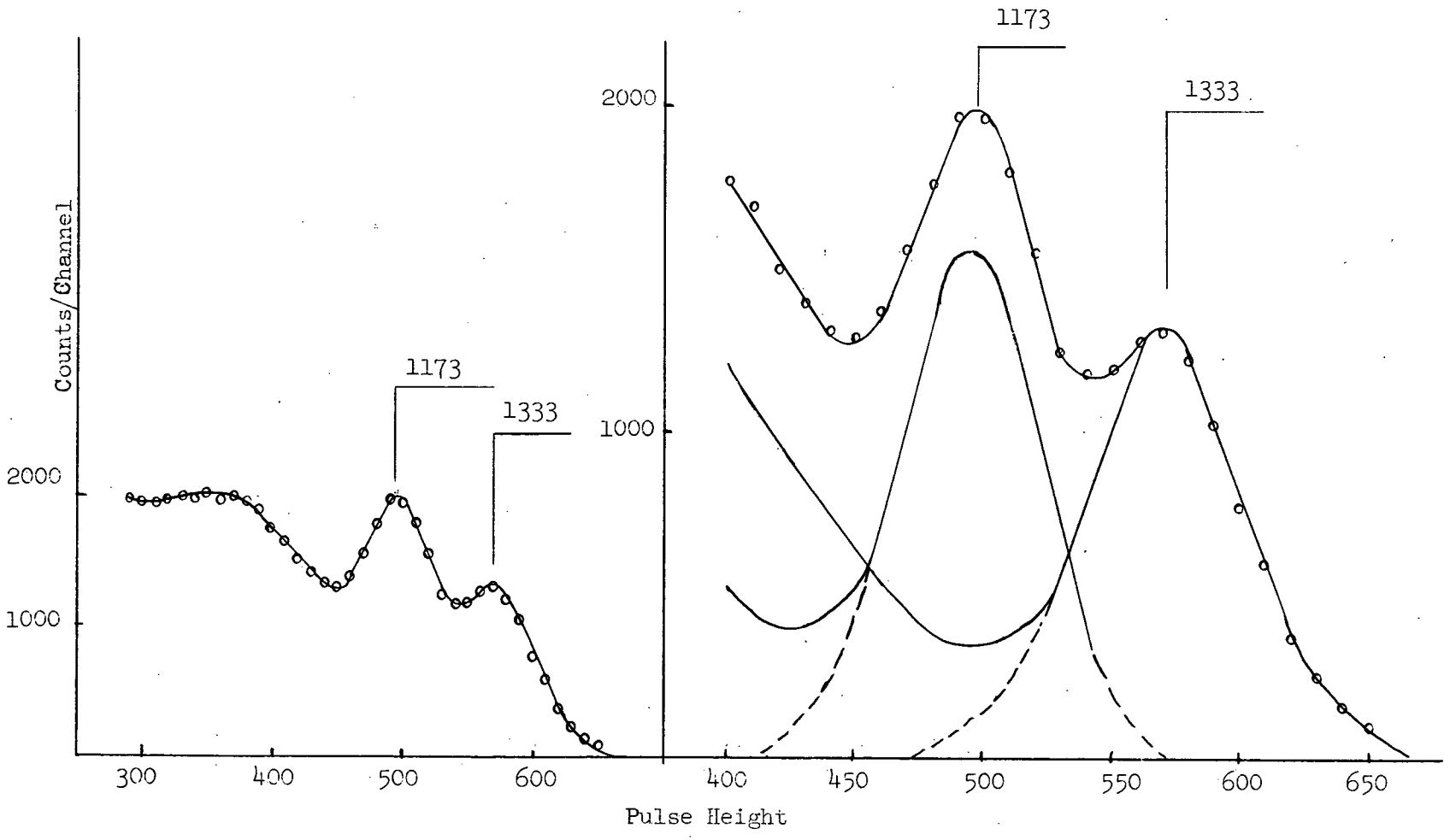

Fig.37 Gamma spectrum of Co^{60}

To follow page 49.

Table IV

Gamma-Ray Intensities

E (kev)	Relative Photoelectron Intensities	From singles	Relative Gamma-Ray Intensities
473	1.0 ± 0.5		1.0 ± 0.5
563 569	26.5 ± 6.5	126.5	26.5 ± 6.5
605	100		100
797 803		94 ± 5	94 ± 5
1036		1.5 ± 0.3	1.5 ± 0.3
1168		2.4 ± 0.3	2.4 ± 0.3
1366		3.6 ± 0.3	3.6 ± 0.3

it completely, however, the 605 and 797 kev residues were reduced by a constant 1% of the 605 kev photopeak.

The 661 kev line profile of Cs^{137} was used as a shape standard for the remainder of the spectrum, each profile being adjusted for photopeak width and peak/total ratio. We could not resolve accurately the weaker 563,569 kev composite peak from the stronger 605 kev peak and preferred to use the intensity ratio from the photoelectron data. A summary of all intensities is given in Table IV relative to the 605 kev gamma-ray.

Coincidence Results

We first used the gamma-beta system with the gamma-gate set on the 797,803 kev photopeak of the Cs^{134} singles spectrum. The spectrometer then scanned the beta-ray spectrum in coincidence with these gamma-rays. The Kurie analysis of the results is shown in Fig.38. The 662 kev group is present but there also seems to be contributions from lower energy groups, in complete disagreement with the decay scheme shown in Fig.25(a).

Fig.39 summarizes the results of measurements with the beta-gamma system. Fig.39(a) shows the gamma-rays in coincidence with the K-conversion electrons of the 797,803 transition. As expected, only the 605 kev photopeak appears, which probably includes the 563,569 gamma-rays as well. Fig.39(b) is the coincident gamma-ray spectrum when the spectrometer is set at the gate point A of Fig.33. If the decay scheme is correct, these should be in coincidence only with the 662 kev beta-group. Fig.39(c) shows the results when the gate-point is moved to B. This should include the 411 and 270 groups as well, both of which should be in coincidence with the 605 kev gamma-ray, but not with the 797, 803 kev radiation, and from the Kurie analysis, this difference should not be negligible. In fact, however, the distributions in Fig.39(b) and (c) have the same shape.

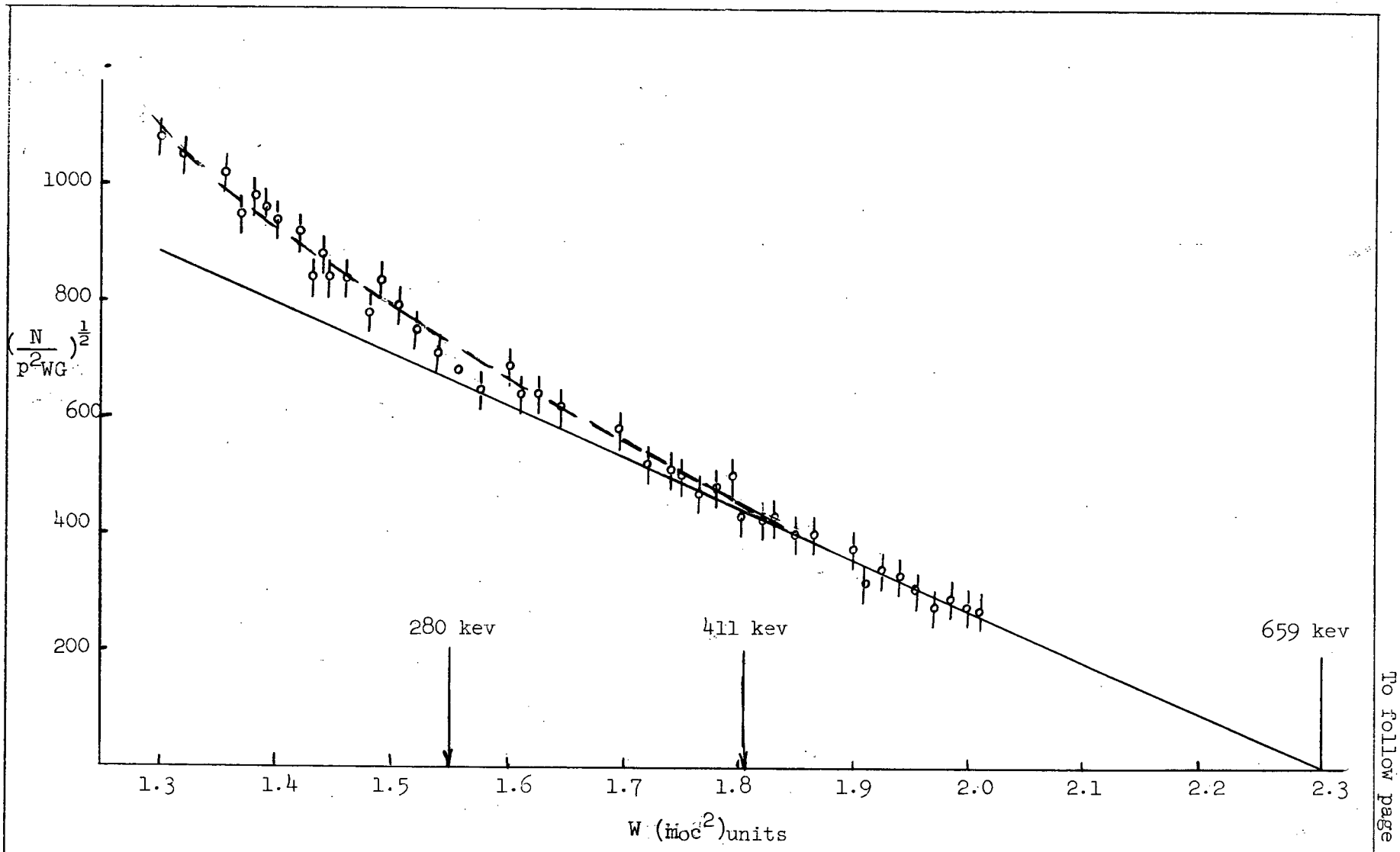

Fig.38 Kurie analysis of beta spectrum in coincidence with $\left.\begin{matrix}797\\803\end{matrix}\right\}$ gamma rays.

To follow page 51.

To follow page 51.

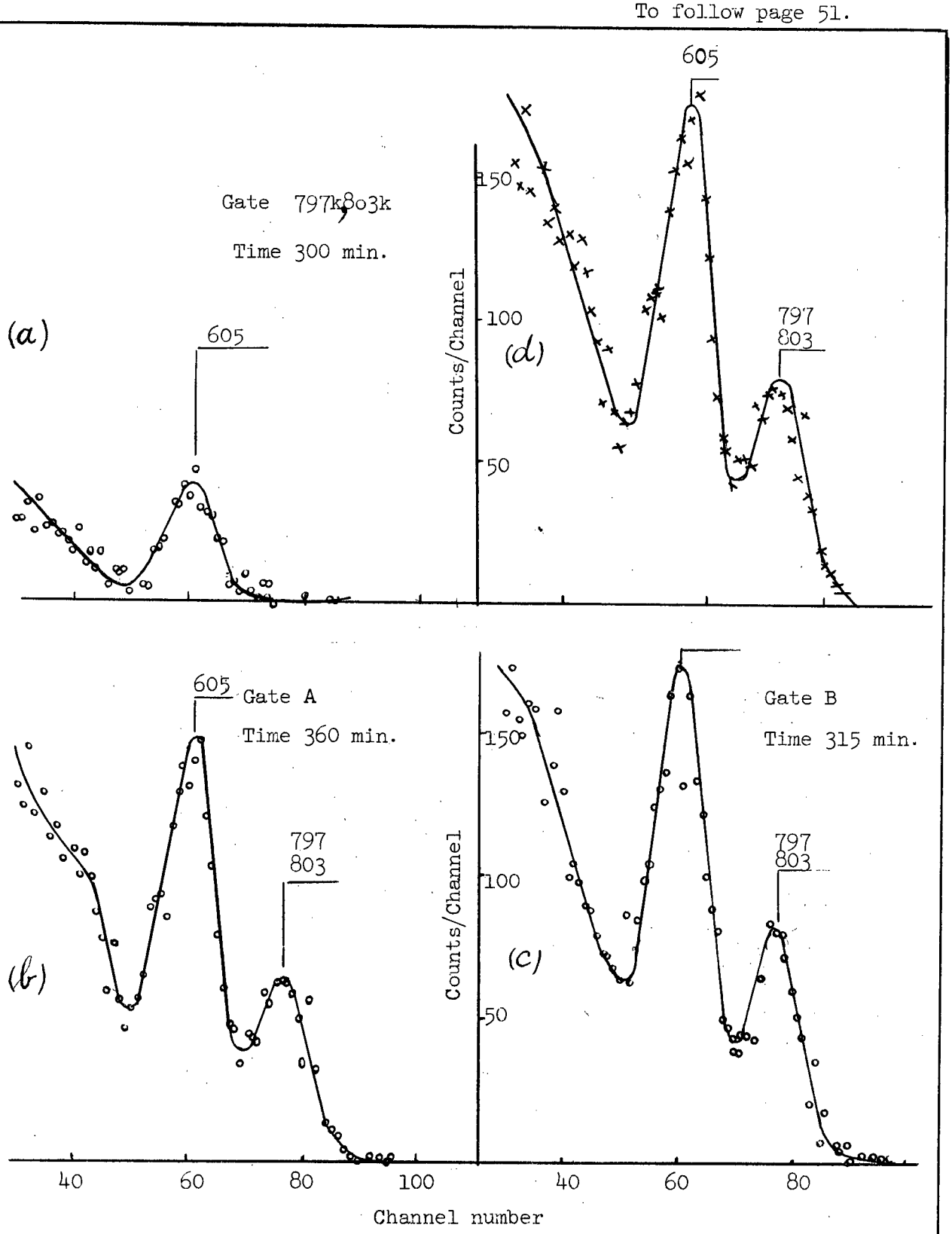

Fig.39 Scintillation spectra of gamma rays of Cs^{134} in coincidence with different gate points.

If we assume that our 411 and 270 kev beta-groups are actually back-scattered electrons of the 662 kev group, then the spectra at gate points A and B should be identical when corrected for time and the difference in counting rate at the two gates. In Fig.39(d), the solid curve is that of Fig.39(c). The superimposed crosses are the corrected experimental points of Fig.39(b). Within the experimental uncertainties, they are identical. We conclude then, that the 411 and 270 kev groups from our beta spectrum must be largely back-scattered electrons of the 662 kev group as predicted by Van Wigngaarden and Connor[52].

THE DECAY SCHEME

The transitions that we have been able to detect, fit the decay scheme of Fig.25(a) and in Tables III and IV we have the conversion and gamma intensities, each to a different scale. From previous work, it appears that all conversion coefficients are less than 10^{-2} so that for the purpose of estimating transition rates, the conversion intensities may be ignored. The relation between the two intensity scales may be deduced by referring to Fig.25(a) and examining the intensity balances of each level of Ba^{134}. All gamma-ray intensities will be denoted by [ ], and beta intensities by ( ). We will reduce all intensities to the gamma-scale, i.e., relative to the value of 100 for the 605 kev gamma-ray, and use mean values throughout.

The 605 kev level $\quad [797] + [563] + [1036] + [1366] = [605]$

$$94 - [803] + 26.5 - [569] + 1.5 + 3.6 = 100$$

$$\text{so that } [569] + [803] = 25.6 \qquad (a)$$

and similarly from the

1168 kev level $\quad [569] + [803] = 27.9 \qquad (b)$

In what follows, we will use the average value $[569] + [803] = 26.7$.

The 1402 level (659) + [569] = [797]

or (659) = 94 - [803] - [569] = 67.3

The 1641 level (411) = [473] + [1036] = 2.5

The 1971 level (89) = [569] + [803] + [1366] = 30.3

Beta-group Intensities

The percentage intensities of the beta groups from this analysis thus are 89(31%), 411(2%) and 659(67%), in excellent agreement with those reported by Van Wijngaarden and Connor[52] of 28%, 1% and 71%, who determined them by direct Kurie analysis of the beta-spectrum from a very thin source.

Conversion Coefficients and Transition Multipolarities

We can now reduce the conversion intensities to the gamma-scale. The 662 kev beta group has an intensity of 2730 counts on the beta scale and 67.3 on the gamma scale. The conversion multiplier is then 0.0247.

Table V lists the revised conversion intensities, the associated gamma-ray intensities and the calculated conversion coefficients. Also included are the theoretical values for some multipolarities computed from the tables of Sliv and Band[55]. With the error limits, all multipolarities are consistent with the spin-parity assignments of Fig.25(a).

It was not possible to resolve either the 563, 569 or the 797, 803 kev gamma-rays from the photoelectron spectrum. However, we can use the conversion data to make some estimates. If we compare the 797, 803 kev composite peaks and the 605 kev peak in both conversion and photoelectron spectra, we find that they have the same percentage width. It is particularly evident in the conversion spectrum, where both peaks are 'clean', and this is shown in Fig.40(a) where the 605 kev peak has been scaled up to the 797, 803 peak. In addition, the maximum of the latter corresponds exactly to a transition of energy 797 kev. Therefore the 803 kev component must be weak. From test

To follow page 53.

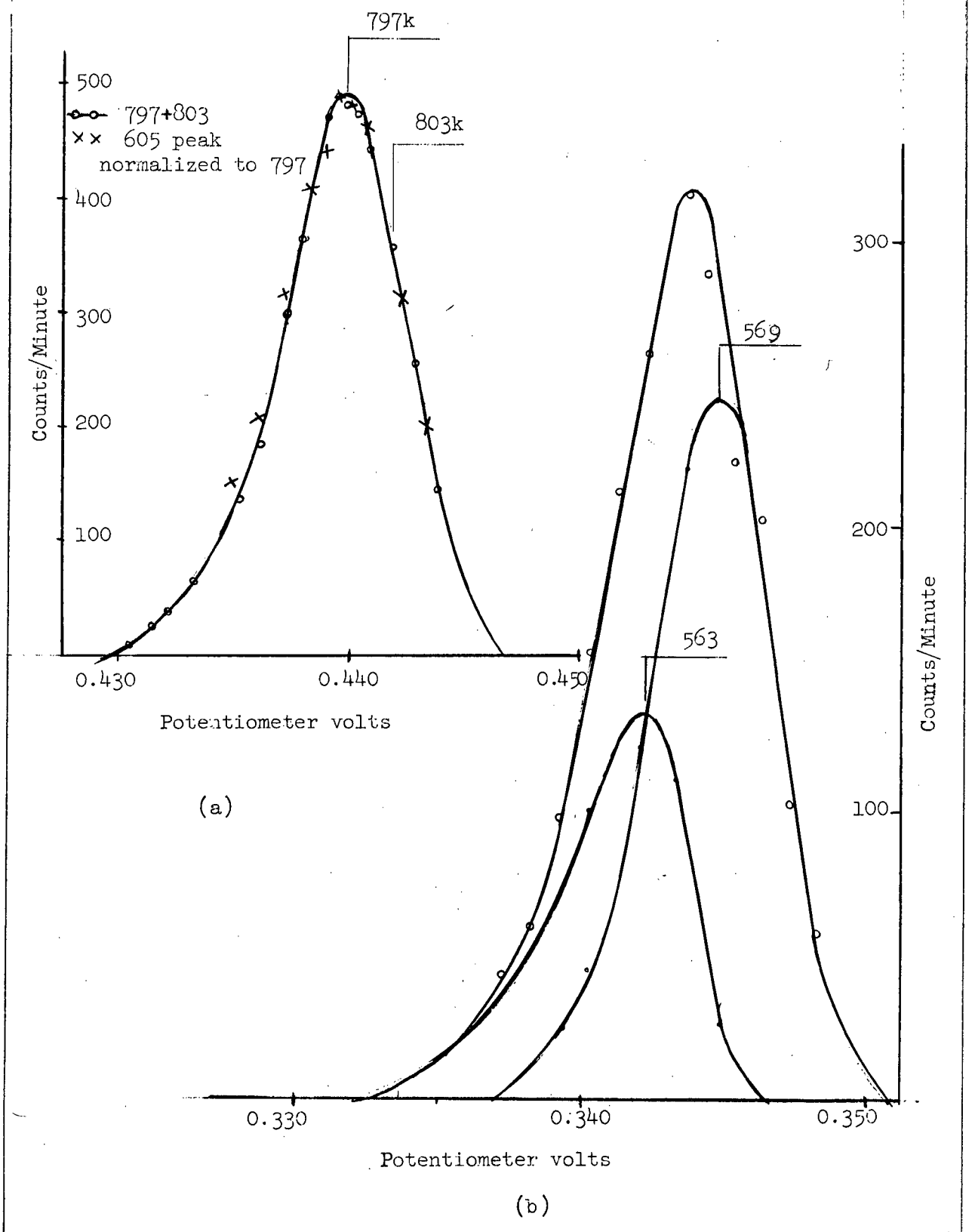

Fig.40 Analysis of composite conversion peaks

Table V

Transition Intensities and Conversion Coefficients

Energy	Gamma-Ray Intensity	K-conversion	K-conversion coeff.	Theoretical α_{1K}	Theoretical β_{1K}	Theoretical α_{2K}	Identification
473	1.0 ± 0.5	0.020 ± 0.006	$0.02 \pm {}^{0.032}_{0.011}$	0.00325	0.0130	0.0097	M1 or E2
563, 569	26.5 ± 6.5	{0.061, 0.105} ± 0.006	$0.0063 \pm {}^{0.0023}_{0.0015}$	0.00215	0.0084	0.0060	M1 or E2
605	100	0.474 ± 0.03	0.0047 ± 0.0003	0.00185	0.0071	0.0051	E2
797, 803	94 ± 5	0.20 ± 0.01	0.00213 ± 0.003	0.00104	0.0036	0.0026	E2
1036	1.5 ± 0.3	0.0020 ± 0.0004	0.00133±0.00067	0.00063	0.0020	0.00147	M1 or E2
1168	2.4 ± 0.3	0.0021 ± 0.0004	0.00088±0.00031	0.00051	0.00154	0.00115	E2
1366	3.6 ± 0.3	0.0026 ± 0.0005	0.00072±0.00022	0.00038	0.00108	0.00089	E2

profiles of composite peaks constructed from components of varying intensity ratios, we conclude that the 803 kev component cannot be much greater than about 10% of the 797 kev conversion line. From the established decay scheme, both should have the same multipolarity, so that this should be approximately the ratio of the gamma-ray intensities.

The 563, 569 composite peak in the conversion spectrum has a much greater percentage width than the 605 kev standard, and was easy to resolve into components of intensity ratio 0.58:1 as shown in Fig.40(b). Again, the decay scheme predicts the same multipolarity for these transitions (M1 predominantly) and this should be a measure of the gamma-ray ratio.

The only way we can check these conclusions is to check their consistency from the decay scheme intensity balances. If the [563] / [569] ratio is 0.58, then [569] = 16.8. Therefore, from the 1971 kev level in Ba^{134}, [803] = 9.9 which is roughly the intensity predicted from the conversion line profiles. Alternatively, from the 605 kev level, we get [797] = 85.2. Thus [797] + [803] = 95.1 compared with the measured value of 94.

These conclusions are in reasonably good agreement with the intensity estimates of other workers who were able to make them. Table VI shows the comparisons of our estimates of these four gamma-rays with some published results.

In summary, our results support the simplification of the decay scheme as proposed by Van Wijngaarden and Connor[52] and supported by Schriber and Hogg[51]. Other levels as shown in Fig.25(b) have been postulated for a variety of reasons not the least of which are observations of beta groups other than the three in Fig.25(a). The intensity measurements of Van Wijngaarden and Connor[52] have placed upper limits on the intensities of beta-groups of energies greater than 662 kev as $< 0.05\%$ which to all intents and purposes rules out the 683, 892 and 1453 kev groups. The only group they detect with

Table VI

Comparative Gamma-Ray Intensities
(Percentage of decay)

Author	[563]	[569]	[797]	[803]
Bashilov et at[36]	10	18	103	8
Forster & Wiggins[41]	14	12	72	11
Kiester et al[42]	9.4	12.8	91	18
Trehan et al[49]	9	11	93	
Schriber & Hogg[51]	9.5	12.6	83	12
Present work	9.5	16.4	83	9.7

an energy between 662 and 89 kev is the 411 kev group, and it has an intensity of approximately 1%. The 1770 kev level, supposedly fed by a 494 kev beta group de-excites by 960 and 1564 kev transitions. Van Wijngaarden and Connor[52] place an upper limit on the 1564 kev gamma-ray of $< 0.02\%$. We made a serious attempt to detect a 960 kev gamma-ray in the photoelectron spectrum but without success. It was reported by Segaert[50] and by Girgis[47] who quote intensities of 1.5% and 0.6% respectively. Counting times of approximately one hour on each point in this region of the spectrum produced no detectable peak. We were able to detect the 473 kev photopeak with relative ease and its intensity is 1% of the 605 kev gamma-ray. It is true that at 960 kev, the photoelectric cross-section falls to about one-quarter of its value at 473 kev but this should be more than compensated by the almost complete absence of Compton background, and by the much lower photomultiplier background we were able to use. The 1036, 1168 and 1366 kev photopeaks are clearly discernable as measureable peaks. A uranium radiator (50 mg/cm^2) increased the latter but still showed nothing at 960 kev. We conclude that if this transition exists, its intensity is less than 0.2%.

The log (ft) values of the three beta-groups closely parallel the results of other workers. They are 8.9 ± 0.5, $9.6 \pm {}^{0.10}_{0.20}$ and 6.2 ± 0.05 for the 662, 411 and 89 kev components respectively.

The spin-parity assignment to the 1641 kev level is somewhat uncertain. The log(ft) value for the 411 kev group from the 4+ Cs^{134} ground state to this level is 9.6 which looks like a first-forbidden transition although it is just possible that it is a heavily-retarded allowed decay. The conversion coefficients of both the 1036 and the 473 kev gamma-ray can be either M1, E2 or a mixture of both. The error limits on both transitions do not include other multipolarities such as E1, M2 or E3. If these identifications are correct, then the state is probably 3+ or 4+ . This agrees with the two possibilities resulting from the angular correlation studies of the 1036-605 gamma-ray cascade reported by Segaert et al[50]

It is not easy to fit the decay scheme of Fig.25(a) in all its details to a particular nuclear model. $_{56}Ba_{78}^{134}$ has 6 protons outside a closed shell and 4 neutron 'holes' so that the energy levels can hardly retain any single-particle characteristics. On the other hand, the nucleus does not fall into the strongly deformed group ($A > 150$ in this region of the periodic table) that have been treated with some success by the various collective model approaches (see Appendix I). In their paper, Segaert et al[50] have calculated the level structure to be expected on the basis of seven different models developed for the medium weight nuclei, and the asymmetric rotor model of Mallmann[62] appears to give the closest fit. All of the levels of Fig.25(a) appear with the correct spins and parities including the 1641 kev level which is degenerate with spins 3+ and 4+. In addition however, it predicts levels at about 1570 and 1770 kev which do not appear to be excited in this decay. All seven models predict the first 2+ state (605 kev) and most of them the second 2+ state (1168 kev). It is interesting to note that the ground, 605 and 1971 kev states fit almost exactly the predicted sequence of rotational band components for K=0.

It is also of interest to compare Fig.25(a) with the level structure of $_{54}Xe_{78}^{132}$ (2 paired protons less). These are shown for the first few levels in Fig.41. The similarities are quite marked, although for Xe^{132} there are two less protons which can interact with the core. It is tempting to conclude from this that the many-particle shell model with configurational mixing is a better approximation in this case than one which emphasizes core excitations. Kurath[63] points out that the region of the $1g_{9/2}$ shell is one in which the many-particle model should work reasonably well. The six extra-core protons of Ba^{134} have $1g_{7/2}$ states immediately available which

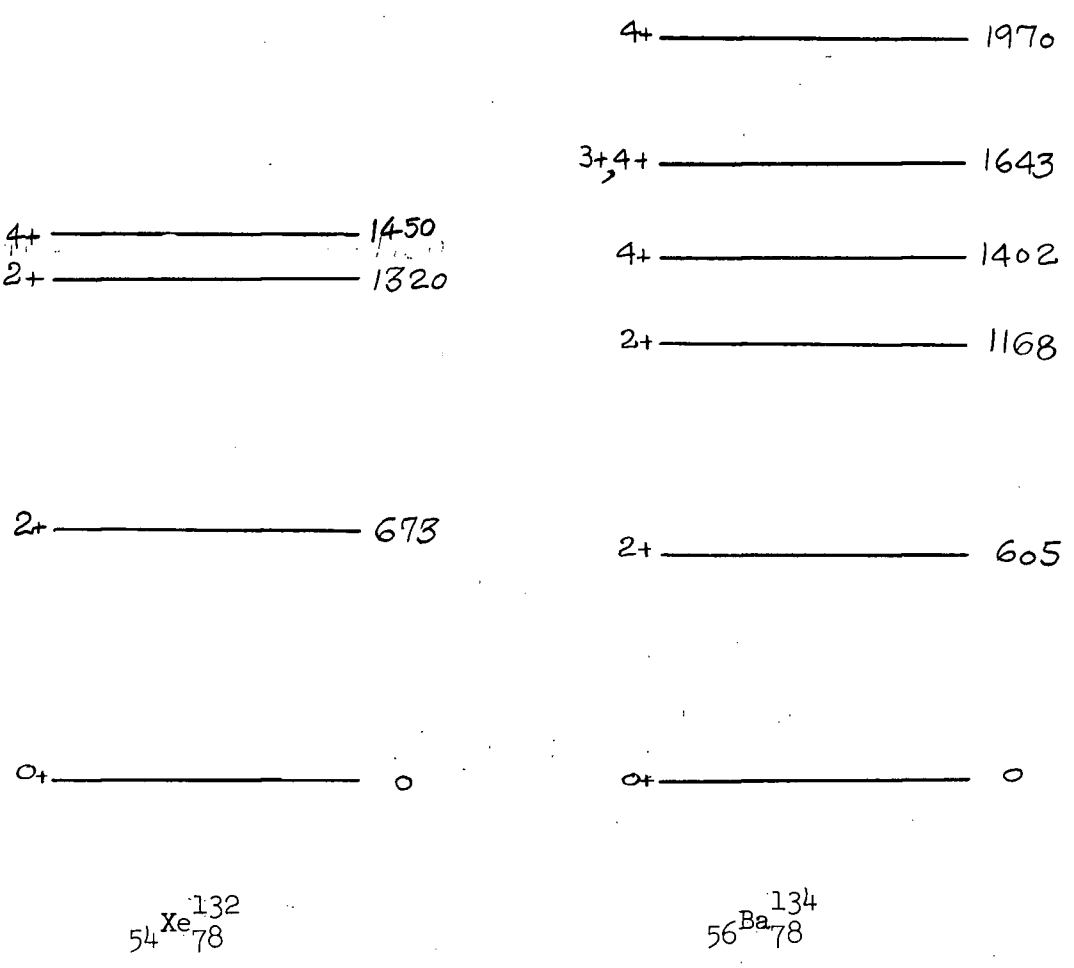

Fig.41 Level structure of Xe^{132} and Ba^{134} (comparison).

lie above the $1g_{9/2}$ configurations. It is fruitless however, to speculate on one model to the exclusion of others since it is probable that both types of excitation contribute.

Appendix 1

NUCLEAR MODELS

Attempts have been made from time to time to arrive at a model of the nucleus consistent with the available experimental evidence. Several models have been proposed each of which explains some aspects of the experimental data in a more or less limited way. Among the models which have been proposed are the Fermi gas model, the liquid drop model, the alpha particle model, the shell (independent particle) model and the collective model. For beta and gamma ray spectroscopy the last two have proved really useful and hence will be described briefly.

The Shell Model

It is now well established that electronic energy levels in an atom show a distinct shell structure which accounts for its characteristic behaviour. For instance, atoms such as helium, neon, krypton etc. are exceptionally stable because they have all their electronic shells completely filled. Among nuclei, those containing 2, 8, 20, 50, 82 and 126 protons or neutrons are observed to be more stable[56] than others. These numbers are known as 'magic numbers'. The nuclear shell model originated as an attempt to explain the magic numbers on lines similar to those of atomic shell structure.

The basic assumptions of the shell model after Mayer, Haxel, Jensen and Suess are[57]:

1) a nucleon moves independently in a nuclear potential field created by all the others. This potential consists of two parts and is analytically expressed as

$$V(r) + f(r)\,\vec{l}\cdot\vec{s} \qquad 1$$

where V(r) is the average central potential due to (A-1) nucleons and f(r) $\vec{l}.\vec{s}$ is that resulting from a strong interaction between the orbital and spin angular momentum of a nucleon.

2) The effect of the latter is to split each l level into two levels with $j = l+\frac{1}{2}$ and $j = l-\frac{1}{2}$, the $j = l+\frac{1}{2}$ level lying below $j = l-\frac{1}{2}$.

For V(r) the most commonly used form is one intermediate between the square well potential and the oscillator potential and is shown in Fig.(A1). The exact form of f(r) is not yet known.

When these assumptions are incorporated into the wave mechanical treatment, the result is that protons and neutrons form independent shells, or subshells, which close at the magic numbers as shown in Fig.(A1).

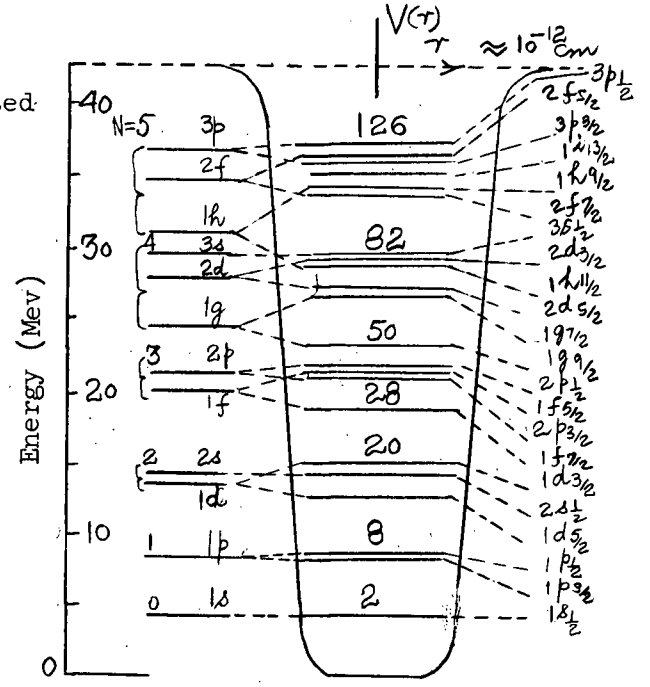

Fig.A1 Energy levels in a potential well intermediate between square well and an oscillator potential.

In addition to explaining the magic numbers, the shell model gives a complete description of ground state spins and parities, nuclear isomerism and some information about magnetic dipole and electric quadripole moments.

To deduce <u>angular momenta</u>, we start with nuclides consisting entirely of closed shells (N and Z, both magic) and those consisting of closed shells plus or minus one particle. According to the exclusion principle the former must have zero angular momentum and the total angular momentum of the latter is just the angular momentum of the 'extra' or the 'missing' (hole) particle. Thus the angular momenta of $^{8}_{8}O^{16}$, $^{20}_{20}Ca^{40}$, $^{126}_{82}Pb^{208}$ are zero and those of $^{8}_{7}N^{15}$, $^{9}_{8}O^{17}$, $^{20}_{19}Kr^{39}$, $^{125}_{82}Pb^{207}$ and $^{126}_{83}Bi^{209}$ are $\frac{1}{2}$, $\frac{5}{2}$, $\frac{3}{2}$, $\frac{1}{2}$ and $\frac{9}{2}$ respectively in accordance

with experimental evidence.

For odd-A nuclides, the assumption made is that like nucleons in a nucleus pair off in such a way that their angular momenta cancel. Then the angular momentum of an odd-A nuclide is due entirely to the angular momentum of the last unpaired nucleon. Actually this assumption is insufficient unless due account is taken of the fact that nucleons outside the closed shells interact with each other. As a result of this so-called pairing energy effect, a level will be depressed when it contains an even number of nucleons compared with its value when it contains an odd number of nucleons. Moreover, the effect increases with increasing orbital angular momentum. Thus odd A nuclides with N above 58 will be expected to have angular momenta of 7/2 or 11/2. Instead they have angular momentum of $\frac{1}{2}$, showing that 1 $g_{7/2}$ and 1 $h_{11/2}$ levels are depressed below the $3s_{\frac{1}{2}}$ level when they are filled by even number of nucleons.

The assumption that like nucleons outside closed shells pair off to produce zero angular momentum is not really self evident. However, it has failed only in three cases. They are $^{12}_{11}Na^{23}$ with angular momentum 3/2 instead of 5/2, $^{30}_{25}Mn^{55}$ with 5/2 instead of 7/2 and $^{45}_{34}Se^{79}$ with 7/2 instead of 9/2. In these three nuclides the total angular momentum is then due to the three nucleons outside the closed shell.

For odd-odd nuclides, the total angular momentum must be due to at least two unpaired particles, the last proton and the last neutron. In this case there is no simple rule to deduce the angular momentum of the nuclide because the angular momenta of the two unpaired particles can combine in many ways.

By convention, nucleons have an even intrinsic parity. The parity of a nucleon state is given by $(-1)^{\ell}$. The shell model predicts the orbital angular momentum for each nucleon and hence the parity of each nucleon in different nucleon states is known. The parity of the nucleus, then, is the product of the parities of the individual nucleons.

The single particle shell model is very successful in predicting spins and parities of the ground states of odd-A nuclei, and even some of the low-lying states of excitation. Higher excited states lose their single particle character, probably because some nucleons are excited out of the core to join the odd particle.

Goldhaber, Hill, Sunyar[58] have studied nuclear isomerism in terms of the shell model. Isomerism (i.e. the phenomenon of long-lived excited states) occurs when transitions to neighbouring nuclear states become forbidden because of large changes in angular momentum involved. The shell model predicts that the conditions for isomerism should exist below magic numbers 50, 82 and 126, but not immediately above them. This is what is observed when the known long lived isomers ($T_{\frac{1}{2}} \geqslant 1$ sec) with odd A are plotted against their odd Z or odd N number. Such a plot reveals the presence of groupings or 'islands of isomers' just below the magic numbers 50, 82 and 126.

Magnetic moments (μ) are obtained using ground state angular momenta. For even even nuclides, J=o and hence μ=o . For odd A nuclides, J=j and magnetic moments are calculated using the following relations:

$$\begin{aligned} \mu &= (j-\tfrac{1}{2})g_\ell + g_s \qquad \text{for } \ell = j-\tfrac{1}{2} \\ \mu &= \frac{j}{j+1}\left[(j+\tfrac{3}{2})g_\ell + g_s\right] \text{ for } \ell = j+\tfrac{1}{2} \end{aligned} \qquad (3)$$

where g_ℓ = 1 for a proton and zero for a neutron; g_s = 2.79 for a proton and -1.19 for a neutron.

μ-values calculated using the above relations are known as Schmidt values and are compared with the observed magnetic moments. Qualitatively they agree very well but quantitatively they show deviations, and usually lie somewhere between the two limits. These deviations disappear (partly) if mixing in of states other than the single particle states is also taken into account. There is some evidence[59] that the magnetic moment μ of a free nucleon is not the same as when the nucleon is in a bound state.

Shell model predictions regarding electric quadrupole moments (Q) are:

Q = o for magic number nuclei

Q is -ve for nuclei with a proton or a neutron outside a closed shell and Q is +ve for nuclei with a 'hole'.

No exceptions have been found to these predictions.

Regarding the magnitudes of Q's the situation is very discouraging. Theoretically Q should be of the order of the nuclear radius squared i.e. $10^{-25} cm^2$. This is found to be so for small A, but for A $>$ 100, values as large as 10×10^{-25} occur. Another puzzling feature is that Q's for odd A-odd N nuclides are of the same order as those of odd A-odd Z nuclides whereas the shell model predicts the former to be much smaller.

The magnitude of Q is a measure of the deviation of a nucleus from spherical shape, and the shell model seems to underestimate this deviation. The large values of Q mean that the nucleus is far from spherical in shape. When, instead, a spheroidal nucleus is treated mathematically, the Q's turn out to be closer to the observed values. This modification of the shell model leads to the collective model[60].

The Collective Model

In the shell model, it is assumed that nuclear properties such as angular momenta, magnetic moments and electric quadrupole moments are determined by the last nucleon moving outside the nuclear core. The nuclear core does not play any active role. The collective model, however, assumes that nucleons outside the core exert a centrifugal pressure on the surface of the core. As a result the core may undergo surface oscillations and become deformed into a non-spherical shape. The nucleons thus move in a non-spherical potential. The nuclear deformation reacts on the nucleons and modifies somewhat the independent particle aspect.

The total angular momentum remains the same but now it is shared between the core and the last nucleon outside it. The core makes a contribution $\sim \frac{Z}{A} L_{core}$ towards the magnetic moment. This brings magnetic moments in better agreement with the observed values.

The effect on the quadrupole moment is much larger. A small deformation of the core can lead to large quadrupole moments. Since the quadrupole moments are due to core deformations, odd A-oddN nuclides may show the same order of quadrupole moments as those of odd A-oddZ nuclides.

The deformation of the core is specified by parameter β such that

$$\beta = \frac{\Delta R_o}{R_o} \sim \frac{n}{A} \qquad (4)$$

where R_o is the average nuclear radius and ΔR_o is the difference between the major and minor semi-axis of the ellipse, n is the number of nucleons outside the core.

Variations of the potential energy of the nucleus with respect to β reveals that

1) for small n, the equilibrium shape of the nucleus is spherical and collective motion is a vibration about this shape.

2) for large n, the nucleus is permanently deformed and the collective motion is a rotation of the nuclear orientation.

Under these circumstances the collective angular momentum $\bar{R}$ is given by

$$|\bar{R}|^2 = \left[J(J+1)-K^2\right]\hbar^2 \qquad (5)$$

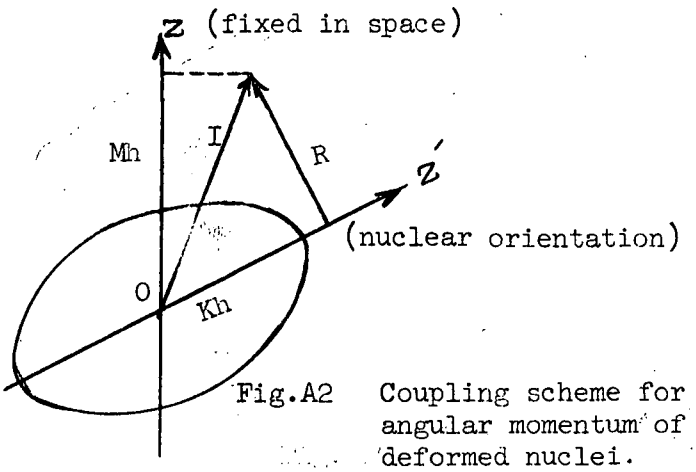

Fig.A2 Coupling scheme for angular momentum of deformed nuclei.

where I is the resultant angular momentum of the nucleus and K is the sum of the intrinsic angular momenta due to all nucleons outside the core (Fig.A2).

For the sake of simplicity it may be assumed now that level spectrum arises from:

a) intrinsic nucleonic motion in a spheroidal potential of which shell model predictions are a special case

b) collective rotation

c) collective vibration

a) Intrinsic spectrum for a spheroidal field as a function of β has been calculated by Nillson[61]. A specimen of his results are shown in Fig. A3.

It is seen that each shell model state splits up into $\frac{1}{2}(2j+1)$ states. For $\beta = o$, the normal shell ordering appears. For large β, however, there is a drastic change.

b) For rotational state

$$E_{rot} = \frac{1}{2} I\omega^2 \qquad (6)$$

where ω is the angular velocity of the core and I is the effective moment of inertia of the core. I is given by

$$I = \frac{2}{5} MA(\Delta R_o)^2$$

Combining (5) and (6)

$$E = \frac{\hbar^2}{2I}\left[J(J+1)-K^2\right] \qquad (7)$$

Equation (7) determines the rotational band superimposed on the intrinsic levels.

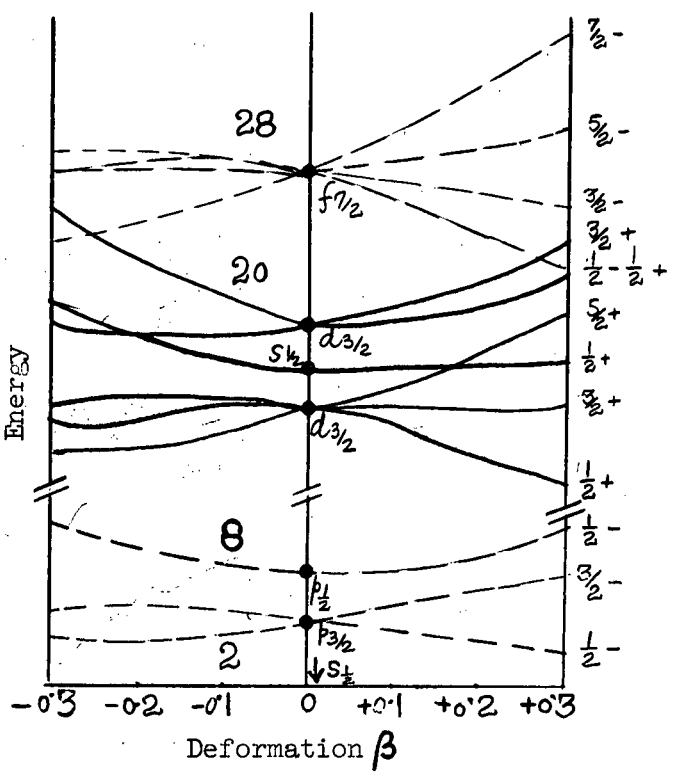

Fig.A3 Single particle states in a spheroidal potential as a function of β.

For even even nuclei K = o and as in the case of a homonuclear diatomic moelcule, the levels are given by

J=o, 2, 4, 6, ... (parity even) .

For odd A nuclei K is equal to the angular momentum of the last odd particle as determined from Nilsson orbits and the allowed values of J are

J = K, K+1, K+2, ... (half integral) .

Parity is determined by K and hence is the same for all states of the rotational band.

c) In this case the nucleus possesses a certain number of vibrational quanta (phonons) each of energy $\hbar\omega$, and angular momentum $l\hbar$. In the simple case of even even nuclei, the vibrational spectrum is due to quadrupole phonons and is shown in Fig.A4.

Collective model thus predicts fine structure of nuclear levels. It retains all the characteristics of the shell model and at the same time gives better results for magnetic moments, electric quadrupole moments, excited states of nuclei and other phenomenon.

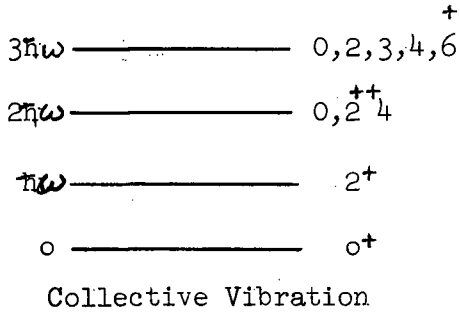

Fig.A4 Vibrational levels in even-even nuclei.

Appendix 2

SOME CIRCUIT DIAGRAMS

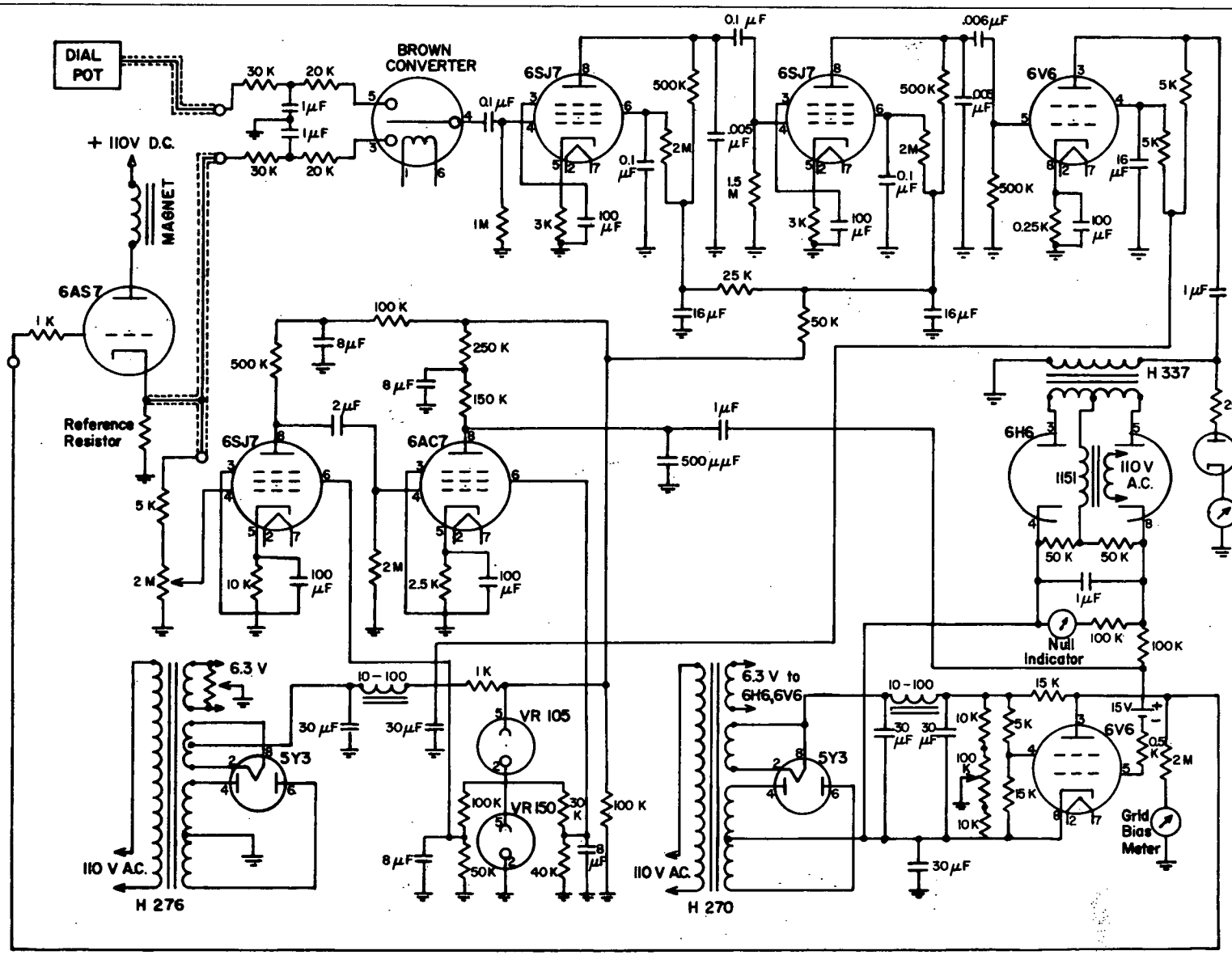

Fig. A5 Magnet current control circuit

To follow page 68.

To follow page68.

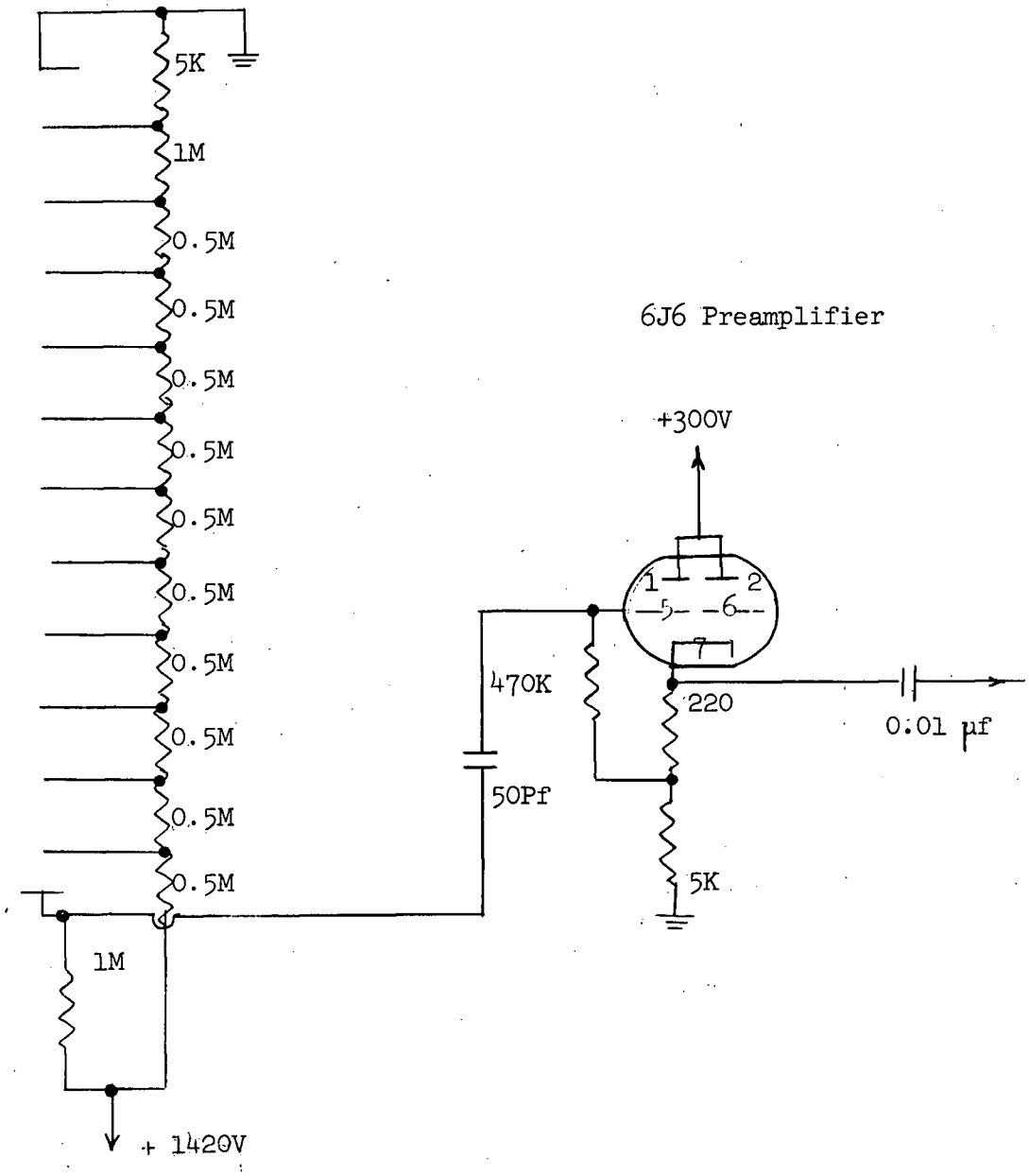

Fig.A6 Components of the phototube bleeder.

To follow page 68.

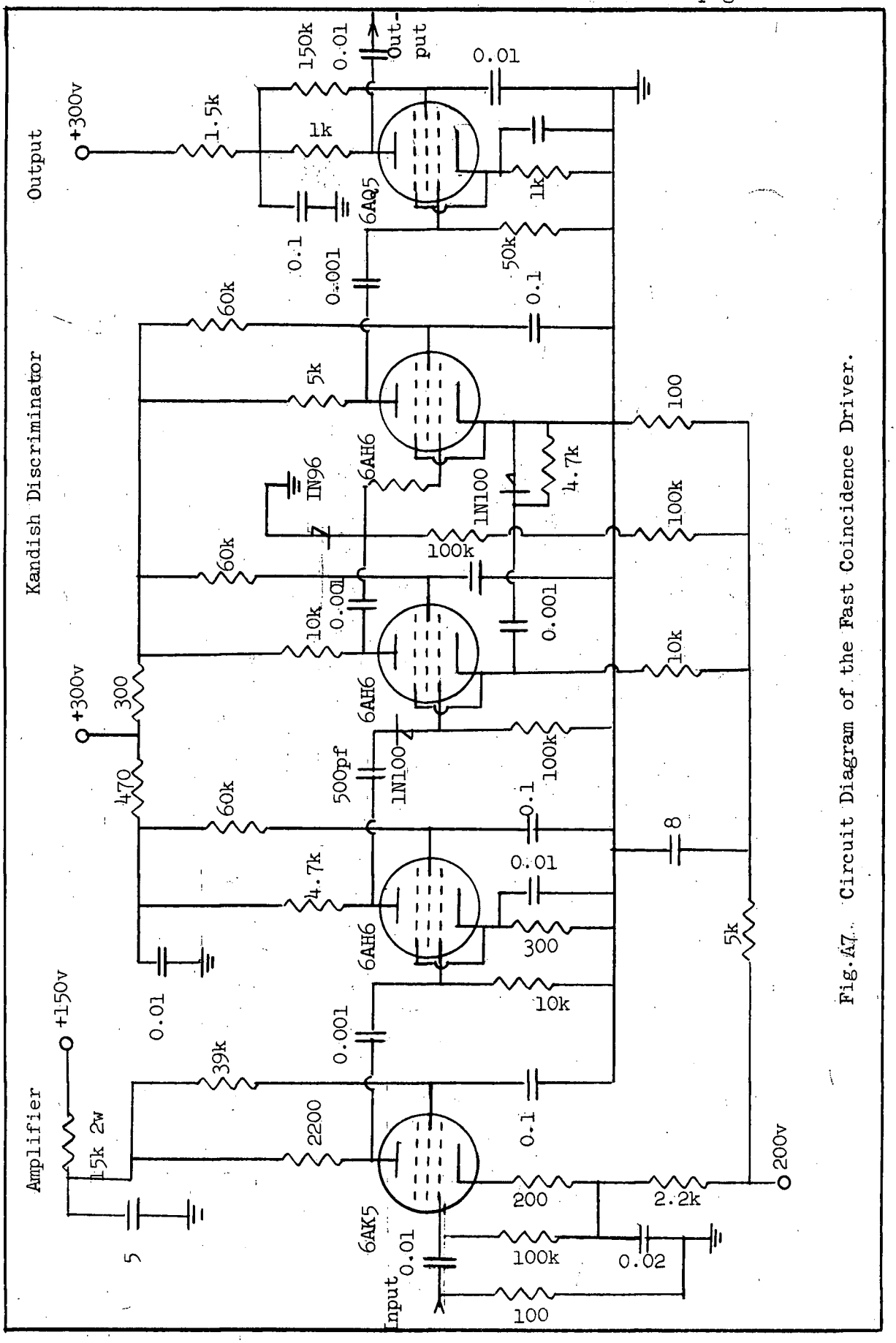

Fig.47. Circuit Diagram of the Fast Coincidence Driver.

To follow page 68.

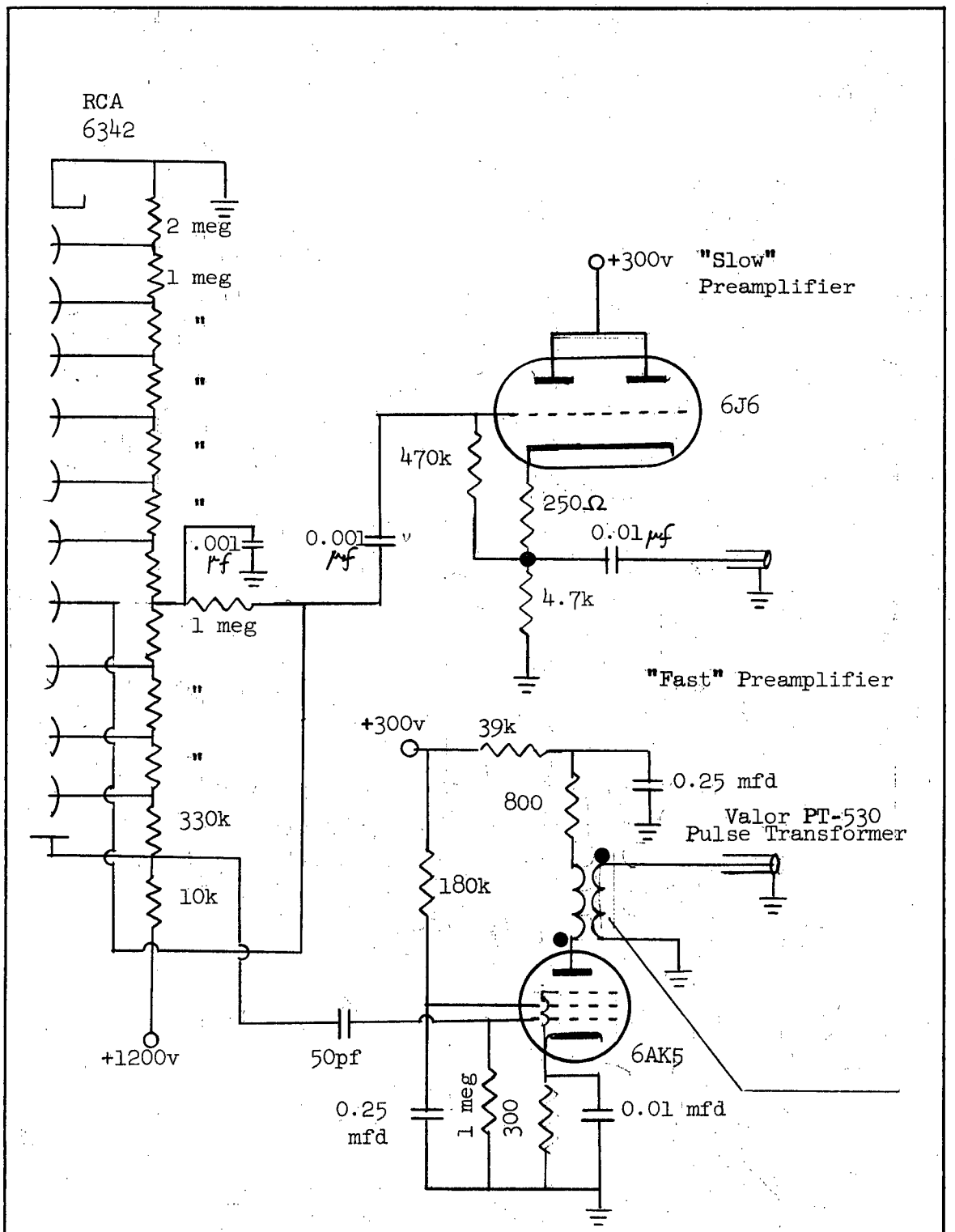

7A8 Scintillation Detector Electronics

BIBLIOGRAPHY

1. E. Fermi. Zeits. f. Physik 88, 161 (1934).
2. C.L. Cowan et al. Science 124, 103 (1956).
3. E. Majorana. Nuovo Cimento 14, 171 (1937).
4. P.A.M. Dirac. Proc. Roy. Soc. (London) A 117, 610 (1928); A 118, 351 (1928).
5. C.N. Yang and T.D. Lee. Phys. Rev. 104, 254 (1956).
6. C.S. Wu et al. Phys.Rev. 105, 1413 (1957).
7. Frauenfeldes et al. Phys. Rev. 106, 386 (1957).
8. Hermannsfeld Burn et al. Phys. Rev. Letters 1, 61 (1958).
9. Fermi Lecture Notes. University of Chicago Press 76, (1950).
10. Appendix II "Beta and Gamma Ray Spectroscopy" edited by K. Siegbahn.
11. E. Feenberg and G. Trigg. Rev. Mod. Phys. 22, 399 (1950).
12. S.A. Moszkowski. Phys. Rev. 82, 35 (1951).
13. S.A. Moszkowski. Chapter VIII, "Beta and Gamma Ray Spectroscopy" edited by K. Siegbahn.
14. M.E. Rose. "Internal Conversion Coefficients" North Holland Publishing Company.
15. E.L. Stolyarova. Uspenski. vol.6, no.6, 872 (1964).
16. A.H. Wapstra et al. "Nuclear Spectroscopy Tables", North Holland Publishing Co., Amsterdam, 31 (1959).
17. K. Siegbahn. Phil. Mag. (7), 37, 162 (1946).
18. T.R. Gerholm. Handbuch der Physik, 33, 610.
19. "Beta and Gamma Ray Spectroscopy". 227 (1955).
20. Solve, Hultberg. Arkiv for Fysik Band 15nr 27, 307 (1963).
21. R.E. Bell, R.L. Graham and H.E. Petch. Can. J. Phys. 30, 35 (1952).
22. L.E. Biedenharn and M.E. Rose. Rev. Mod. Phys. 25, 746 (1953).
23. H. Busch. Ann. Physik 81, 974 (1926). Arch. Elektrot. 18, 583 (1927).
24. M. Deutsch, L.G. Elliot and R.D. Evans. Rev. Sci. Inst. 15, 178 (1944).
25. Hornyak, Lauritsen and Rasmussen. Phys. Rev. 76, 731 (1949).

26. J.M. Keller, E. Koenigsberg and A. Paskin. Rev. Sci. Inst. 21, 713 (1950).

27. W.W. Pratt, E.I. Boley and R.T. Nicholas. Rev. Sce. Inst. 22, 92 (1951).

28. Jensen, Laslett and Pratt. Phys. Rev. 75, 458 (1949).

29. K.C. Mann and F.A. Payne. Rev. Sci. Inst. 30, 408 (1959).

30. R.P. chaturvedi. Ph.D. Thesis, U.B.C. Van., 8 (1962) unpublished.

31. L.G. Elliot and R.E. Bell. Phys. Rev. 72, 979 (1947).

32. J.L. Meem and F. Maienshein. Phys. Rev. 76, 328 (1949).

33. M.A. Waggoner et al. Phys. Rev. 80, 420 (1950).

34. K. Gromov and B. Dzhelepov. Dokl. Akad. Nauk. SSSR 85, 299 (1952).

35. J.M. Cork et al. Phys. Rev. 90, 444 (1953).

36. A.A. Bashilov et al. Izv. Akad. Nauk. SSSR Ser. Fiz 18, 43 (1954).

37. D.C. Lu and M. Wiedenbeck. Phys. Rev. 94, 501 (1954).

38. M.C. Joshi and B.V. Thosar. Phys. Rev. 96, 1022 (1954).

39. T. Azuma. Bull Maniwa University 3A, 237 (1955).

40. G. Bertolini et al. Nuovo Cimento 2, 273 (1955).

41. H.H. Forster and J.S. Wiggins. Nuovo Cimento 2, 854 (1955).

42. G.L. Keister et al. Phys. Rev. 97, 451 (1955).

43. E. Klema. Phys. Rev. 100, 66 (1950).

44. G. Chandra. Proc. Indian Acad. Science. A vol. 44, no.4, pp.194-200, (Oct., 1956).

45. C.L. Peacock. NP-6325 Microcard (1957).

46. T.D. French and M. Goodrich. Bull. Am. Phys. Soc. 4, 391 (1959).

47. R.K. Girgis and R. Van Lieshout. Nuclear Physics 12, 672 (1959).

48. Y. Yamamoto. Thesis, Osaka University, Japan (1960).

49. P.N. Trehan et al. Phys. Rev. 131, 2625 (1963).

50. O.J. Segaert et al. Nuclear Physics 43, 76 (1963).

51. S.O. Schriber and B.G. Hogg. Nuclear Physics 48, 647 (1963).

52. W. Van Wijngaarden and R.D. Connor. Can. J. Phys. 42, 504 (1964).

53. G.M. Davisson and R.D. Evans. Rev. Mod. Phys. 24, 79 (1952).

54. W.E. Mott and R.B. Sutton. Encyclopedia of Physics 45, 111 (1958).

55. L.A. Sliv and I.M. Band. "Coefficients of Internal Conversion of Gamma Radiation". Unpublished.

56. (a) M.G. Mayer. Phys. Rev. 74, 253 (1948).
(b) B.H. Flowers. Prog. in Nuc. Phy. 2, 235 (1952), edited by O.R. Frisch, Academic Press.
(c) M.H.L. Pryce. Rep. Prog. Phy., London Physical Society 17, 1 (1954).

57. (a) M.G. Mayer. Phys. Rev. 78, 16 (1950).
(b) O. Haxel et al. Phys. Rev. 75, 1766 (1949).

58. (a) M. Goldhaber. Rev. Mod. Phys. 24, 179 (1952); Phys. Rev. 83, 906 (1951).

59. De Shalit. Proc. of Int. Conf. of Nuc. Structure, Univ. of Toronto Press (1960).

60. A. Bohr. Kgl. Danske Videnskab Selskab Mat. fys. Medd 26, No.14 (1952).

61. S.G. Nillson. Dan. Mat. Medd. 29, No.16 (1955).

62. C.A. Mallmann. Nuc. Phys. 24, 535 (1961).

63. D. Kurath. 'Nuclear Spectroscopy' edited by Fay Ajzenberg-Selove. Academic Press, page 983 (1960).